HUMAN SKIN OPTICAL PROPERTIES AND AUTOFLUORESCENCE DECAY DYNAMICS

by

Haishan Zeng

B.Sc., Peking University, 1983
M.Sc., Institute of Electronics, Academia Sinica, 1986

A THESIS SUBMITTED IN PARTIAL FULFILLMENT OF

THE REQUIREMENTS FOR THE DEGREE OF

DOCTOR OF PHILOSOPHY

in

THE FACULTY OF GRADUATE STUDIES
Department of Physics

We accept this thesis as conforming

to the required standard

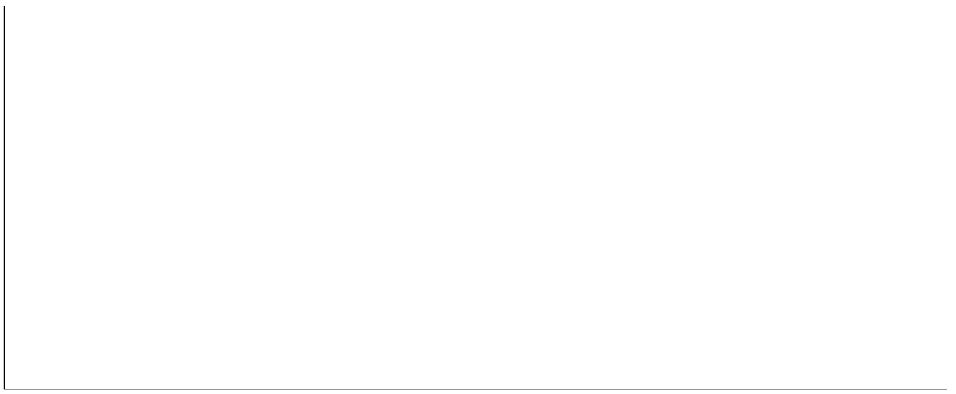

THE UNIVERSITY OF BRITISH COLUMBIA

August 1993

In presenting this thesis in partial fulfilment of the requirements for an advanced degree at the University of British Columbia, I agree that the Library shall make it freely available for reference and study. I further agree that permission for extensive copying of this thesis for scholarly purposes may be granted by the head of my department or by his or her representatives. It is understood that copying or publication of this thesis for financial gain shall not be allowed without my written permission.

(Signature)

Department of Physics

The University of British Columbia
Vancouver, Canada

Date Aug. 18, 1993

DE-6 (2/88)

ABSTRACT

Human skin is an optical organ which constantly interacts with light. Its optical properties are fundamental to understanding various effects of light-tissue interaction in human skin and to laser applications in medicine and biology. The aim of this thesis was to test two hypotheses: (1) that skin optical properties can be quantitatively modeled, and (2) that *in vivo* spectroscopic measurements can be used to derive information about skin structures. Both theoretical and experimental procedures were used to test these hypotheses.

Experimental studies were completed in terms of macroscopic, *in vivo* diffuse reflectance spectroscopy, autofluorescence spectroscopy, and temporal behavior of the autofluorescence signal during continuous laser exposure, as well as microscopic *in vitro* fluorophore distribution and spectral differences. Several interesting physical phenomena were discovered. Three new methods were developed for deriving information of different skin layers from *in vivo* and *in vitro* measurements. The most interesting finding was that, under continuous laser exposure, skin autofluorescence decays following a double exponential function and that the autofluorescence recovery takes about six days.

A seven layer skin optical model was developed based on (1) the structural anatomy of skin, (2) published optical properties of different skin layers and blood, and (3) measured skin fluorophore micro-distribution. Monte Carlo simulation

was used to solve the Boltzmann equation of radiative transfer for the new skin model. The solutions provided a detailed knowledge of light propagation in skin tissue.

The theoretical modeling unified the microscopic properties with the macroscopic *in vivo* skin measurements. The physical meaning of the autofluorescence double exponential decay dynamics was also elucidated. It was shown that the coefficients of the double decay can be used to estimate the fractional contributions of different skin layers to the observed *in vivo* autofluorescence signal. Using this approach, it was determined that the fractional contribution of the stratum corneum was ~ 14%, while the calculated value for the Monte Carlo skin model was ~ 15%, providing a close agreement between experimental and theoretical values. The dermis contributed the remaining 85% of the observed *in vivo* signal. We therefore, believe that the thesis hypotheses have been substantially proven. Although the skin has complicated inhomogeneous structures, its optical properties can now be quantitatively modeled and various modalities of *in vivo* skin spectroscopy can be used to derive information on skin structures.

TABLE OF CONTENTS

LIST OF TABLES

LIST OF FIGURES

LIST OF ABREVIATIONS AND SYMBOLS

a - Pre-exponential coefficient in the autofluorescence decay equation (23)

α - Illumination angle

b - Pre-exponential coefficient in the autofluorescence decay equation (23)

β - Pick-up (detection) angle
Also denotes "intrinsic fluorescence coefficient".

c - Constant term in the autofluorescence decay equation (23)

CCD - Charge coupled device

d - Thickness of a tissue slab

D - Tissue thickness

DNA - Deoxyribonucleic Acid

δ - Spatial resolution of fluorescence imaging

$E(\lambda_{em}, r, z)$ - Fluorescence escape function. It is the surface distribution as a function of radial position (r) of escaping photons from a point source of fluorescence at depth z and radial position r = 0 within a tissue.

$\varepsilon(\mathbf{r}, \mathbf{s})$ - Source function. It denotes the power radiation per unit volume per unit solid angle in the direction **s** at position **r**.

$\mathcal{J}(\ )$ - Denotes a monotonically increasing function.

F(s) - Probability density function for light attenuation (Eq.14)

$F(\lambda,r)$ - Observed flux of escaping fluorescence

FWHM - Full width at the half maximum

f - Fluorescence distortion factor or escape effectiveness

$\Phi(\mathbf{r})$ - Flux density vector, its quantity is the fluence or radiant flux rate per unit area. (Eq.10)

ψ - Azimuthal angle of photon deflection in a scattering event

g - Scattering anisotropy

$G(\psi)$ - Probability density function for direction of light scattering (Eq.15)

h - Planck's constant

Hb - Haemoglobin

HbO_2 - Oxyhaemoglobin

HKS - Hyperkeratotic skin

$H(\theta)$ - Probability density function for direction of light scattering (Eq.16)

λ - Wavelength of light (photon)

I - Intensity of light

IR - Infrared

K - Kubelka-Munk absorption coefficient

LIF - Laser induced fluorescence

LP - Long pass

$L(\mathbf{r},\mathbf{s})$ - Specific intensity or radiance denotes the average power flux density within a unit solid angle along direction **s**, at position **r**, and has the unit of $W/cm^2/sr$.

ω - Solid angle

MRI - Magnetic resonance imaging

MSP - Microspectrophotometer

μ_a - Absorption coefficients

μ_{eff} - Effective attenuation coefficient (Eq.3)

μ_s - Scattering coefficients

μ_s' - Reduced (or effective) scattering coefficient

μ_t - Total attenuation coefficient ($\mu_t = \mu_a + \mu_s$)

N' - Ratio of the reduced scattering to absorption

ν - Frequency of light

OMA - Optical Multichannel Analyzer

ρ - Distance along tissue surface

P - Power

PDA - Photo-diode array

PET - Positron Emission Tomograph

$p(\theta)$ - Scattering phase function

Q - Accumulated light power density in W/cm^3 that is deposited in a local tissue volume

γ - Angle between illumination plane and detection plane

θ - Photon deflection angle in a scattering event

$\mathbf{r}$ - Position vector

R - Diffuse reflectance or remittance

RGB - Red, green, blue

s - Direction vector

S - Kubelka-Munk scattering coefficient

S_0 - Ground state of the energy levels of a molecule

S_1 - First excited singlet state of a molecule

t - Time

T - Transmittance

T_c - Unscattered transmittance

T_1 - First excited triplet state of a molecule

τ - Time constant in an exponential decay

UV - Ultra violet

UVA - Ultra violet band A (320 nm - 400 nm)

UVR - Ultra violet radiation

VGA - Video Graphic Adaptor

Y - Quantum yield of fluorescence emission

ACKNOWLEDGMENTS

I would like to thank Dr. Branko Palcic whose guidance, supervision, and optimistic encouragement made all this work possible. Special thanks goes to Dr. Calum MacAulay for his daily supervision. Our discussions and his suggestions were always most helpful. Special thanks also goes to Dr. David McLean for his guidance, encouragement, and arrangement in obtaining the skin tissue samples. I am grateful to the staff of the Cancer Imaging Department of the B.C. Cancer Research Center for their support, especially, the administrative assistance of Vel Kinnie and the secretarial assistance of Susan Grose and Tanya Reimer.

I would also like to thank the members of my Ph.D. Supervisory Committee, Dr. Myer Bloom and Dr. John Eldridge, for their annually critical reviews on my thesis work. Finally, grateful acknowledgment is made to Dr. Steven Jacques at the University of Texas M.D. Anderson Cancer Center for his generosity in providing me the Monte Carlo code.

CHAPTER 1: INTRODUCTION

We human beings have two optical organs, the eye and the skin, both of which interact with light constantly. The eye is an ideal imaging device which consists of optically homogeneous tissue and which images objects onto the retina so that the brain can perceive the outside world. The imaging optics of eye can be described by geometrical optics, and have been widely discussed in optics textbooks. The skin, however, is an optically inhomogeneous and multi-layered turbid medium. Light interaction with skin tissue will be subject to scattering, absorption, and may also produce fluorescence and phosphorescence. These interactions cause turbidity and prevent us from seeing inside of the skin, and therefore, gives skin its aesthetic quality. The optics of skin has not been completely understood and is currently being intensively studied. This dissertation was dedicated to the physics of basic light-tissue interaction in human skin. The following is a brief review of the skin tissue optical property studies.

1.1 Overview of skin tissue optical properties

The physical properties of biological materials have been optimized with respect to the environmental constraints through evolutionary processes (Bloom, 1992, 1993). The optical properties of skin is just such an example. It is well known that exposure of skin to sunlight stimulates the synthesis of

vitamin D_3 which is essential for maintaining calcium and phosphorus homeostasis, and therefore a healthy skeleton (Holick *et al*, 1982). This is a known beneficial effect of light-tissue interaction in skin. However, over-exposure of skin to sunlight (especially its UV components) may cause sunburn, skin photoaging (dermatoheliosis), and even skin cancer. The optical properties of skin do provide some protective mechanisms against these damages. Perhaps, the most important is the strong absorption by melanin of short wavelength visible light and ultra violet radiation (UVR). Secondly, the scattering of incident light by inhomogeneous structures in skin tissue (e.g. cells in epidermis, collagen and elastin fiber bundles in dermis) also prevents it from penetrating deeply into the skin and subcutaneous tissue. It seems that both the absorption spectrum of melanin and the scattering coefficient variation with wavelength have been optimized for this protective purpose. For example, damage to DNA increases with decreasing wavelength, and the absorption coefficient of melanin increases sharply with the decreasing wavelength of the incident light (Anderson and Parrish, 1981). The scattering coefficients of various skin layers also show rapid increases with decreasing wavelength in the UV range, while they decrease slowly with increasing wavelength in the less damaging visible and infrared (IR) range (Anderson *et al*, 1979, Wan *et al*, 1981, Van Gemert *et al*, 1989). This evolutionary optimization enables skin to effectively block harmful UVR and short wavelength visible light from penetrating

deeply to damage the underlying viable tissue, but allows relatively harmless long wavelength visible and near infrared light to penetrate deep into the tissue, facilitating diagnosis and therapy of various skin diseases by light.

In addition to the above mentioned stimulating vitamin D_3 synthesis and DNA damage, the light-tissue interactions in human skin cause many photophysical (photothermal, photomechanical etc., see for example, Anderson and Parrish, 1983, Bulnois, 1986, Jacques, 1992), photochemical, and photobiological effects (see for example, Urbach, 1969, Magnus, 1976, Parrish *et al*, 1978, Diffey, 1980, 1984, Regan and Parrish, 1982, Martellucci and Chester, 1985, Kochevar, 1986). Light-tissue interaction can also be used for diagnostic and therapeutic purposes in dermatology (see, for example, Anderson and Parrish, 1981, Goldman, 1981, Regan and Parrish, 1982, Arndt *et al*, 1983, Goldman 1991, Goldman and Kerr 1991, Chester *et al*, 1991, Green *et al*, 1992). In diagnosis, the effect of tissue on light is exploited to detect malignant changes, while therapeutic applications (surgical and non-surgical) are based on the effect of light on tissue (Parrish and Wilson, 1991).

To understand all the light induced phenomena and their use in clinical applications, knowledge of the initial events (scattering, absorption, and fluorescence) of light-tissue interaction and the immediate measurable effects (diffuse reflectance and fluorescence spectra) is the necessary prerequisite. The scattering and absorption determine the light micro-distribution inside the skin tissue which is

important for generation of any biological effects and for therapeutic applications as well as for determining the information contained in any diagnostic signal. The diffuse reflectance and fluorescence spectra are non-invasively measurable from *in vivo* skin, therefore, are diagnostically significant. The work in this thesis concentrated on the basic optical properties (scattering, absorption, autofluorescence, and reflectance) of normal human skin and their relationships with the microscopic structure of skin, in agreement with the postulate that understanding the normal is the key to understanding the abnormal (Montagna *et al*, 1992).

1.1.1 The structure of skin

For the convenience of the later discussion, a brief description of the structure of skin is provided here. There are a number of treatises describing the anatomy and functions of the skin (for example, see Montagna and Lobitz, 1964, Fitzpatrick *et al*, 1971, Montagna and Parakkal, 1974, Parrish, 1975, Montagna *et al*, 1992). The skin accounts for about 15% of total body mass and can be considered the largest organ of the body. It consists of an outer epidermis, the dermis, and the subcutaneous tissue (Figure 1). It contains nerves, blood vessels, glands, and hair follicles. The skin is the barrier to a hostile external world. The functions of skin include protection from the external environment, inhibition of water

loss, absorption and blockage of radiation, temperature regulation, sensory perception, and immunological surveillance.

The epidermis contains no blood or lymphatic vessels and is composed of a continually renewing, stratified, squamous epithelium. The superficial layer of the epidermis (the stratum corneum or horny layer) consists of dehydrated flattened dead cells. It is a mechanically tough and chemically resistant layer. The epidermal cells are manufactured by the keratinocytes (prickle cells) of the stratum malpighii. Keratinocytes are derived from a single germinative layer of basal cells. In normal skin, it may take up to 14 days for a daughter cell of the basal layer to reach the stratum corneum, and another one or two weeks before it is sloughed off from the skin surface. Specialized cells called melanocytes reside within the basal layer and produce melanin-containing granules called melanosomes, which are transferred through dendritic processes to the keratinocytes of the epidermis. As the keratinocytes migrate outward, some melanin is carried toward the surface of the skin, eventually appearing in the stratum corneum. Melanin is a complex macromolecular protein which strongly absorbs UV radiation and short wavelength visible light, and plays an important role in attenuating the light before reaching the viable cells in the skin. As a response to UVR-induced injury and a mechanism to protect against sunburn, the skin can produce more melanin. this new melanin, in turn, protects the skin from new damage of the sunlight. This UVR-induced melanin may also prevent the

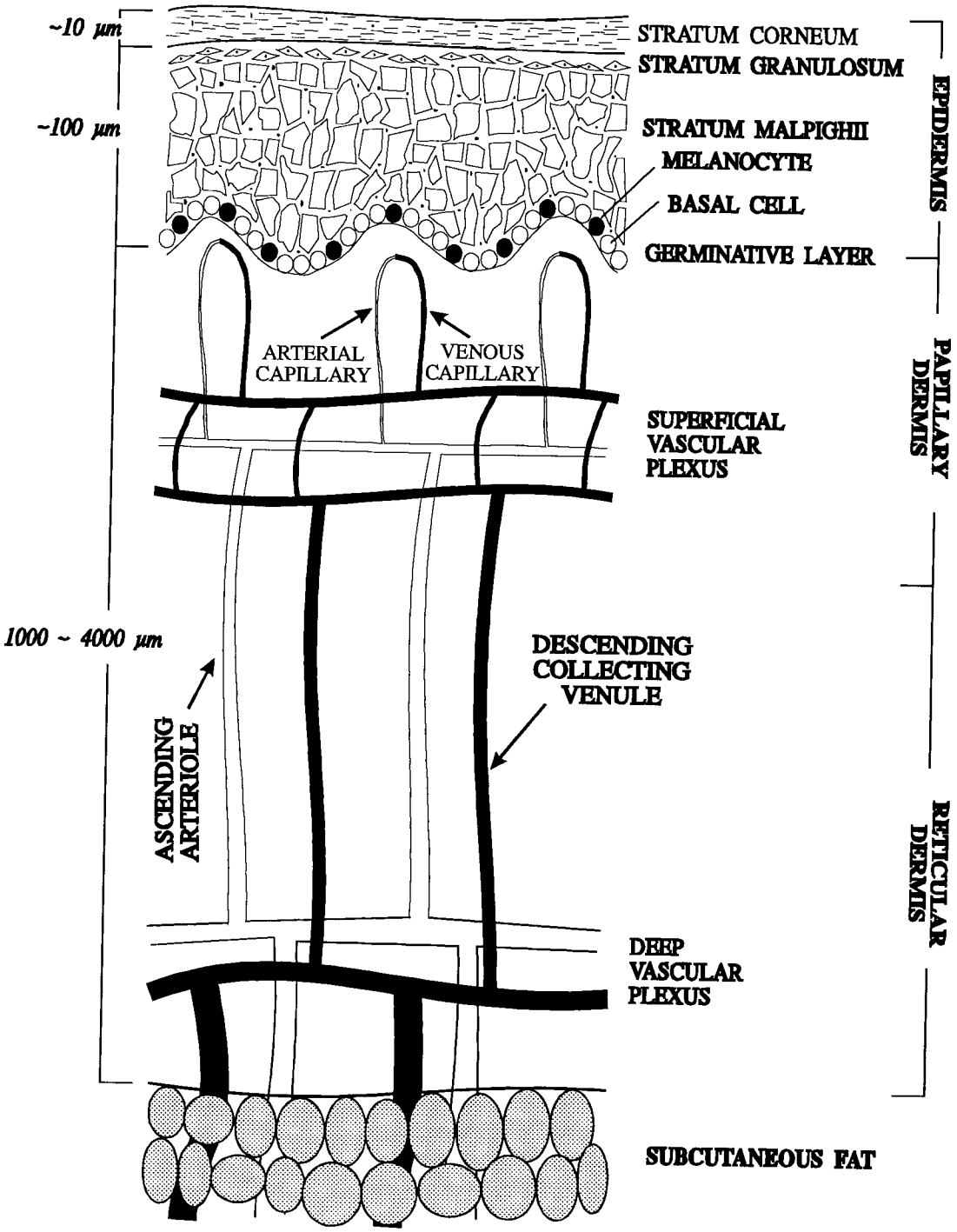

Figure 1. Schematic diagram of the structure of skin.

over-production of vitamin D_3 by absorbing more UV radiation. Too much vitamin D might result in calcification of soft body tissue, possiblely causing kidney stones and other pathological calcifications.

Below the epidermis lies the dermis, which has well-marked ridges and projections on its upper surface. These ridges, with anchoring fibers, prevent the two layers from separating due to shearing forces. Primarily, the dermis consists of collagen and elastic fibers embedded in a viscous gel of water and mucopolysaccharides (ground materials). In the dermis, there are relatively few cells compared to the epidermis. Scattered cells called fibroblasts produce the fibers, proteins and viscous ground materials of the dermis. The uppermost dermal layer, called papillary dermis, contains many capillaries, lymphatics, and nerves, giving it more cellular appearance than the underlying reticular dermis. The reticular dermis is more fibrous, contains larger vessels, and has fewer cells and less ground substance than the papillary dermis. The dermis normally contains no melanin. The blood vessel distribution in the dermis consists of two plexuses: one plexus is located in the papillary dermis and branches into many capillaries toward the epidermis, the other is near the bottom of the dermis. The skin blood supply is far more than enough for cell nutrition, and it acts as a heat regulator. Collagen and elastin fibers have diameters comparable or larger than the wavelength of visible and UV light and are largely responsible for the strong scattering properties of the dermis. Collagen

makes up 75% of the dry weight of the skin and provides both tensile strength and elasticity. Three collagen chains make up a collagen molecule, collagen molecules are cross linked in the extracellular space into collagen fibrils. The fibrils collect into small groups or fibers that can be seen with the light microscope. Fibers, in turn, organize into larger fiber bundles. Elastic fibers account for about 4% of the dermal proteins and form a network that borders the collagen bundles and strengthens the elasticity of skin. The collagen in the papillary dermis is mainly type III, which consists of small-diameter fibrils organized into small fiber bundles. The reticular dermis is composed primarily of type I collagen, which consists of large-diameter fibrils woven into large fiber bundles. The subcutaneous tissue supports the dermis. It consists mainly of fatty tissue, which acts as an insulator and a shock absorber as well as serving as a readily available source of energy.

The presence of these various skin layers leads to the skin behaving optically as a highly scattering, turbid medium. Figure 2 is a schematic representation of the possible light pathways in skin tissue. When a beam of light reaches the skin surface, part of it will be reflected by the surface directly, while the rest will be refracted and transmitted into the skin (Tregear 1966, Anderson and Parrish 1981). The direct reflection by the skin surface is called regular reflection, and is related only to the refractive index change between air and the stratum corneum of the skin. The light transmitted

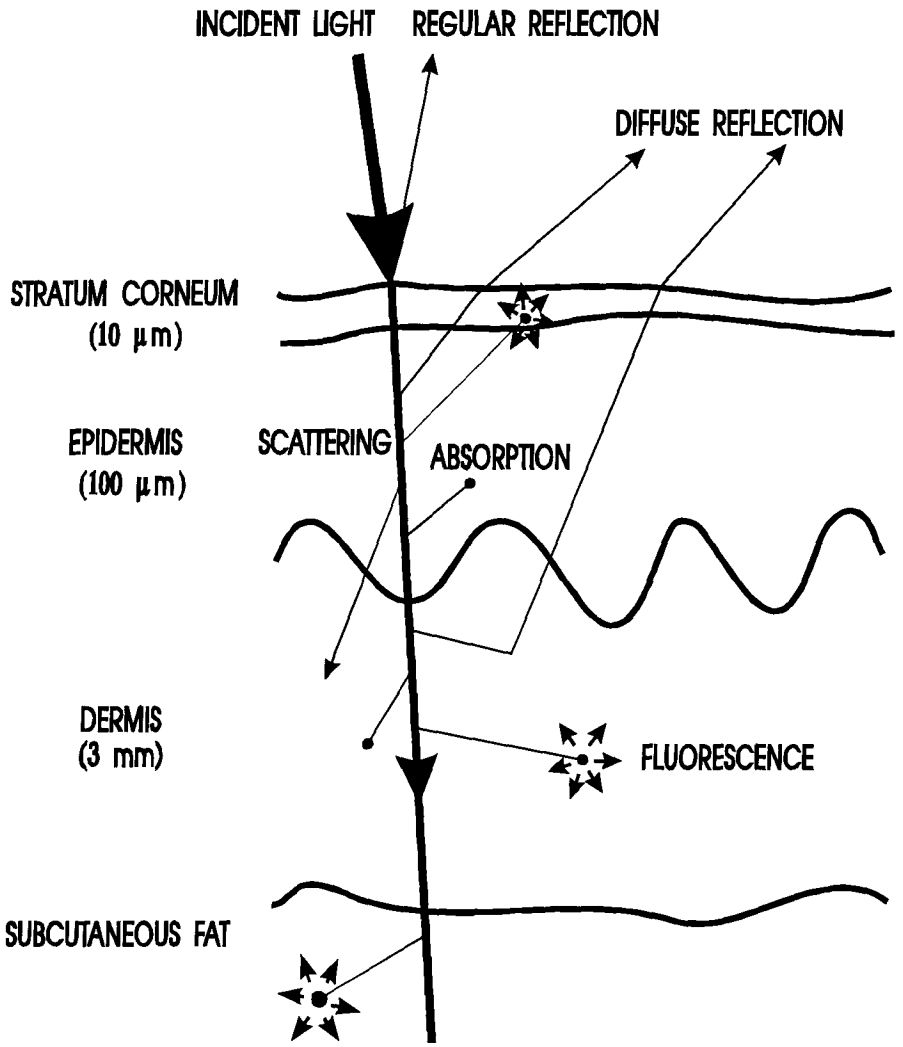

Figure 2. Schematic diagram of light pathway in skin tissue.

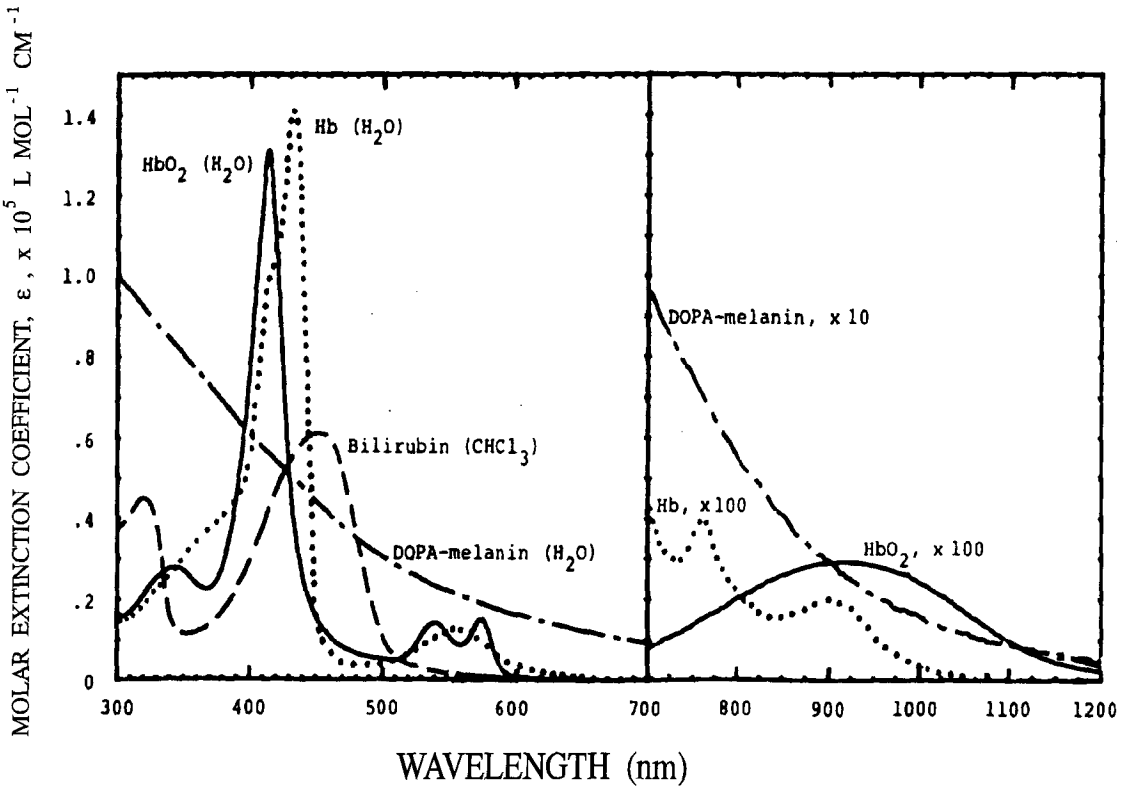

Figure 3 Absorption spectra of major skin chromophores, oxyhaemoglobin, HbO_2, (—), haemoglobin, Hb (·····), bilirubin (- - -), and DOPA-melanin (–·–). Parentheses indicate solvent. The spectrum shown for DOPA-melanin is the absorbance on a scale of 0 to 1.5 of 1.5 mg% aqueous solution. Not shown is β-carotene, which has a broad absorption band qualitatively similar to that for bilirubin in the 400-500 nm region, with maxima at 466 and 497 nm in $CHCl_3$. Note scale changes in the near infrared. (Adapted from Anderson and Parrish, 1981.)

into the skin will be scattered and absorbed by the skin tissue. After multiple scattering, some of the transmitted light will re-emerge through the air-stratum interface into the air. This re-emergence is called diffuse reflection (or remittance). The amount of diffuse reflection is determined by both scattering and absorption properties of the skin tissue. The stronger the absorption, the less the diffuse reflection; the stronger the scattering, the larger the diffuse reflection. Following absorption of a photon by the skin, the electrically excited absorbing molecule may rapidly return to a more stable energy state (1) by re-emission of a photon with lower energy in the form of fluorescence or phosphorescence; (2) by relaxation through vibrational or rotational energy levels, resulting in production of heat; (3) by undergoing a permanent structural changes; and/or (4) by reaction with an appropriate nearby molecule. Different chromophores reside in different skin layers and have different absorption spectra. Figure 3 shows the absorption spectra of major skin chromophores (Anderson and Parrish, 1981).

1.1.2 Diffuse reflectance of skin

Studies of skin reflectance started many decades ago (Edwards and Duntley, 1939, Goldzieher *et al*, 1951, Edwards *et al*, 1951, Kuppenheim and Heer, 1952, Jacquez *et al*, 1955, Jacquez *et al*, 1955b, Hardy *et al*, 1956, Ballowitz and Avery, 1970, for review of early work, see Tregear, 1966). Most of

these early studies employed an integrating sphere to collect all reflected light including the regular reflection. Acquisition of a complete spectrum could take as long as one-half hour (see for example, Jacquez *et al*, 1955). As the subjects being studied must remain motionless, they were probably somewhat uncomfortable. Depending on the spectrophotometer used, many of these early works obtained more or less accurate reflectance spectra, in general, consistent with the results obtained by modern instruments. In many modern setups for skin reflectance measurements (Dawson *et al*, 1980, Tang and Wan, 1983, Kollias and Baqer, 1984), optical fibers are used to collect only part of the reflected light, excluding the regular reflection. Regular reflection contains no information about the inside skin composition and structure, and can interfere with the diffuse reflection signal. The addition of computer controlled filter wheels and stepper motor for wavelength change in a single channel spectrophotometer reduced the time required to obtain a spectrum to a few minutes. For this thesis, a computerized spectroanalyser system was built using fiber optic sampling and optical multichannel analyzer (OMA) (Zeng *et al*, 1992, 1993). Our system can acquire a reflectance spectrum very rapidly (in less than 1 second) with a repeatability of 0.7%.

Although over the years, skin reflectance and transmittance have been measured from time to time, theoretical modeling of the optical properties of skin has been carried out only in the last decade. It started with the application of

the Kubelka-Munk model (Kubelka and Munk 1931, Kubelka 1948, Kubelka, 1954, Atkins, 1969) to analytical modeling of the relationship between the optical properties of single skin layers and the *in vivo* reflectance by Anderson *et al* (1979, 1981, 1982) and Wan *et al* (1981). The Kubelka-Munk theory is an approximate solution to the Boltzmann equation of radiation transport (Chandrasekhar, 1960). It is only applicable to isotropic, strong scattering media and requires diffuse incident illumination which is hard to satisfy experimentally. In recent years, various improvements to the Kubelka-Munk model and other approximate solutions to the transport equation have been developed (Takatani and Graham, 1979, Bonner *et al*, 1987, Van Gemert and Star, 1987, Van Gemert *et al*, 1987, 1988, Yoon *et al*, 1987, 1989, Arnfield *et al*, 1988, Keijzer *et al*, 1988, Star *et al*, 1988, Steinke and Shepherd, 1988). Of these, the diffusion theory (which very well approximates the transport equation when scattering dominates over absorption and deals with situations far away from light source and boundaries) is very successful in elucidating the basic characteristics of light transport in turbid biological tissue in analytical formulae or by less intensive numerical computing (Ishimaru, 1978, van de Hulst, 1980, Groenhuis *et al*, 1983, Marijnissen and Star, 1984, Marijnissen *et al*, 1985, Wilson and Patterson, 1986, Star *et al*, 1987, Van Gemert *et al*, 1987, 1988, Keijzer *et al*, 1988, Wilson *et al*, 1988, Jacques, 1989, Karagiannes *et al*, 1989, Patterson *et al*, 1989, 1991, 1991b, Yoon *et al*, 1989, Farrel *et al*, 1992). Diffusion theory also permits a more

accurate determination of the basic transport parameters of tissue from reflection and transmission measurements of tissue slab (Jacques and Prahl, 1987, Cheong, *et al*, 1990). More recently, Monte Carlo methods have been developed to obtain rigorous numerical solutions of the transport equation (Wilson and Adam, 1983, Flock *et al*, 1988, 1989, Prahl *et al*, 1989, Wyman *et al*, 1989, Keijzer *et al*, 1989, Hebden and Kruger, 1990, Jacques and Keijzer, 1991, Haselgrove *et al*, 1991, Gardner and Welch, 1992, Wang and Jacques, 1992). We now know that the diffuse reflectance of a uniform[1] semi-infinite tissue bulk is a monotonically increasing function of the ratio, N', of the reduced scattering to absorption.

$$N' = \mu_s' / \mu_a = \mu_s(1 - g) / \mu_a \qquad (1)$$

where μ_s and μ_a are the tissue scattering and absorption coefficients respectively, and g the scattering anisotropy. For a derivation of this function, see Patterson *et al* 1989 (diffusion theory) and Jacques 1989 (Monte Carlo simulation). For experimental demonstration, see Wilson and Jacques 1990. Very recently, using photon migration formulism and Monte Carlo simulation, Wu *et al* (1993) worked out an analytical formula for this function valid for the tissue optical parameters

---

[1] Most biological tissues have granular (e.g. cells) or fibrous (e.g. collagen fibers) structures and are, therefore, optically inhomogeneous. "Uniform" in this thesis means that the optical inhomogeneity of the tissue is uniform, i.e. the tranport parameters, μ_a, μ_s, g, are constants over the specified uniform tissue volume.

range of μ_s/μ_a (= 5 - 300), g (= 0.7 - 0.95) and refraction index matched boundary conditions.

Inspired by the theoretical modeling of light transport in turbid biological tissue, more complicated reflectance measurement modalities have been developed. Wilson and Jacques (1990) summarized these modalities into four categories: 1) steady-state measurement of the total remittance R, 2) time-resolved measurement of total diffuse reflectance R(t) as a function of time t, 3) steady-state measurement of the local spatial distribution of remittance $R(\rho)$ along the tissue surface, and 4) time-resolved measurement of the local spatial distribution of remittance $R(\rho,t)$ along the tissue surface as a function of time. In this thesis, a fifth modality was added which is a steady-state measurement of the remittance angular distribution $R(\beta)$ as a function of detection angle β. Our preliminary results suggest that $R(\beta)$ may be used to derive information from different skin layers (Zeng *et al*, 1992, 1993).

For uniform semi-infinite tissue, steady state measurement of the total remittance R can determine the ratio N', while steady-state $R(\rho)$ measurement can determine μ_{eff} given:

$$R(\rho) \propto \frac{1}{\rho^2} e^{-\mu_{eff}\rho} \qquad (2)$$

for $\rho >> \mu_s'$(Groenhuis *et al*, 1983, Butler *et al*, 1985, Bonner *et al*, 1987, Nossal *et al*, 1988, Patterson *et al*, 1989, Patterson *et al*, 1989b), where μ_{eff} is the effective attenuation

coefficient in diffusion theory. Combining these two steady-state techniques, μ_a and μ_s' can be obtained non-invasively:

$$\mu_a = \frac{\mu_{eff}}{\sqrt{3(1 + N')}} \quad (3a)$$

$$\mu_s' = \mu_a N' \quad (3b)$$

Using time-resolved techniques, μ_a, μ_s, and g (of a semi-infinite uniform media) can all be determined non-invasively. For details, see Chance 1988, Chance *et al* 1988, Wilson *et al* 1989, Lokowicz *et al* 1989, Jacques 1989b, Nossal *et al* 1989, Wilson 1989.

The above elegant formulae (1), (2), (3) and the theory for time resolved techniques are, however, based on uniform semi-infinite media. Although this greatly improves our understanding of tissue optics, it does not work for multi-layered heterogeneous media like skin. Before it becomes applicable to skin studies, the inverse problem (i.e. algorithm for deriving μ_a, μ_s, and g from R measurements) for multi-layered media must be solved first. These inverse solutions are not yet available. However, it has been found in many clinical applications that the relative changes of the absorption properties of a specific chromophore are very useful. In these situations, the steady-state total reflectance spectroscopy has found many applications.

The measured diffuse reflectance of skin changes significantly in the 300 to 1100 nm wavelength range depending on the melanin content in the various skin types. A five fold difference in reflectance was reported by Kuppenheim and Heer

(1952) between white and Negro skin. However, for wavelength larger than 1100 nm, due to the lack of significant absorption by melanin, the reflectance of dark Negroid and fair Caucasian skin are about the same (Jacquez *et al*, 1955b, Anderson and Parrish, 1981, 1982). In general, the reflectance of Caucasian skin (see, for example, figure 6-11 in Anderson and Parrish, 1982) is characterized by a low reflectance of less than 10% at wavelengths shorter than 300 nm. The reflectance rapidly rises with a maximum of 20-40% around 350-360 nm. From 400-700 nm, the reflectance continually increases to a maximum of 50-70%. There are small minima located at about 430 nm, 530-540 nm, and 570-580 nm which can be attributed to haemoglobin absorption in blood. The general increasing trends of the spectrum correspond to the melanin absorption characteristics of decreasing with wavelength. As the wavelength is further increased, reflection declines with marked dips due to water absorption. These spectral characteristics are the result of a complex interplay of the intrinsic absorption and scattering properties of various skin layers. Generally, the absorption effects of various skin chromophores are obvious. Therefore, over the years, many applications have been found with the reflectance spectroscopy in quantifying the relative amount of various chromophores (melanin, haemoglobin, and bilirubin) in skin at normal or diseased states or for photobiological effect studies (Daniels and Imbrie, 1957, Frank *et al*, 1961, Findlay, 1966, Hannemann *et al*, 1978, Dawson *et al*, 1980, Yamanouchi *et al*, 1980, Feather *et al*, 1982, 1988, 1989, Wan *et al*, 1983,

Kollias and Baqer, 1984, 1985, 1986, 1987, 1988, Leveque *et al*, 1985, Kollias *et al, 1989,* Swairjo *et al*, 1989, Rosen *et al*, 1990). Other applications of reflectance include quantitative assessment of skin color (Edwards and Duntley, 1939, Findlay, 1970, Feather *et al*, 1982, Tang and Wan, 1983, Towne and Hulse, 1990, Weatherall and Coombs, 1992), detection of skin cancer (Marchesini *et al*, 1991, 1992), and the oximeter for determining cutaneous blood oxygen saturation (see, for example, Brinkman *et al*, 1949, 1949b, Bowes *et al*, 1989, Mendelson *et al*, 1991, 1991b) etc.. Photography and computerized imaging techniques which exploit the spatial distribution of reflectance under broad beam illumination (and therefore measure the chromophore distribution in a skin lesion) are also under development by many authors to improve the diagnosis of skin cancer and other skin diseases (Marshall, 1976, 1980, 1981, 1982, Picton *et al*, 1976, Cascineli *et al*, 1987, Murray, 1988, Moss *et al*, 1989, Perednia *et al*, 1989, Herbin *et al*, 1990, Green *et al*, 1991, Perednia, 1991, Claridge *et al*, 1992, Dhawan and Sicsu, 1992, Golston *et al*, 1992, Perednia and White, 1992, Stoecker *et al*, 1992, 1992b, Stoecker and Moss, 1992, Umbaugh *et al*, 1992, White and Perednia, 1992, Kenet *et al*, 1993). The successful development and enhancement of these imaging methods for skin diagnosis will greatly depend on our knowledge on the optical properties of skin.

1.1.3 Transport parameters, μ_a, μ_s, g, of single skin layers

Currently, no method will allow us to completely determine optical properties of single skin layers solely from *in vivo* measurements. A natural step in skin study is therefore to investigate optical properties of single skin layers *in vitro*. The measurements of transmission and reflection properties of excised skin layers have a history extending over many decades (for review, see Tregear, 1966, Magnus, 1976, Parrish *et al*, 1978, Duck, 1990). In general, the methods for skin sample preparation affect the measurement results. However, the absorption of DNA and protein in the UV range and of water in the IR range is usually obvious on the spectrum curves. Through these studies, it was eventually elucidated that light scattering by skin tissue is non-isotropic (Hardy *et al*, 1956), strongly forward (Everett *et al*, 1966, Bruls and van der Leun, 1984), and that the scattering angular distribution can be approximated by the Henyey-Greenstein phase function (Jacques *et al*, 1987b). Reliable and consistent transmission and reflection measurements for thin epidermis and dermis samples were reported by Anderson *et al*, 1979 and Wan *et al*, 1981 using the same spectrophotometer setup.

Due to the strong scattering, Beer's law does not hold when light transmits through skin tissue. The absorption and scattering parameters cannot be obtained unless a radiation transport model is employed. It was not until 1973 that Sayre for the first time obtained the "scattering power SX" and the

"absorptive power KX" of epidermis by applying the Kubelka-Munk theory (Sayre, 1973). Anderson *et al* 1979 and Wan *et al* 1981 calculated systematically the diffuse scattering (S) and absorption (K) coefficients of epidermis and dermis from transmission and reflection measurements and used them to analyze the *in vivo* skin remittance by the Kubelka-Munk theory. The relationship between the Kubelka-Munk absorption and scattering coefficients K, S and the general transport parameters μ_a, μ_s, g was only worked out very recently (van Gemert and Star, 1987).

The absorption coefficient μ_a is in units of cm^{-1}, and its inverse value $1/\mu_a$ indicates the mean free path between absorption events. The scattering coefficient μ_s is also in unit cm^{-1}, and its inverse value $1/\mu_s$ indicates the mean free path between scattering events. The anisotropy g indicates the angular deflection of a photon's trajectory caused by a scattering event. The anisotropy equals the expectation value, $\langle\cos\theta\rangle$, where θ is the photon deflection angle. The effectiveness of light scattering is described by the product $\mu_s(1-g)$. A g of zero, corresponding to isotropic scattering that scatters light randomly in all directions, implies that the scattering is 100% effective. If g equals 0.9, then a photon must be scattered 10 times to achieve the randomization equivalent to a single isotropic scattering event. If g equals 1, it corresponds to total forward scattering. The effective (or reduced) scattering coefficient, $\mu_s(1-g)$, or simply μ_s', is in units of cm^{-1} too, and its inverse value $1/\mu_s'$ indicates the

mean free path before a photon's trajectory becomes randomized. The relationship between the Kubelka-Munk K, S parameters and the transport parameters, μ_a, μ_s, g, are:

$$\mu_a = \eta K \tag{4a}$$

$$\mu_s(1-g) = \chi S \tag{4b}$$

where η and χ are functions of $\mu_a/[\mu_a + \mu_s(1-g)]$ and of K/S and can be found in van Gemert and Star, 1987, van Gemert *et al*, 1989. If scattering dominates over absorption $[\mu_s(1-g) >> \mu_a]$, Eqs. (4a) and (4b) become:

$$K = 2\mu_a \tag{5a}$$

$$S = \tfrac{3}{4}\mu_s(1-g) - \tfrac{1}{4}\mu_a \tag{5b}$$

In a review paper, "Skin Optics", van Gemert *et al* (1989) fitted the goniometer measurement data from stratum corneum, epidermis, and dermis of Everett *et al* 1966, Bruls and van der Leun 1984 with the Henyey-Greenstein phase function (Henyey and Greenstein, 1941) to obtain anisotropy g values. The g for stratum corneum is approximately 0.9 with a tendency to increase slightly with increasing wavelength. The g values for both epidermis and dermis can be approximated by

$$g \approx 0.62 + \lambda 0.29 \times 10^{-3} \quad (\lambda \text{ in nm}) \tag{6}$$

where λ is the wavelength of light. The g value at 633 nm evaluated by this formula is 0.80 which is very close to the value obtained by Jacques *et al*, 1987b. They used formulae (4a), (4b) and the above g values to convert the K, S data of Anderson *et al* 1979 and Wan *et al* 1981 into transport parameters, μ_a, μ_s. The results are shown in figure 4. For all skin layers, the scattering coefficient μ_s are larger than the

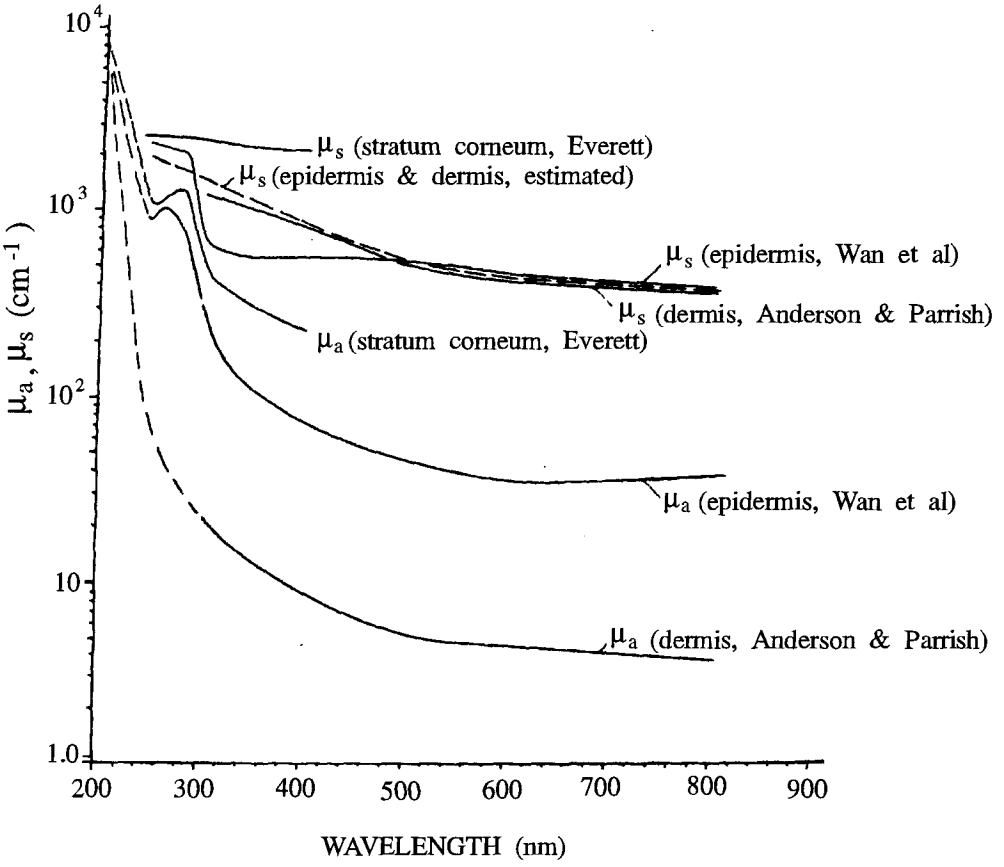

Figure 4. Transport parameters μ_a, μ_s of various skin layers as a function of wavelength: stratum corneum (from data by Everett *et al*, 1966); epidermis (from data by Wan *et al*, 1981); and dermis (from data by Anderson and Parrish, 1979). For shorter UV wavelengths (< 200 nm) absorption coefficients indicated by (– – – –) are likely to reach values of μ_a ~ 10000 cm^{-1}. The dashed line (– – – –) shows the estimated epidermal and dermal scattering coefficient, assumed equal to each other. (Adapted from van Gemert *et al*, 1989.)

absorption coefficient μ_a. The fact that the μ_s decreases slowly with increasing wavelength and large g values indicates that the skin tissue scattering is Mie's type and strongly forward. It must be noted that the absorption coefficient μ_a *in vitro* does not include the contribution of blood found in *in vivo* skin.

In recent years, a host of investigators have developed various techniques and methods to measure the 3 transport parameters (μ_a, μ_s, g) of various tissue *in vitro* (Cheong *et al*, 1990). In summary, any three of the following five measurements will be sufficient to determine the three parameters: (1) total (or diffuse) transmission for collimated or diffuse irradiance, (2) total (or diffuse) reflection for collimated or diffuse irradiance, (3) absorbance of the sample, placed inside an integrating sphere, (4) unscattered (collimated) transmission for collimated irradiation, and (5) angular distribution of emitted light from an irradiated sample. The data processing methods for determining the three parameters can be classified into the following categories:

a) *Direct Methods* which do not depend on any specific transport model to obtain the optical parameter from measurements. For example, μ_t (= μ_a + μ_s) can be derived directly from the above measurement (4) using Beer's Law:

$$T_c = exp(-\mu_t t) \qquad (7)$$

where T_c is the unscattered transmittance, and t the thickness of the tissue slab.

b) *Noniterative Indirect Methods* which require simple expressions relating the optical properties to measured transmission T and reflection (R). For example, one of the simple expressions is the Kubelka-Munk formulae (Anderson and Parrish, 1982):

$$\frac{K}{S} = \frac{1 + R^2 - T^2}{2R} - 1 \qquad (8a)$$

$$S = \frac{1}{d}\left(\frac{K}{S(K/S+2)}\right)^{-1/2} \coth^{-1}\frac{1 - R(K/S+1)}{R[K/S(K/S+2)]^{1/2}} \qquad (8b)$$

where d is the thickness of the tissue slab. Then Eq. (4) or (5) can be used to turn K, S into μ_a and $\mu_s(1\text{-}g)$. However, this method is usually only an approximation because the assumed diffuse irradiance situation is hard to realize experimentally (van Gemert *et al*, 1989, Cheong *et al*, 1990).

c) *Iterative Indirect Methods* which use complicated solutions to the transport equation. Examples are diffusion theory (Jacques and Prahl, 1987), adding-doubling model (Prahl *et al*, 1993), and Monte Carlo (Wilksch *et al*, 1984, Peters *et al*, 1990). Iterative algorithms may be computing intensive, but generate more accurate parameters.

Transport parameter determination of skin tissue by iterative algorithms have been reported by Jacques and Prahl 1987, Jacques 1991b, Marchesini *et al*, 1992b, Graaff *et al*, 1993. Some of the new data showed agreement with the data compiled by van Gemert *et al*, 1989, but some did not. The data in van Gemert *et al*, 1989 are still the most complete and self consistent transport parameters of skin tissue available today.

These data were, therefore, used for Monte Carlo simulation in this thesis. In the future, however, it would be definitely worth-while to explore a more detailed and complete determination of the transport parameters of various skin layers at different wavelengths using iterative algorithms.

As mentioned in Section 1.1.2, more recently, spatially resolved and time-resolved reflectance measurements are being exploited to determine the tissue transport parameters non-invasively. Other non-invasive methods include pulsed photothermal radiometry (PPTR) (Long *et al*, 1987, Anderson *et al*, 1989, Prahl *et al*, 1992) and photoacoustic effects (MacLeod *et al*, 1988). However, the photoacoustic method can measure only the absorption coefficient. To apply the PPTR and the reflectance methods for *in vivo* skin transport parameters determination, more theoretical studies on solving the inverse problem of multi-layered media are required.

1.1.4 Autofluorescence of skin

Autofluorescence of skin is the fluorescence emission of natural fluorophores inside the skin tissue upon excitation by absorption of certain wavelength of light. When laser light is used for excitation, it is called laser induced fluorescence (LIF) by some authors. Figure 5 shows the photon absorption, fluorescence emission, and other accompanying physical processes schematically. More general treatises on fluorescence can be found in Becker, 1966, Guilbault, 1973, and

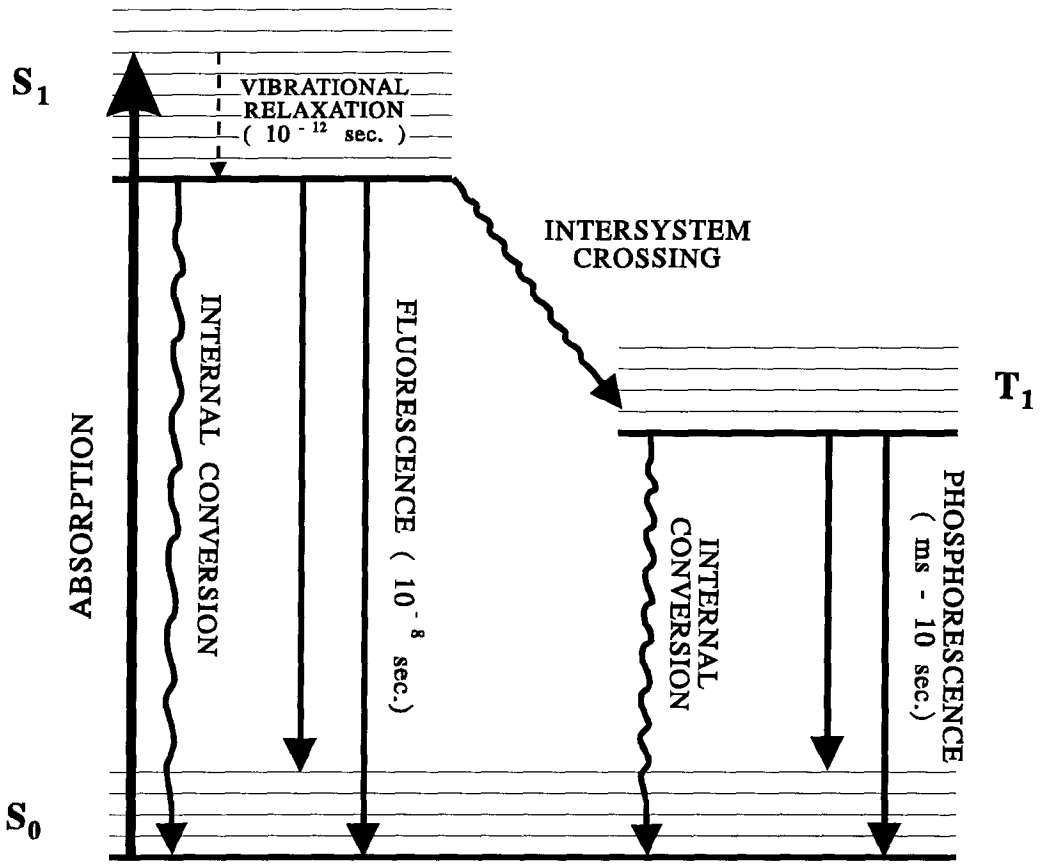

Figure 5. Schematic diagram of some physical processes relevant to fluorescence emission. Following absorption of a photon, the molecule will be excited from the ground state S_0 to some vibrational energy level of the first excited singlet S_1. Then it very rapidly relaxed to the zero vibrational state of S_1 (in 10^{-12} sec.). The molecule will return to the ground state from there by either internal conversion (generating heat) or emission of a photon (fluorescence). It may also transit to the first triplet state T_1 through intersystem crossing. The molecule at T_1 will return to S_0 through either internal conversion or photon emission (phorsphorescence). Because the transition from T_1 to S_0 is forbidden, the life time of phosphorescence could be as long as 1 ms to 10 sec. Not shown in this diagram are other processes including a permanent structure change of the molecule and chemical reaction of the excited molecule with an appropriate nearby molecule.

Lakowicz, 1983. Skin autofluorescence was observed as early as in 1908 according to Anderson and Parrish (1982). The device used is now called "Wood's lamp" which consists of a mercury discharge lamp and a UVA-transmitting, visible-absorbing filter. When using this device to observe skin autofluorescence, apparently, the eyes serve as both the detector and the long pass filter. The eye is not sensitive to the UV light, but is very sensitive to the visible light. Dermatologists have since used the organism's particular fluorescence to diagnose infections such as tinea capitis, erythrasma, and some *Pseudomonas* infections. The Wood's lamp can also be used to detect porphyrins in hair, skin, or urine (Caplan, 1967). Another application of Wood's lamp is that of visualizing subtle changes in epidermal melanin pigmentation and assessing whether pigmented lesions are due to epidermal versus dermal deposition of pigments (Gilchrest *et al*, 1977).

Hoerman (1971) reviewed most of the early spectroscopic studies of skin autofluorescence. Those studies concentrated on the UV light excited fluorescence. It was proven that the ring-membered amino acid residues, tryptophan and tyrosine in skin protein contents, fluoresce at 353 nm and 303 nm (maximum wavelengths), respectively with a maximum excitation band near 280 nm. The skin autofluorescence at these wavelengths is quite strong and may cause significant error to the dermal transmission measurements (Anderson and Parrish 1982). Another important discovery was the visible skin autofluorescence peaked at about 405 nm which, by its apparent high efficiency

and excitation maximum ($\lambda \approx 340$ nm), does not support its origin from the primary protein structure. It was suggested that this fluorescence may be due to the cross-links of collagen and/or elastin (Labella, 1971). But the successful isolation of the fluorophore(s) has not yet been achieved and therefore, at the present time, the fluorophores responsible for the visible autofluorescence of skin are still unknown. Other fluorescence species in skin were also found but were thought to be insignificant comparing to the strong *in vivo* autofluorescence signal. For example, NADH (nicotinamide adenine dinucleotide) has a peak emission at $\lambda \approx 460$ nm after excitation at $\lambda \approx 340$ nm. Using a microspectrograph with fluorescence measuring capabilities, Caspersson *et al* (1965) found that some dermal autofluorescence (DAF) cells fluoresce with a peak at $\lambda \approx 500$ nm. However, macroscopically, this emission is inconsequential compared to the total fluorescence of skin arising from such fluorophores as ring-membered amino acids in collagen and glycoproteins.

Although the natural fluorophores responsible for most of the visible autofluorescence of skin have not yet been identified, skin autofluorescence has been applied in skin disease diagnosis. More recent applications of skin autofluorescence include skin cancer detection (Lohmann *et al*, 1988, 1991) and photoaging study (Leffell *et al*, 1988). Prior to this thesis work, all reported skin autofluorescence studies used UV excitation. However, recently, tissue autofluorescence of other organs excited by both UV and visible light have been

demonstrated and used to improve the diagnoses of various diseases including atherosclerotic plaque and cancer of various tissues (Alfano *et al*, 1984, 1987, 1988, Kittrell *et al*, 1985, Satori *et al*, 1986, 1988, Deckelbaum *et al*, 1987, Montan and Strombland, 1987, Yang *et al*, 1987, Clarke *et al*, 1988, Oraevsky *et al*, 1988, Tang *et al*, 1989, Richards-Kortum *et al*, 1989, 1991, Cotheren *et al*, 1990, Kapadia *et al*, 1990, Lucas *et al*, 1990, Anderson-Engels *et al*, 1991, Hung *et al*, 1991, Palcic *et al*, 1991, Schomacker *et al*, 1992, Lam *et al*, 1993). In this thesis, a complete study on the spectroscopic characteristics of skin autofluorescence was carried out using both UV and visible light excitation.

Tissue autofluorescence has many different characteristics when compared to fluorescence from low concentration solutions. Tissue reabsorption and scattering will distort the shape of fluorescence spectrum (Anderson 1989, Keijzer *et al*, 1989b, Richards-Kortum *et al*, 1989, 1989b). Ignoring these characteristics may lead to incorrect interpretation and inappropriate use of the fluorescence spectra. For example, Alfano *et al* (1987) interpreted two peaks at 554 nm and 600 nm on the lung tissue autofluorescence spectra to be originating from melanins and porphyrins respectively. But these two peaks are actually due to the blood absorption because, beside the two peaks, there are two valleys located at 540 nm and 580 nm which correspond to the oxyhaemoglobin α- and β- absorption bands. For comments on the inappropriate use of the *in vivo* skin autofluorescence for photoaging study by Leffell *et al*,

(1988), see Anderson 1989. More recently, theoretical studies have been initiated to calibrate the distortion of tissue fluorescence spectra (Richards-Kortum *et al,* 1989b, Gardner *et al,* 1993). We proposed a combined autofluorescence and diffuse reflectance measurement to assist the correct interpretation of skin autofluorescence spectra (Zeng *et al,* 1992, 1993). This idea was further explored in this thesis.

Tissue fluorescence measurements are complicated by tissue optical properties in two aspects: (1) absorption and scattering will lead to a non-uniform distribution of excitation light inside the tissue, therefore, different regions will have different excitation intensity; (2) when fluorescence light escapes from the tissue, it will be modified by the tissue scattering and absorption again, fluorescence sources located at different depths will have different escape efficiencies. Very recently, these processes have drawn the attention of some theoretical workers. Monte Carlo simulation was used to model these processes (Keijzer *et al,* 1989b, Crilly *et al,* 1992, Gardner *et al,* 1993, Tinet and Avrillier, 1993). However, these researches all assumed uniform fluorophore distribution in a semi-infinite medium or used average fluorophore distribution derived from macroscopic measurements. This is far from reality in the tissue. In this thesis, the natural fluorophore distribution and spectral differences in skin tissue was determined by using a novel microspectrophotometer (MSP) developed by us specifically for this work (Zeng *et al* 1993b, 1993c). The Monte Carlo

simulation was then used to model the excitation light distribution in and autofluorescence escape from skin tissue based on such obtained experimental data.

When performing *in vivo* skin autofluorescence measurements, we noted that the fluorescence signal decreases during continuous laser exposure (Zeng *et al*, 1993d). We postulated that the decay dynamics of skin autofluorescence are determined by (1) the excitation light distribution pattern in skin tissue, (2) the number of fluorophore types and their chemical environments, (3) the escape process of fluorescence light, and (4) that the non-invasive measurement of the decay dynamics may be used to determine various information about the skin, especially, to determine the fractional contributions of different skin layers to the total *in vivo* autofluorescence signal. In this thesis, the autofluorescence decay dynamics, which has never before been reported by others, was measured quantitatively and analyzed mathematically. The above postulates were then examined and elaborated in detail by combining the *in vitro* microscopic, *in vivo* macroscopic measurement results and theoretical modeling.

1.2 Objective and outline of this dissertation

The primary objective of this thesis was to test the hypotheses: (1) that skin optical properties can be quantitatively modeled and (2) that *in vivo* spectroscopic measurements can be used to derive information about skin

structures. Both theoretical and experimental procedures were used to test these hypotheses. A computerized autofluorescence and diffuse reflectance spectroanalyser system was built using fiber optics and optical multichannel analyzer (OMA), allowing very rapid spectra acquisition. A combined diffuse reflectance and auto-fluorescence measurement procedure was implemented to assure correct interpretation and calibration of the autofluorescence spectra. A novel fiber alignment mechanism was designed and developed to construct a unique microspectrophotometer (MSP) system for measuring the microscopic distribution of natural fluorophores in the skin tissue and their intrinsic fluorescence properties. A skin optical model was developed and Monte Carlo simulation was used to model the light distribution as well as fluorescence escape from the model skin.

This dissertation consists of five chapters. Chapter 1 is an introduction (this chapter) which gives the background of this thesis and a review of skin tissue optical property studies. Chapter 2 describes the methodology of experimental measurements and theoretical modeling. Chapter 3 presents the spectroscopic properties of human skin obtained by macroscopic *in vivo* measurements. Chapter 4 is dedicated to understanding the dynamics of skin autofluorescence decay. Microscopic *in vitro* measurement results on excised skin tissue sections are presented. A skin optical model is developed and Monte Carlo simulation is used to solve the Boltzmann equation of radiative transfer for the model skin. Finally the physical meaning of

the autofluorescence decay dynamics is elucidated. The thesis hypotheses were proven to be positive. Chapter 5 is the conclusion of this dissertation. The major progress in understanding skin optics is summarized and future research directions are discussed.

CHAPTER 2: METHODOLOGY OF EXPERIMENTAL MEASUREMENTS AND THEORETICAL MODELING

2.1 Combined autofluorescence and diffuse reflectance spectro-analyser system

When starting this thesis research, we found that in the literature, the autofluorescence and diffuse reflectance methods are used separately in skin and other tissue optics studies. However, tissue reabsorption and scattering distort the shape of fluorescence spectrum. We, therefore, proposed a combined autofluorescence and diffuse reflectance measurement procedure so that we can use the reflectance spectrum to assist the correct interpretation or calibration of the fluorescence spectrum (Zeng *et al*, 1992, 1993). We employed fiber optic sampling and OMA techniques to realize this procedure. By choosing a high-gain microchannel plate intensified photo-diode array (PDA) detector for spectrum detection and large core diameter (1 mm) fibers for both illumination and signal pick-up, we detected measurable autofluorescence from skin *in vivo* when excited by a conventional light source (1000 W xenon lamp) instead of a laser. The same light source is bright enough for diffuse reflectance measurements. A specially designed fiber holder was used to hold the two fibers and is suitable for both types of spectroscopy. For quantitative measurements, we employed a microcomputer controlled EG&G OMA and chose a 14-bit A/D converter to obtain a large dynamic range. The

reproducibility of the reflectance spectrum obtained by this system was measured to be better than 0.7%.

2.1.1 Materials and methods

Two 1 mm core diameter fused silica fibers (3M company, spectral transmission range: 200 nm to 2400 nm, N.A. = 0.18) were used to deliver illumination light and to collect reflected light or fluorescence light. A special fiber holder was designed to hold these two fibers; figure 6 shows the side view and the top view of the fiber holder. The two fibers were mounted on two quarter circle arms which are co-centered so that they always project to the same point on the skin surface. The two fibers could be moved along the two quarter circle arms in the range of 0 to 90 degrees with some limitations (shown in figure 6) at the two ends due to the size of the fiber clip. The two quarter circle arms could move along the bottom supporting ring in the range of 0 to 360 degrees. Therefore, the two fibers could be set over almost any angular position in the three-dimensional space. The distance from the fiber tip to the skin surface could also be set such that the spot size of the illumination light and the sampling area of the detection fiber could be changed as desired.

Figure 7 shows the set-up of the spectroanalyser system, which consists of a tunable light source, fiber holder, OMA, and a computer. The tunable light source (PTI A5000) is a

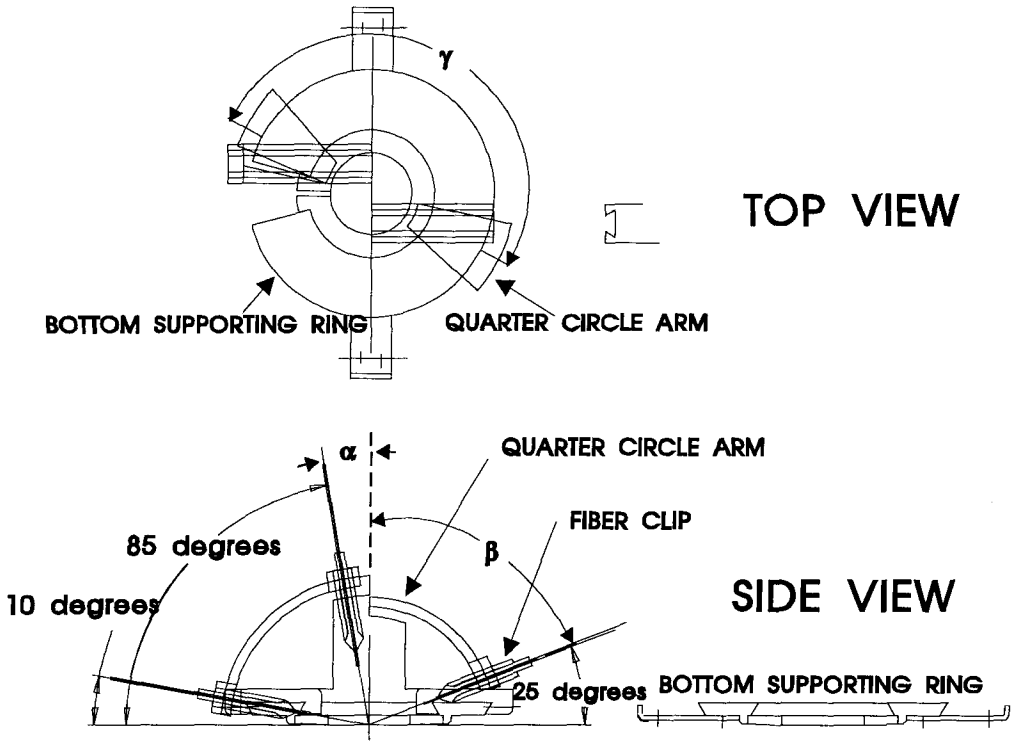

Figure 6. Top view and side view of the fiber holder.

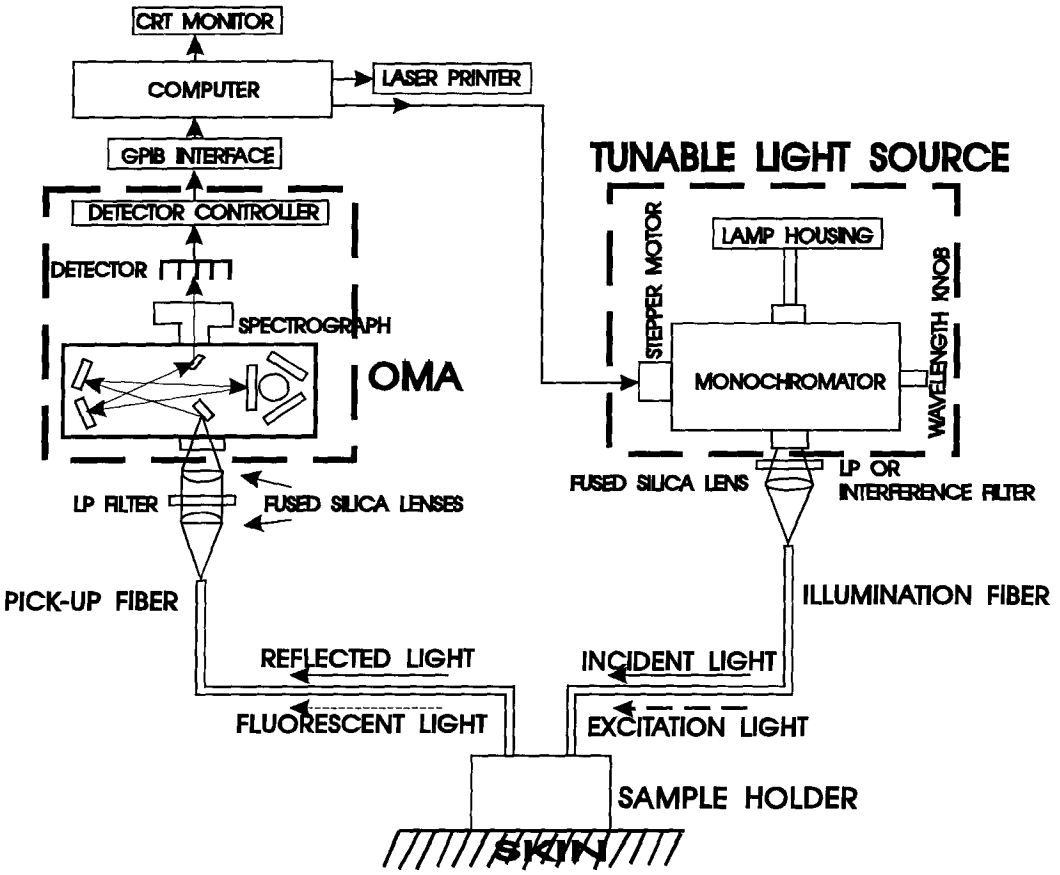

Figure 7. Set-up of the spectroanalyser system for combined autofluorescence and diffuse reflectance measurements.

1000 W xenon lamp plus a monochromator to select the wavelength. The emission spectrum range of the xenon lamp is from 200 nm to 1100 nm. The monochromator provide a narrow bandwidth output when used for autofluorescence measurements. The wavelength could be adjusted manually or by the computer through a stepper motor. The light from the monochromator was focused onto a 1.0 mm fiber which was used to illuminate the skin. Reflected light or fluorescence light from the skin was collected by the detection fiber in the fiber holder and transmitted to the fiber adapter on the OMA. The collected light was then focused onto the entrance slit of the spectrograph (Jarrell-Ash Monospec 27), with a 150 grooves/mm grating, blazed at 450 nm, yielding a 0.59 nm/element sampling density. A 25 μm entrance slit was used. The spectral resolution was measured to be 1.5 nm FWHM (full width at the half maximum). The detector is an intensified 700-element silicon linear diode array (EG&G PARC, model 1455R-700HQ, response wavelength range: 200 nm - 900 nm). The detector was interfaced to the computer through the model 1461/2 detector interface/controller with a 14-bit analogue-to-digital converter. The actual measurement wavelength range could be changed by adjusting the grating in the spectrograph. A 400 nm measurement window can be covered by this detector, grating combination. The whole spectrum curve in the 400 nm window is acquired simultaneously by the linear array detector. The computer performs the data storage, spectral display/processing, and spectrum printout.

The effects of dark noise in the detector were reduced by background subtraction using the OMA software. Spectral calibration was performed using a known spectrum of a low-power, low-pressure mercury-argon lamp (Oriel Corporation, model 6035). When performing fluorescence measurements, intensity calibration was made using the EG&G Gamma Scientific RS-10 standard lamp and the supplied spectral data. The intensity calibration enabled the calibration of the wavelength dependence of the response of the complete system.

When measuring autofluorescence, the system was set up as follows:

(1) the monochromator was used to select the excitation wavelength;

(2) a corresponding interference band pass filter was inserted after the exit slit of the monochromator to suppress the stray light; and

(3) a long pass filter was placed into the OMA fiber adaptor to block the reflected excitation light.

At times, the illumination fiber was connected to a 442 nm He-Cd laser which was also used for tissue autofluorescence excitation. The fiber holder was placed onto the skin site of interest and by changing the gain of the detector and the exposure time (typically 1 second), good quality fluorescence spectra (displayed in near real time on the CRT screen) could be obtained, calibrated, and stored.

Fluorescence spectrum data are presented in the literature by plotting intensity values using either the dimension of

power (e.g. in the unit of mW), which we denoted as $I(\lambda)$, or photon counts per unit time, which we denoted as $I_c(\lambda)$. $I(\lambda)$ and $I_c(\lambda)$ curves will have different shapes according to the relationship:

$$I_c(\lambda) \propto I(\lambda)/h\nu \propto \lambda I(\lambda) \quad (9)$$

where λ is the wavelength, ν the frequency of light, and h is Planck's constant. For quantitative measurements, we performed intensity calibration and chose to use $I_c(\lambda)$ with the unit of "fluorescence photon counts per unit time (arbitrary units)" or briefly "photon counts (a.u.)".

When measuring diffuse reflectance, the system was set up as follows:

(1) the monochromator was set to allow zero-order white light to pass through;

(2) a long pass filter was placed at the output port of the monochromator to block out harmful UV radiation and /or to select the short-wavelength end of the spectrum measurement window.

For quantitative measurements of diffuse reflectance, a reference spectrum was first collected using a standard disc with constant reflectance, independent of the wavelength, then the collection of the spectra from the selected skin site followed. The division of the skin spectrum by the reference spectrum gives the diffuse reflectance spectrum. Direct regular reflection from the surface can be avoided by placing the detection fiber at an angular position different from the specular reflection direction of the incident light.

An Oriel certified standard disc of diffuse reflectance (Oriel Corporation, Model 70496) was used as the reference material for diffuse reflectance measurements. This disc has constant reflectance over a wide wavelength range (from 250 nm to 2500 nm), and is an almost perfect Lambertian diffuser. It is more durable than traditional thick barium sulphate coatings or magnesium oxide blocks (Oriel Manual).

Unless mentioned otherwise, in our measurements, the illumination fiber was set to be 5° from normal (α = 5°); the pick-up fiber was 30° from normal (β = 30°); while the two quarter circle arms were set to be perpendicular to each other (γ = 90°). In this way, the regular reflection due to the refractive index mismatch at the air-skin boundary was avoided.

To test the reliability of the system, we performed 50 repeating measurements at a fixed skin site. Figure 8 shows the 50 reflectance curves. At the wavelength of 540 nm, the reflectance values from the 50 curves were read and the mean and the standard deviation were then calculated. The ratio of the standard deviation to the mean (the coefficient of variation) was 0.7%.

2.1.2 Demonstration of autofluorescence spectrum distortion by tissue reabsorption

Figure 9(a) shows the autofluorescence spectra of a hyperkeratotic skin (HKS) from a Chinese volunteer's finger and its surrounding normal skin. Also shown is a spectrum

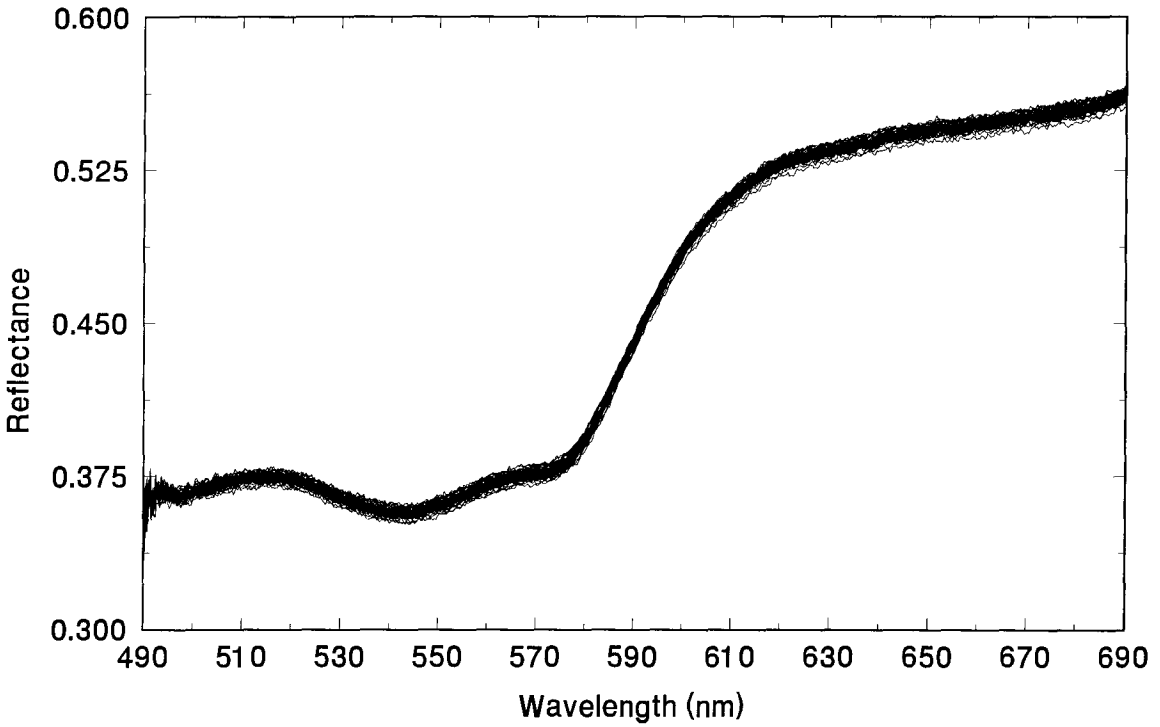

Figure 8. 50 diffuse reflectance curves obtained by repeating measurements at a fixed skin site.

a)

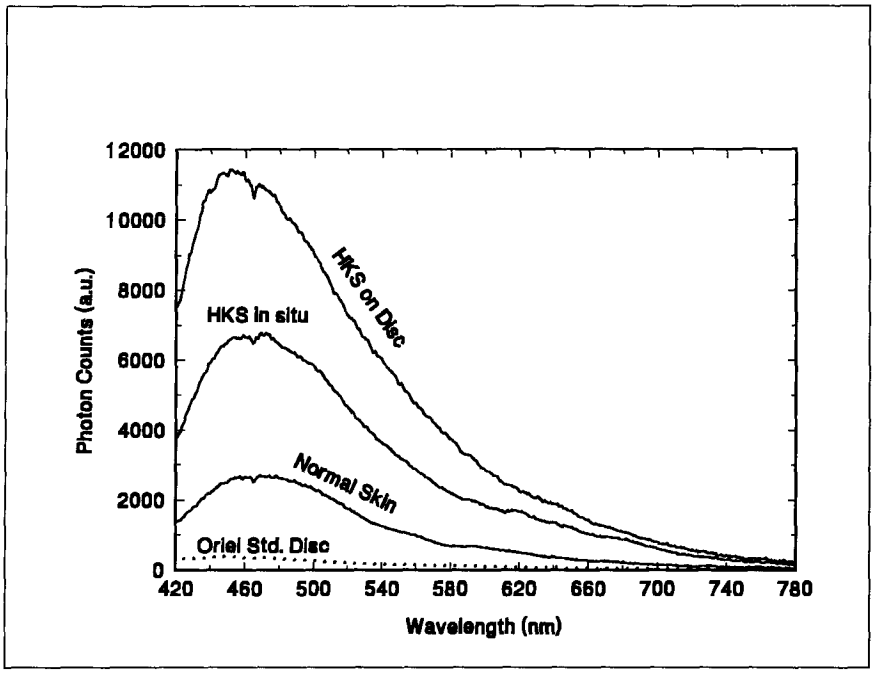

b)

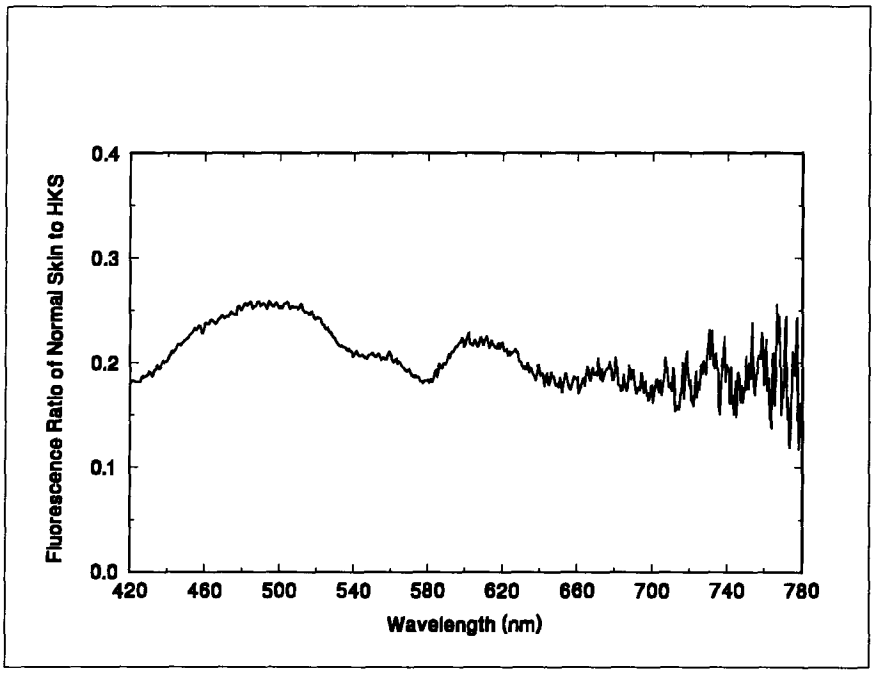

Figure 9. (a) Autofluorescence spectra of a hyperkeratotic stratum corneum (HKS) on a Chinese volunteer's finger and its surrounding normal skin. The excitation wavelength is 380 nm. (b) Ratio spectrum of the autofluorescence of normal skin to that of the HKS on an Oriel standard disc.

measured from a slotted scar plaque of hyperkeratotic stratum corneum placed on the Oriel standard disc. Comparing the spectrum for the HKS to that of the normal skin, we found that although the respective maxima are at the same wavelength (470 nm), the shapes of the spectra are quite different. The spectrum of the HKS is quite smooth, while for the normal skin spectrum, a small shoulder is evident at 600 nm. This shoulder might be interpreted as coming from an additional fluorophore. The results of the division of the normal skin spectrum by the HKS spectrum suggest that the shape difference may be caused by the skin tissue reabsorption of the fluorescence light. Figure 9(b) shows the ratio spectrum of the autofluorescence of normal skin to that of the HKS. The two oxyhaemoglobin absorption valleys are now clearly seen. There was no blood, therefore, no haemoglobin in the HKS; the small shoulder at 600 nm on the normal skin spectrum was caused by the strong haemoglobin absorption.

2.2 The novel microspectrophotometer system based on a fiber optic alignment mechanism

To study the microscopic morphology and spectroscopy of *in vitro* skin tissue sections, a microspectrophotometer (MSP) was needed. This is a microscope with a capability of measuring the spectroscopic properties of selected, localized areas of microscopic objects as small as a few microns. MSPs have been developed and used in biological and biophysical studies for

many years. Examples include cell staining (Wied *et al,* 1969, Holmquist *et al,* 1976, Galbraith *et al,* 1979, Halaby and Vance, 1979, Turner *et al,* 1990), spectral response measurements of photoreceptor cells and visual pigments (Knowles and Dartnall, 1977, MacNichol, 1977, Archer and Lythgoe, 1990, Bowmaker *et al,* 1991, Govardoviskii *et al,* 1991), lateral diffusion studies of visual pigments (Gupta and Williams, 1990), enzyme activity monitoring in tissue sections (Lomax *et al,* 1989), characterization of the fluorescent morphological structures in human arterial wall (Baraga *et al,* 1991), measurement of optical density of vascular tissue (Schwarzmaier *et al,* 1992), cellular bioluminescence (David and Galbraith, 1975) and cellular fluorescence measurements (Caspersson *et al,* 1965, Moser *et al,* 1992, Schneckenburger *et al,* 1992, Seidlitz *et al,* 1992, Wessels *et al,* 1992,). However, all existing MSPs have in common a need for a structure in which specially designed alignment optical and photometric measurement parts must be mechanically attached to the microscope. Commercialized attachments are only available from E. Leitz and Carl Zeiss for a number of their microscopes (Richardson, 1991). For this thesis, we developed and built an easy-to-construct and easy-to-use MSP system based on a novel fiber alignment mechanism (Zeng *et al,* 1993b).

2.2.1 MSP system configuration

Figure 10 shows the setup of the MSP system. Its major components are a microscope (Nikon), an OMA, a CCD video camera (Sony), and a computer. It has all the functions of a conventional microscope plus the ability to perform spectral analysis on selected micro areas of a microscopic sample.

The sample for examination is placed on the microscope stage. The microscope has its own white light illumination setup (Halogen lamp, mirror M1, condenser, etc.) which can be used for transmittance or absorbance measurements. For fluorescence measurements, a 442 nm He-Cd laser light was conducted to the microscope for excitation illumination through a 100 μm optical fiber which has a microlens on its output end. A 470 nm long pass filter was inserted after the objective to block transmitted laser light while passing long wavelength fluorescence light. The white light image or fluorescence image of the sample was formed on the image plane indicated in figure 10 and was also visible through the eyepiece. Optionally, the image could be deflected by a movable mirror (M2) and focused onto a CCD video camera which was connected to an image processing board (Matrox Electronic Systems Ltd.) in the computer. Therefore, images could be acquired by the computer for storage and/or further processing.

An optical fiber was mounted into one of the image planes of the microscope to collect light from a specific micro area of the sample. The collected light is transmitted via the

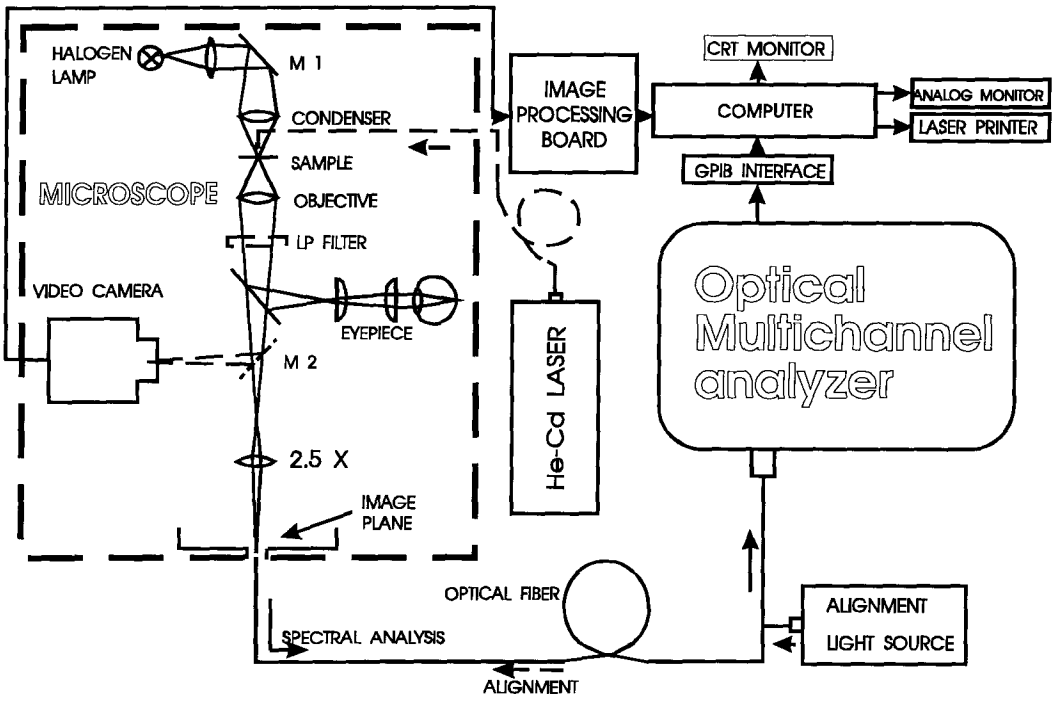

Figure 10. Setup of the microspectrophotometer system based on a novel fiber optical alignment mechanism.

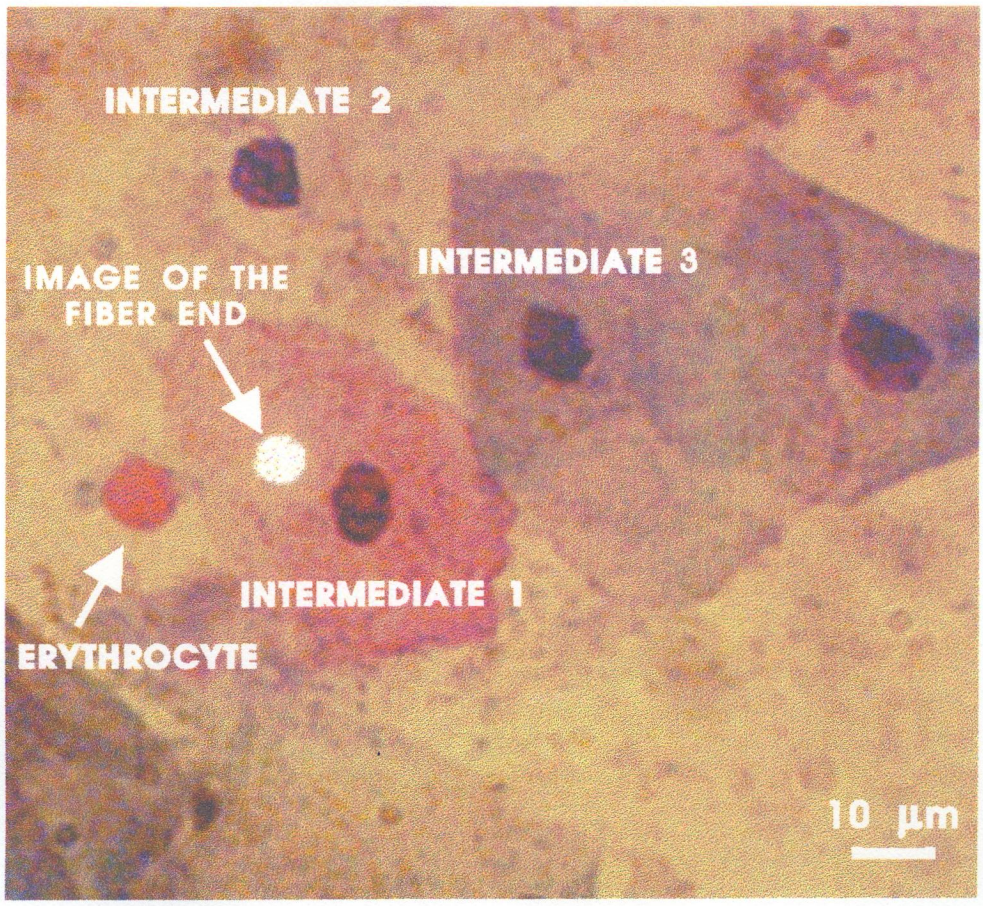

Figure 11. Microscopic image of Pap-stained cervical cells.

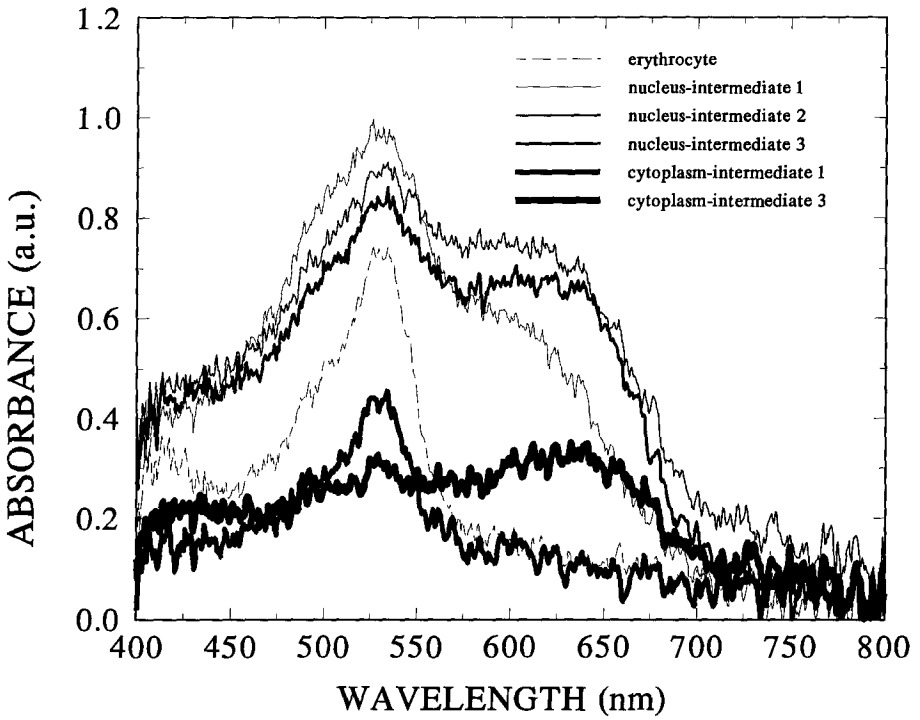

Figure 12. Absorbance spectra of the cytoplasm and nuclear areas of the Papanicolaou-stained cervical cells indicated in figure 11.

fiber to the OMA for spectral analysis. The same fiber can also be disconnected from the OMA port and then connected to an auxiliary light source to conduct light in the reverse direction into the microscope image plane. In this case, the end of the fiber becomes a bright object. Since the image plane is conjugate with the focused sample plane, according to the principle of reversibility of light, the bright fiber end is imaged onto the sample. This image of the fiber end is visible through the eyepiece as a bright circular spot. This bright spot is positioned exactly where the light collected by the fiber for spectral analysis will originate. One can move the stage to select the spot to be analyzed. Different core diameters of fibers can be used to change the size of the analysis area. The spectral analyses were performed by the OMA. The computer controls both the image and the spectrum data acquisition and processing. The acquired spectra and images were displayed in near real time on VGA monitor and RGB analog monitor, respectively.

2.2.2 Reliability test of the MSP system

To test the reliability of the MSP system, we measured the absorbance spectra of Papanicolaou-stained cervical cells smeared on a microscopic slide. Figure 11 shows an image of a part of a sample being analyzed. The bright circular spot is the image of the fiber end when it was placed into the image plane of the eyepiece and was connected to the auxiliary light

source. The mirror M2 (in figure 10) prevents simultaneous viewing and video camera recording when the fiber is in its usual position. An image was captured in this fashion to demonstrate the alignment principle. In practical measurements, the fiber was mounted into another image plane as shown in figure 10. Once the fiber is fixed, the position of the bright spot in the field of view is also fixed. The slide can then be moved such that different areas of the slide occupy this location and can be analyzed.

The microscope glass slides are optically homogeneous material; their transmittance is uniform from point to point and from slide to slide (Halaby and Vance, 1979). We verified this for slides used in our laboratory. To obtain the absorbance spectrum of a cell component, a reference spectrum was first recorded at any cell-free location on the slide, then a spectrum at a cell area of interest (nucleus or cytoplasm) was recorded. Division of the two spectra gave the transmittance spectrum, while the absorbance was obtained by calculating the negative value of the logarithm of the transmittance. The sizes of the nuclei shown in figure 11 were ~ 10 μm diameter. The detection fiber used had a 600 μm core diameter, the objective had a 60x magnification power, and the projection lens had a 2.5x magnification power. The resulting sampling spot diameter on the slide was 4.0 μm (600 μm/(60 x 2.5)) which was consistent with the measured value found through the eyepiece reticules. Figure 12 shows the measured absorbance spectra corresponding to the cytoplasm or nuclear

areas indicated in figure 11. The shapes of these spectra are in accordance with the colors seen under the microscope and are also consistent with those reported in the literature (Galbraith *et al,* 1979), proving the reliability of our MSP system.

In summary, our new MSP has the following characteristics comparing to conventional MSPs:

(1) it is easy to build, any kind of multi-port microscope can be used, and no special attachments for the microscope except for an optical fiber are needed;

(2) it is easy to use and to determine the sampling area due to the unique alignment mechanism; and

(3) it has a higher spectral resolution and shorter data acquisition time due to the OMA solid array detector. For comparison, conventional MSP systems acquire spectral data in 5 nm to 15 nm intervals (Holmquist *et al,* 1976, Halaby and Vance, 1979, Galbraith *et al,* 1979, Turner *et al,* 1990, Schneckenburger *et al,* 1992), while this system acquires data in 0.59 nm steps and has a spectral resolution of 1.5 nm FWHM when a 25 μm entrance slit is used.

2.3 Method for quantitative monitoring of CW laser induced changes in autofluorescence of *in vivo* skin

2.3.1 Experimental setup

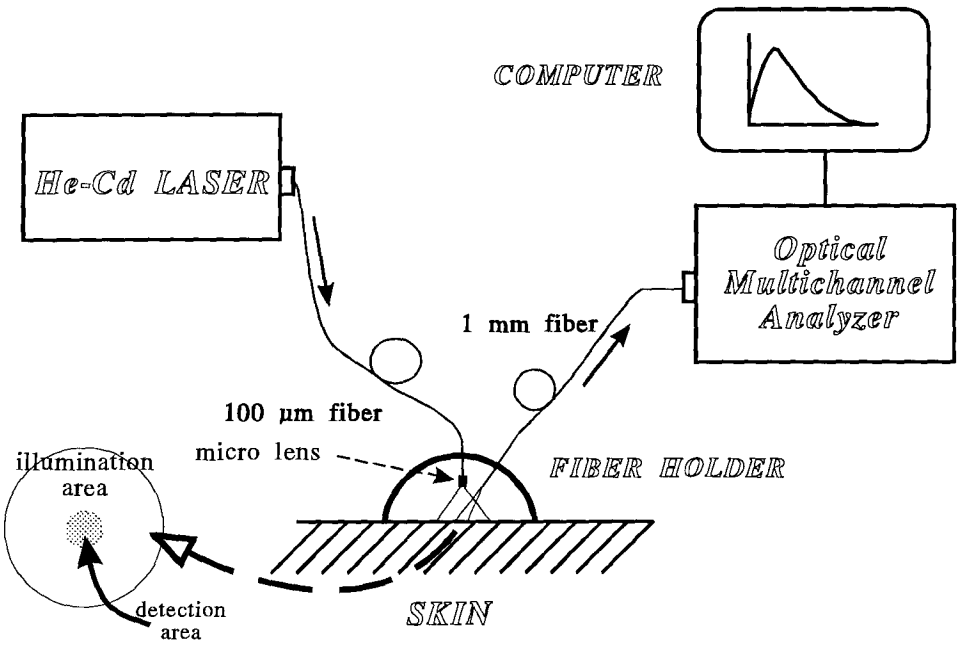

Figure 13. Spectroanalyser system configuration for quantitative monitoring of laser induced autofluorescence decay.

The measurements of *in vivo* skin autofluorescence decay during continuous laser exposure were carried out by using the spectroanalyser system described in section 2.1. Figure 13 shows the system configuration and some modifications for this purpose. A 100 μm core diameter fiber with microlens was used to conduct a 442 nm He-Cd laser light to continuously illuminate the selected skin site. The microlens attached to the fiber was used to achieve uniform illumination. The excited autofluorescence light was collected by a large core (1 mm) diameter fiber and transmitted to the OMA for spectral analysis. The two fibers were held by a fiber holder which keeps the two fibers co-centered and allows the illumination and detection angles to be varied. The distance from the fiber tip to the skin surface, and therefore, the illumination spot size and the detection area size may also be easily adjusted as desired. A 470 nm long pass filter was inserted into the light path on the OMA side to block the scattered excitation laser light while allowing the longer wavelength fluorescence light to pass through. During laser induced autofluorescence decay experiments, the computer controlled OMA was programmed to acquire the autofluorescence spectra at constant time intervals with a constant exposure time. Typically, for each spectrum, we selected a 5 second exposure time. The data transfer took 0.51 seconds, thus the time interval (or sample time) between each spectrum was 5.51 seconds. For each skin site, 120 spectra were obtained continuously in about 11 minutes

(5.51 sec. x 120). All 120 spectra were stored in a single file for further processing.

2.3.2 Methods for removing signal fluctuations

During a period of 11 minutes of data acquisition on *in vivo* human skin, it was impossible to assure that there were no relative movements between the fiber holder and the investigated skin site. Two measures were thus taken to reduce the measured autofluorescence signal fluctuations caused by the mentioned relative movements and the laser output power fluctuations:

(1) In order to minimize errors due to horizontal movements of the fiber holder, a large illumination spot (10 mm diameter) and a small detection spot (3 mm diameter) were selected to assure that the detected signal always came from a continuously exposed area even if the fiber holder were to move in a parallel direction to the skin surface. Before each experiment, a visual check was performed by viewing through a 480 nm long pass edge filter (Omega Corp.) at the uniformly illuminated area to select a uniformly fluorescing skin site for the laser exposure.

(2) Vertical movements of the fiber holder relative to the skin surface could change the fluorescence collection efficiency and therefore, cause the measured fluorescence signal to fluctuate. We found that during the whole laser exposure processes, the diffuse reflectance of the exposed skin

did not change significantly. Two observations support this. First, the laser peaks appeared on the 120 fluorescence spectra showed no significant increasing or decreasing trends, but fluctuations always existed. Second, in the white light (diffuse reflectance) images of the exposed area, there were no visible or measurable intensity and color changes between the exposed area and the surrounding unexposed area. In addition, Kollias (1984) reported that to bring pigmentation (color) changes of human skin, *in vivo*, with visible and IR light irradiation, a minimum exposure intensity of 200 mW/cm^2 and 15 minutes of exposure time are needed. We used a maximum exposure intensity of 64 mW/cm^2 and a exposure time of 11 minutes. Therefore, if the vertical movements of the fiber holder or the intensity changes of the excitation laser light were to affect the fluorescence detection efficiency, they should affect the diffuse reflectance detection efficiency by the same amount. Hence, the ratio of the fluorescence signal to the laser peak signal (there is always a very small signal of scattered laser light that passes the LP filter, appropriate LP filter was chosen to make the laser peak comparable with the autofluorescence signal.) cancels the fluctuations caused by the laser power fluctuation and the relative movement between the fiber holder and the investigated skin site.

2.3.3 Data processing

The data processing was completed in two steps:

(1) A program was written to read the data file containing the 120 spectral curves, to calculate the intensity value of the laser peak (denoted as a_0) and the area a_i under the spectral curve over a certain wavelength band (i.e. 10 nm) surrounding a selected central wavelength λ_i for each of the 120 spectral curves. In one run, the program can calculate 12 a_i at 12 different wavelength λ_i. The ratio a_i/a_0 was then calculated and divided by the a_i/a_0 value of the first spectrum curve to normalize the maximum a_i/a_0 to 1. We denoted the normalized a_i/a_0 quantity by I(t). I(t) is a function of time and represents the autofluorescence decay. Figure 14 illustrates this data processing step graphically. Figure 14a shows the original data containing the 120 spectral curves. Figure 14b shows the laser peak intensity (a_0) change as a function of time. Figure 14c shows the calculated area a_i of a selected wavelength band decay with increasing time, significant fluctuations can be seen on this curve. Figure 14d is the a_i/a_0 ratio versus time curve. This curve is much smoother than that in figure 14c and is denoted as the I(t) curve.

(2) The I(t) data was imported to the non-linear regression program of the BMDP software package (BMDP Statistical Software, Inc.) for exponential fitting. First, a single exponential fit was completed and residuals were checked. If the residuals were not randomly distributed, a double exponential fit was carried out, and residuals were checked again. The number of exponential terms were increased until a random residual distribution was achieved and a good

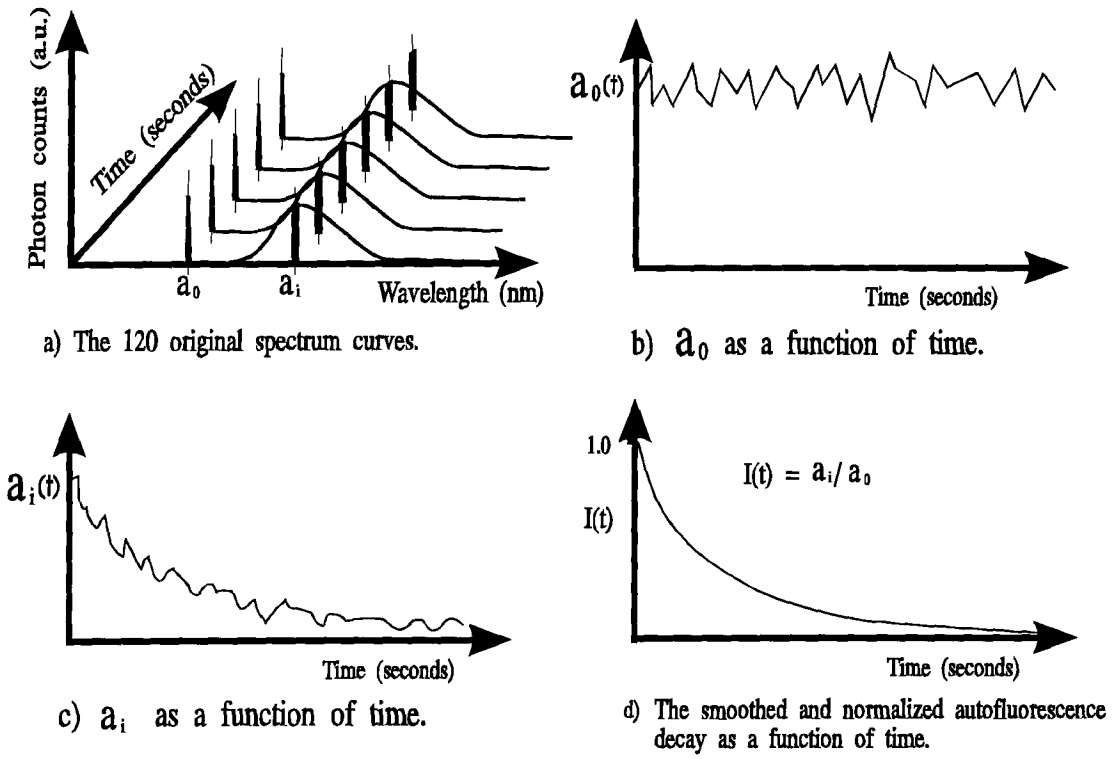

Figure 14. Data processing steps to generate a smooth I(t) curve.

fit was obtained. After that, one more fit was attempted with one additional exponential term, and the residual distribution and fit were checked. Usually, this additional term fitting yielded a poor fit, confirming the previous fitting as the best one.

2.3.4 Method for monitoring the autofluorescence recovery after laser exposure

For short term monitoring of the autofluorescence recovery, autofluorescence spectrum measurements were performed immediately after the laser exposure was terminated. For long term monitoring, autofluorescence imaging methods were used. The setup of the imaging system is shown in figure 15. A uniform illumination was achieved by the same optical fiber as shown in figure 13. A small hole was drilled on the camera lens shield to let the fiber pass through. An adjustable support bar was attached to the shield to hold the fiber and adjust its position. The autofluorescence image was acquired by a Sony 3-chip CCD color camera. A 480 nm long pass edge filter (Omega Corp.) was used to cut out the scattered laser light so that it did not interfere with the fluorescence imaging. The images were digitized by an image processing board (Matrox Electronic System Ltd.) and displayed on an RGB analog monitor under the control of a computer. Immediately after terminating the laser exposure, the exposed skin site was seen as a dark but detectable circular spot in the fluorescence

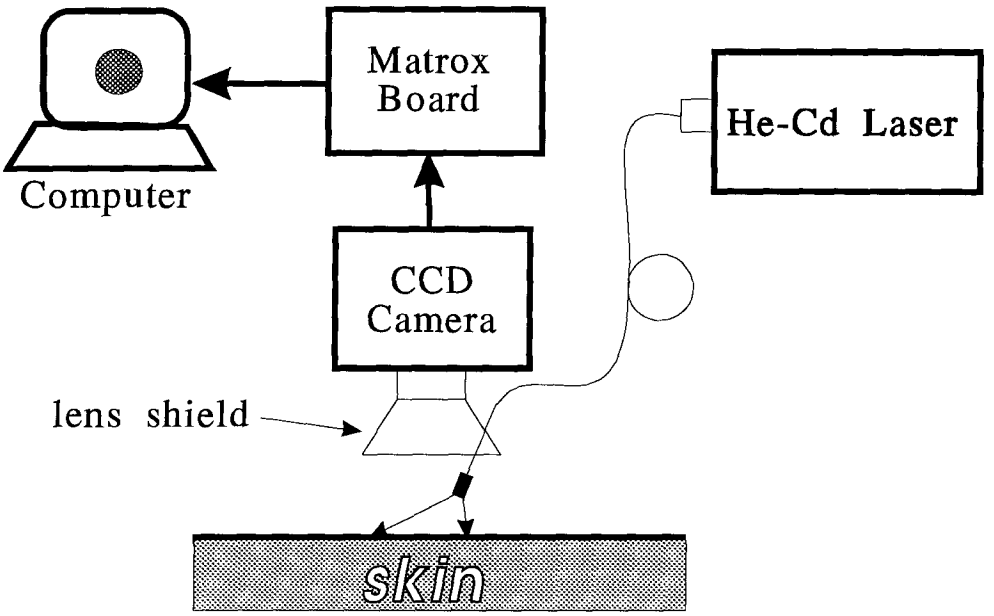

Figure 15. Autofluorescence imaging system for monitoring *in vivo* skin autofluorescence recovery after laser exposure.

image. During the recovery process, this dark spot eventually became as bright as the surrounding tissue.

2.3.5 Safety consideration of the experiments

The maximum illumination power density used in these experiments was 64 mW/cm^2 at 442 nm for 11 minutes exposure. This is unlikely to be harmful to human skin because the total power density at the earth's surface of 400 nm to 500 nm sunlight is estimated to be 14 mW/cm^2 and the power density required to burn skin is 420 mW/cm^2 (Tregear, 1966). In addition, the 442 nm wavelength is well away from the carcinogenic UV light bands. We also monitored the temperature rise of the exposed skin site during the laser exposure. The temperature rise was less than 0.2 °C as measured by a thermo-couple and therefore, no harmful thermal effects were generated.

2.4 Radiative transfer theory and Monte Carlo simulation of light propagation in biological tissue

Historically, the problem of wave propagation in random media has been investigated theoretically from two distinct points of view (Ishimaru, 1978). One is "radiative transfer theory" or "transport theory", and the other is "multiple scattering theory" or "analytical theory". Analytical theory starts with basic differential equations such as the Maxwell

equation, obtains solutions for a single particle, introduces the interaction effects of many particles, and then considers statistical averages. It is mathematically rigorous in the sense that in principle, all the multiple scattering, diffraction, and interference effects can be included. However, practically, it is almost impossible to obtain the exact properties of all skin components. It is mathematically difficult to treat their multiple scattering interactions because skin is irregularly shaped, has hair follicles and glands, is inhomogeneous, multi-layered, and has anisotropic physical properties. Radiative transfer theory, on the other hand, deals with the propagation of intensities. It is based on phenomenological and heuristic observations of the transport characteristics of intensities. The basic differential equation is called the transport equation and is equivalent to Boltzmann's equation in the kinetic theory of gases and in neutron transport theory. To determine the light propagation in tissue by the transport equation, only the average absorption coefficient μ_a, scattering coefficient μ_s, and the scattering phase function $p(\theta)$ are needed. These parameters can be measured experimentally. The transport theory has been found very useful in tissue optics studies. The following is a detailed description of the transport theory and the Monte Carlo simulation method for numerical solutions of the transport equation.

2.4.1 Transport theory

A basic quantity in the transport equation is the specific intensity or radiance $L(\mathbf{r},\mathbf{s})$ which denotes the average power flux density within a unit solid angle along direction $\mathbf{s}$, at position $\mathbf{r}$, and has the unit $W/cm^2/sr$. The flux density vector $\Phi(\mathbf{r})$ (its quantity is the fluence or radiant flux rate per unit area) is related to $L(\mathbf{r},\mathbf{s})$ by

$$\Phi(\mathbf{r}) = \int_{4\pi} L(\mathbf{r},\mathbf{s})\,\mathbf{s}\, d\omega \qquad (10)$$

where $d\omega$ is the differential solid angle.

If a specific intensity $L(\mathbf{r},\mathbf{s})$ is independent of the direction $\mathbf{s}$, then the radiation is said to be "isotropic". If the specific intensity radiated from a surface *da* is isotropic, then the power *P* radiated from this surface *da* in the direction $\mathbf{s}$ is given by

$$P\ (W\ sr^{-1}) = (L da)\ \cos\theta = P_0\ \cos\theta \qquad (11)$$

where θ is the angle between the direction $\mathbf{s}$ and the normal to the surface *da*. This relationship (Eq.11) is called Lambert's cosine law.

Although the transport theory ignores the wave properties of the radiation, the radiance can be proven to be the sum of all Poynting vectors whose tips are located within a solid angle in the direction $\mathbf{s}$ and related to the mutual coherence function used in the analytical theory through a Fourier transform. This also means that even though transport theory was developed on the basis of the addition of powers, it

contains information about the correlation of the fields (Ishimaru, 1978).

The transport equation reads:

$$(\mathbf{s}\bullet\nabla)\,L(\mathbf{r},\mathbf{s}) = -(\mu_a + \mu_s)\,L(\mathbf{r},\mathbf{s}) + \mu_s \int_{4\pi} p(\mathbf{s},\mathbf{s}')\,L(\mathbf{r},\mathbf{s}')\,d\omega' + \varepsilon(\mathbf{r},\mathbf{s}) \quad (12)$$

where μ_a (cm^{-1}) and μ_s (cm^{-1}) are the absorption and scattering coefficients, respectively, $p(\mathbf{s},\mathbf{s}')$ is the phase function[2] representing the probability that a photon is scattered from direction **s** into direction **s'**. It depends only on the angle θ between **s** and **s'** assuming that the scatters are randomly distributed over the tissue volume. The Henyey-Greenstein phase function is a good approximation for skin tissue (Jacques *et al*, 1987b):

$$p(\theta) = \frac{1}{4\pi}\,\frac{1-g^2}{(1+g^2-2g\cos\theta)^{3/2}} \quad (13)$$

The integration in Eq. (12) is over all 4π steradians of solid angle in a spherical coordinate system. Eq.(12) is the result of energy conservation. The left side of the equation denotes the radiance change rate in the **s** direction. The first term of the right side denotes the losses in $L(\mathbf{r},\mathbf{s})$ per unit of length in the **s** direction due to absorption and scattering. The second term denotes the gain in $L(\mathbf{r},\mathbf{s})$ per unit of length in the **s** direction due to scattering from all other direction **s'**. The radiance $L(\mathbf{r},\mathbf{s})$ may also increase due to light emission

---

[2] The name "phase function" has its origin in astronomy where it refers to lunar phases. It has no relation to the phase of a wave. See Ishimaru, 1978.

(e.g. fluorescence emission) from within the volume ds. The $\varepsilon(\mathbf{r},\mathbf{s})$ denotes the power radiation per unit volume per unit solid angle in the $\mathbf{s}$ direction.

Eq. (12) is a local integro-differential equation. No general accurate analytical solutions are available for a turbid biological tissue with strong forward scattering properties. The most successful approximation method is the diffusion theory. However, it is a good approximation only when scattering dominates over absorption and deals with situations far away from the light source and boundaries. For details in diffusion theory, see references in Chapter 1. However, Monte Carlo simulation methods have been developed to obtain rigorous numerical solutions of the transport equation.

2.4.2 Monte Carlo simulation of light propagation in biological tissue

In Monte Carlo simulation, the step by step trajectories of individual photons in tissue are calculated by computer. Specifically, light is treated as non-interacting photon bundles, and tissue is stochastically identified by probability density functions for light attenuation, F(s), and direction of light scattering, $G(\psi)$ and $H(\theta)$:

$$F(s) = \mu_t \, exp(-\mu_t s) \tag{14}$$

$$G(\psi) = 1/2\pi \tag{15}$$

$$H(\theta) = \frac{1 - g^2}{2(1 + g^2 - 2g\cos\theta)^{3/2}} \tag{16}$$

In Eq. (14), s is the photon bundle pathlength between attenuation events, and μ_t (= μ_a + μ_s) is the total attenuation coefficient. In Eqs. (15) and (16), ψ and θ identify the new direction of the scattered photon in a spherical geometry. Here θ is the deflection angle, while ψ is the azimuthal angle. A computer generated random number is used to determine the probability of an event (F, G, H) occurring, and the probabilistic parameter (s, ψ, θ) is calculated. The photon bundle is propagated through the tissue by absorbing a fraction μ_a/μ_t of its "weight" after the bundle has traveled the pathlength s. The remaining weight is scattered in the new direction specified by ψ and θ, measured from the previous photon direction. Refractive index mismatched boundary conditions are handled by calculation of the Fresnel reflection coefficients, assuming unpolarized light:

$$R(\theta_i) = \frac{1}{2}\left[\frac{\sin^2(\theta_i - \theta_t)}{\sin^2(\theta_i + \theta_t)} + \frac{\tan^2(\theta_i - \theta_t)}{\tan^2(\theta_i + \theta_t)}\right] \qquad (17)$$

where θ_i is the incident angle of the photon onto the boundary (θ_i = 0 implies orthogonal incidence), θ_t is the deflection angle of the transmitted photon and is related to θ_i by Snell's law:

$$n_i \sin\theta_i = n_t \sin\theta_t \qquad (18)$$

with n_i and n_t being the refractive indices of the media. The photons are multiply scattered by tissue and phase and polarization are quickly randomized, and play little role in the energy transport.

The simulation program records the accumulated light power density, Q, in W/cm^3 that is deposited in a local tissue volume. The local light fluence Φ, in W/cm^2 is calculated using the local absorption coefficient μ_a, in cm^{-1}:

$$\Phi = Q/\mu_a \tag{19}$$

Φ represents the light distribution in tissue. The program also records where and in which direction the photons escape the air-tissue interfaces. Therefore, the local diffuse reflectance and transmittance as well as the total reflectance and transmittance can be obtained.

To model the autofluorescence measurements, the following procedure is used:

(1) Excitation light distribution

The distribution of excitation light within the tissue must be specified first. It is calculated using the Monte Carlo simulation, and is denoted as $\Phi(\lambda_{ex}, r,z,\theta)$ in W/cm^2. λ_{ex} is the excitation wavelength, while r, z, θ represent a local position in cylindrical coordinates.

(2) Intrinsic fluorescence coefficient, $\beta(\lambda_{ex},\lambda_{em},z)$

The intrinsic fluorescence coefficient β is defined as the product of the absorption coefficient due to the fluorophore , μ_{afl} (cm^{-1}), and the quantum yield Y (dimensionless) of fluorescence emission. Biological tissues usually have layered structure. In the same layer, β is constant, therefore, it can be denoted as a function of z, $\beta(\lambda_{ex},\lambda_{em},z)$. λ_{em} is the wavelength of emitted fluorescence light. The product $\Phi\beta$ yields the density of fluorescence source in W/cm^3. Using a

microspectrophotometer system, one can measure the relative β distribution in skin tissue.

(3) Escape function $E(\lambda_{em},r,z)$

Once a fluorophore emits a fluorescent photon, that photon must successfully reach the surface and escape to be observed. The escape function $E(\lambda_{em},r,z)$ is the surface distribution as a function of radial position (r) of escaping photons from a point source of fluorescence at depth z and radial position r = 0 within a tissue of thickness D. It also can be calculated by Monte Carlo simulations. The units of E are (W/cm^2 escape at surface)/(W of source point within tissue) which equals cm^{-2}. Simulations are conducted for a series of depth (z) inside the tissue, using the optical properties for the emission wavelengths of interest.

(4) Observed fluorescence, $F(\lambda,r)$

The observed flux of escaping fluorescence F in W/cm^2 at the tissue surface is computed by the following convolution (Keijzer *et al*, 1989b):

$$F(\lambda_{ex},\lambda_{em},r) = \int_0^D \int_0^{2\pi} \int_0^{\infty} \Phi(\lambda_{ex},r',z',\theta')\beta(\lambda_{ex},\lambda_{em},z')E(\lambda_{em},\sqrt{r^2+r'^2-2rr'\cos\theta'},z')r'\,dr'\,d\theta'\,dz' \qquad (20)$$

The convolution in Eq. (20) can be implemented numerically using discrete values for Φ and E that were generated by the Monte Carlo simulations, and the experimentally determined β.

For details of the implementation of the Monte Carlo simulation, see Prahl *et al*, 1989, Wang and Jacques, 1992,

Jacques, 1993 or the appendix at the end of this thesis. A simulation program of "Monte Carlo Modeling of Light Transport in Multi-layered Tissue in Standard C (MCML)" was obtained from The University of Texas M.D. Anderson Cancer Center and used as the starting point of our theoretical modeling. The MCML program can be used to calculate the fluence distribution inside skin tissue and the diffuse reflectance for a normal incident light beam on the tissue surface. We recalculated examples in the MCML manual and some published Monte Carlo simulation results in the literature to verify the correctness of this program before used it in our work. To calculate the fluorescence escape function, we modified the MCML program to simulate the light propagation process for a buried isotropic point source inside the tissue. Again, the correctness of the modified program was verified by comparing our results with those reported in the literature. We used an IBM 320 - RISK/6000 workstation to run the simulation program. Each run takes 3 to 5 hours depending on where the light source is located. Deep light sources have a longer simulation time.

CHAPTER 3: SPECTROSCOPIC PROPERTIES OF HUMAN SKIN

We measured the optical properties of *in vivo* normal skin on 8 volunteers in terms of diffuse reflectance spectra, autofluorescence spectra, and autofluorescence decay as a function of time during continuous laser exposure. These measurements revealed many important characteristics of human skin optical properties. Of them, the most interesting property is that laser induced skin autofluorescence decay follows a double exponential function. This property is discussed in great detail in this and the next chapter.

3.1 Diffuse reflectance properties of *in vivo* skin

Taking advantage of the fiber holder described in section 2.1.1, the diffuse reflectance spectra of different body locations were measured on volunteers at different illumination angle and detection angle combinations (when choosing a combination, we made sure that the specular reflection was avoided). In all measurements shown in this section and section 3.2, we used a small illumination spot and a large detection spot by varying the distances of the fiber tip to the skin surface. In this way, all the diffusely reflected light or fluorescence light at the detection angle direction were collected. For section 3.3, we used a large illumination area but small detection spot to reduce the measured signal fluctuations due to relative movements between the fiber holder

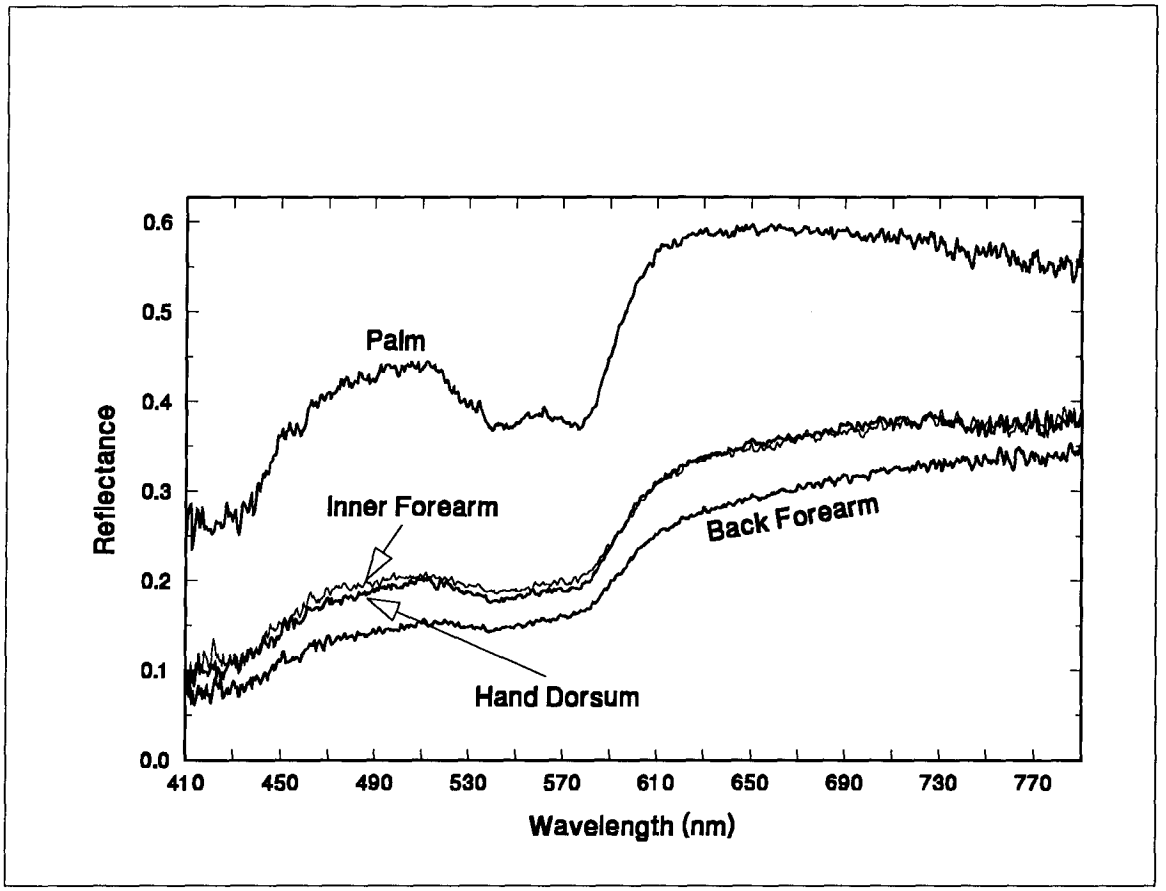

Figure 16. Normal skin diffuse reflectance spectra at different body locations of a Caucasian volunteer. All spectra were measured with illumination angle α = 5° and pick-up angle β = 30°; the two quarter circle arms were perpendicular to each other i.e. γ = 90°. Refer to figure 6 for the meaning of α, β, and γ.

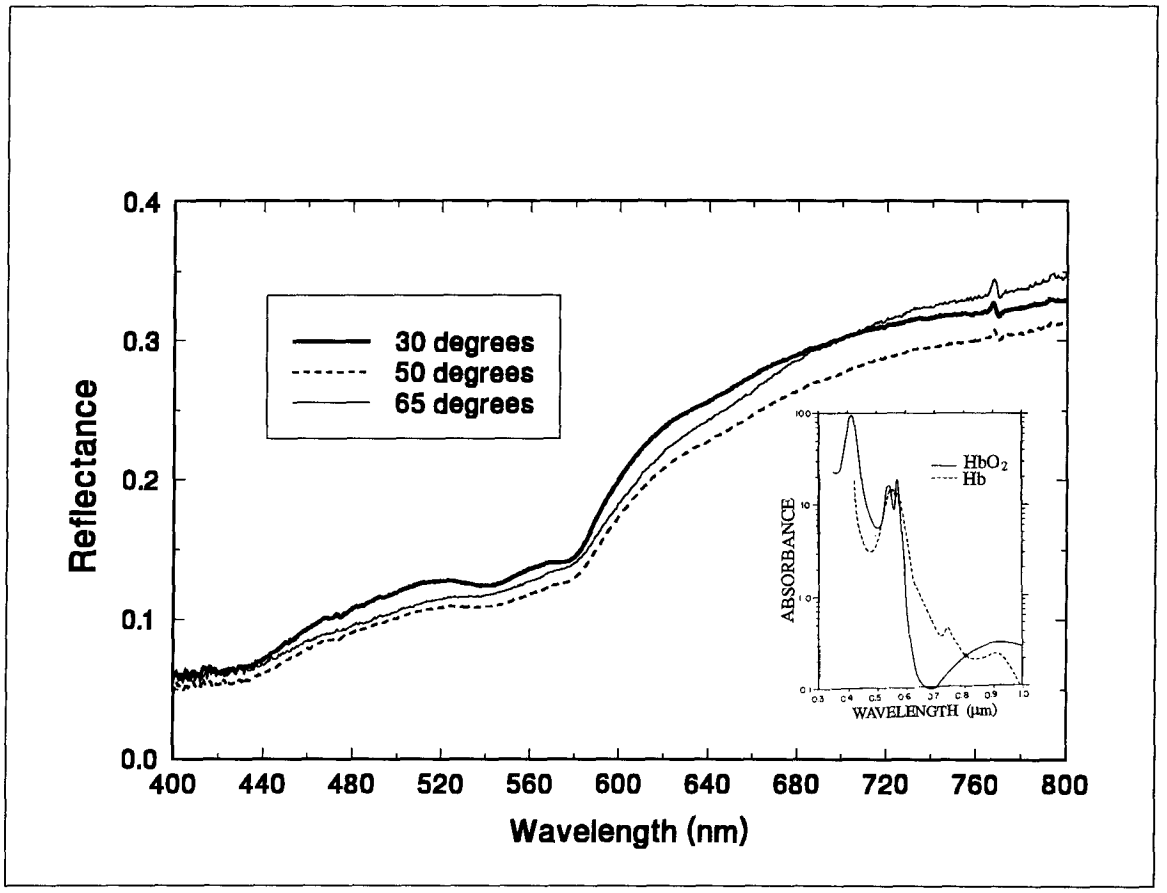

Figure 17. Diffuse reflectance spectra at a fixed illumination angle (α = 70°, γ = 90°) but different pick-up angles (β) measured from a Chinese volunteer's hand dorsum. The insert is the absorption spectra of the haemoglobin (Hb) and oxyhaemoglobin (HbO_2).

and subject being measured during longer (11 minutes) laser exposure period. The results show that the diffuse reflectance spectral curves from different body locations at a fixed illumination and pick-up condition are different in detail and that when changing the illumination and pick-up angles, the spectral curves can have different shapes.

Figure 16 shows normal skin diffuse reflectance spectra from four different body locations on a Caucasian volunteer. All four curves are different in detail, indicating that the amount of various absorption chromophores is a function of the body location. There are, however, some common characteristics. The two characteristic oxyhaemoglobin absorption valleys between 520 nm and 600 nm appear on all the four curves. The general trend of increasing reflectance with increasing wavelength reflects the effect of melanin absorption. However, the reflectance value of the spectrum curve for palm decreases slightly above 690 nm, differing from the other 3 curves where the reflectance values are relatively stable above 690 nm. This indicates that there is more oxyhemoglobin content on palm than on other locations: the increasing absorption of oxyhemoglobin above 690 nm (see figure 3) counteracts the decreasing absorption of melanin at this wavelength range and, therefore, causes the reflectance value of palm to decrease.

Figure 17 shows three reflectance curves obtained at a fixed illumination angle (α = 70°, γ = 90°), but different detection angle β. At β = 30°, the two oxyhemoglobin absorption

valleys between 520 nm and 600 nm are prominent and relatively deep. At 50°, the two valleys become shallower, while at 65°, they have almost disappeared as two independent valleys. Similar results were obtained for smaller α angles: the larger the α value, the more the spectral curve shape was changed. These results suggest that at small pick-up angles, the collected light come from deeper layers of the skin tissue, where haemoglobin absorption contributed more to the spectrum. At large pick-up angles, the collected light come from shallower skin layers. As the haemoglobin is more abundant in the deeper skin layers (the dermis), it did not contribute as much to the measured spectra. Therefore, by changing the illumination and detection angles, we could change the depth in the skin tissue from which the measurements of diffuse reflectance were made.

The fact that the 65° curve crosses over the 30° curve at about 690 nm (if normalized to 400 nm, the 65° curve also crosses over the 50° curve around this wavelength) further confirmed the above considerations. Because the oxyhaemoglobin absorption coefficient increases with wavelengths between 690 nm (see figure 3 and the insert in figure 17), the cross-overs at 690 nm suggest that blood absorption contributed more to the small angle reflectance curves. The blood absorption caused the diffuse reflectance curve to decline above 690 nm.

The strong forward scattering properties of the skin tissue may also play an important role in the above spectrum curve shape changes. Along with future progress in theoretical

studies of light propagation in multi-layered biological tissue, the diffuse reflectance at different illumination and pick-up angles $R(\alpha,\beta,\gamma)$ may be used as a fifth measurement modality to derive information from multi-layered tissue (like skin) *in vivo*. For other modalities, see chapter 1.

3.2 Autofluorescence properties of *in vivo* skin

We studied the autofluorescence spectra of the skin at different body locations for different illumination angle and detection angle combinations. The results show that on different body locations, the skin autofluorescence intensities had significant changes, but the spectrum maximum positions (wavelengths) had no significant variations, while the details of the spectrum shape did change as a consequence of tissue reabsorption of the fluorescence light and the variation of the amount of various absorption chromophores at different body locations. When the illumination and pick-up angles were changed, the detected autofluorescence intensities had significant changes, while the spectrum shapes did not show significant changes. This was different from the case of diffuse reflectance spectra and was probably due to the isotropic emission of fluorescence light. All data presented in the remaining part of this section were measured at the fiber holder settings of: $\alpha = 5°$, $\beta = 30°$, $\gamma = 90°$.

We measured the skin autofluorescence spectra at different excitation wavelengths (from 350 nm to 470 nm). The spectra at

Figure 18. Diffuse reflectance spectrum (a) and autofluorescence spectra (b - g) at different excitation wavelengths of an Asian volunteer's hand dorsum. In all fluorescence spectrum graph, solid line (———) denotes the measured original autofluorescence spectrum, dashed line (----) represents the calibrated autofluorescence spectrum which is the ratio of the original spectrum to the diffuse reflectance spectrum in (a).

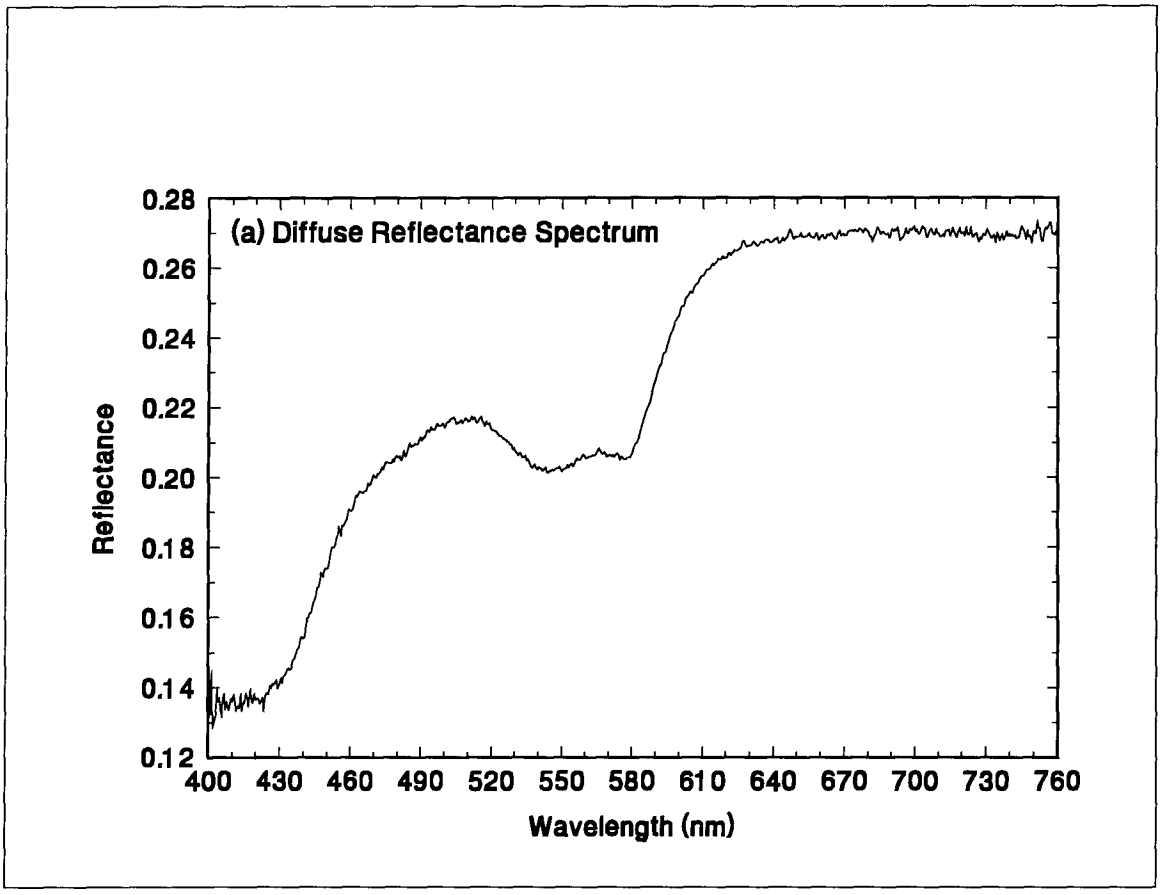

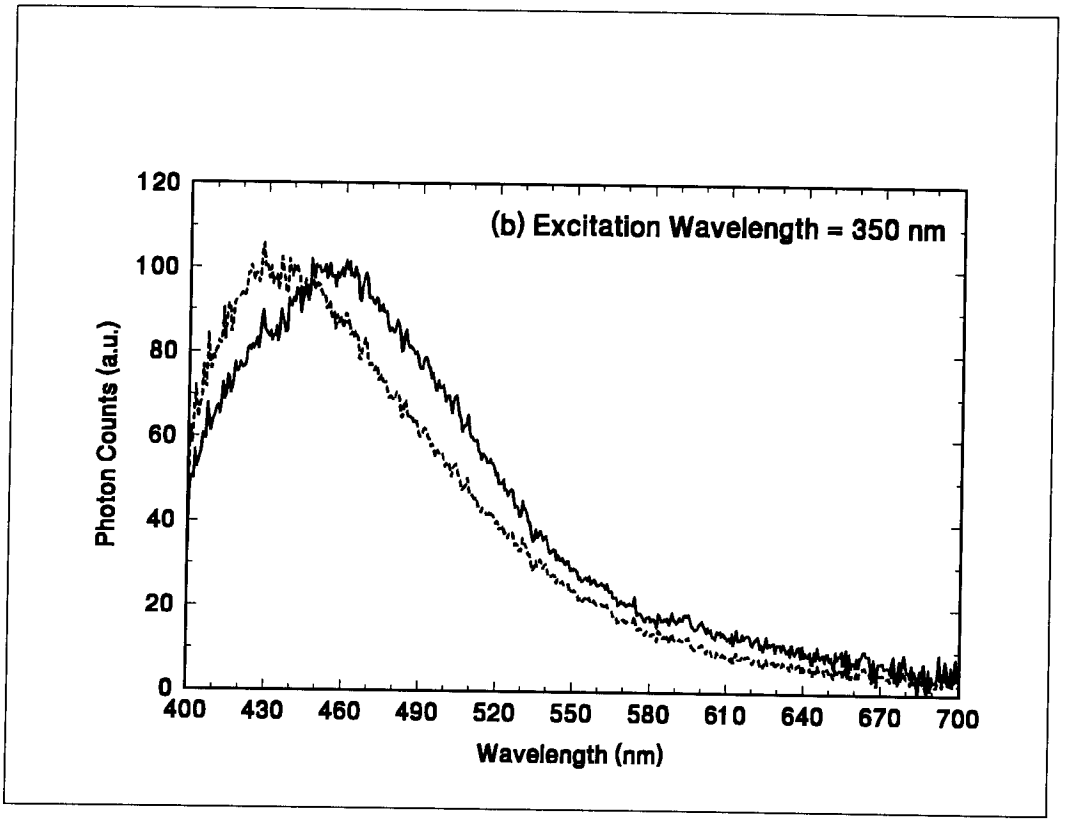
(b) Excitation Wavelength = 350 nm
Photon Counts (a.u.)
120
100
80
60
40
20
0
400 430 460 490 520 550 580 610 640 670 700
Wavelength (nm)

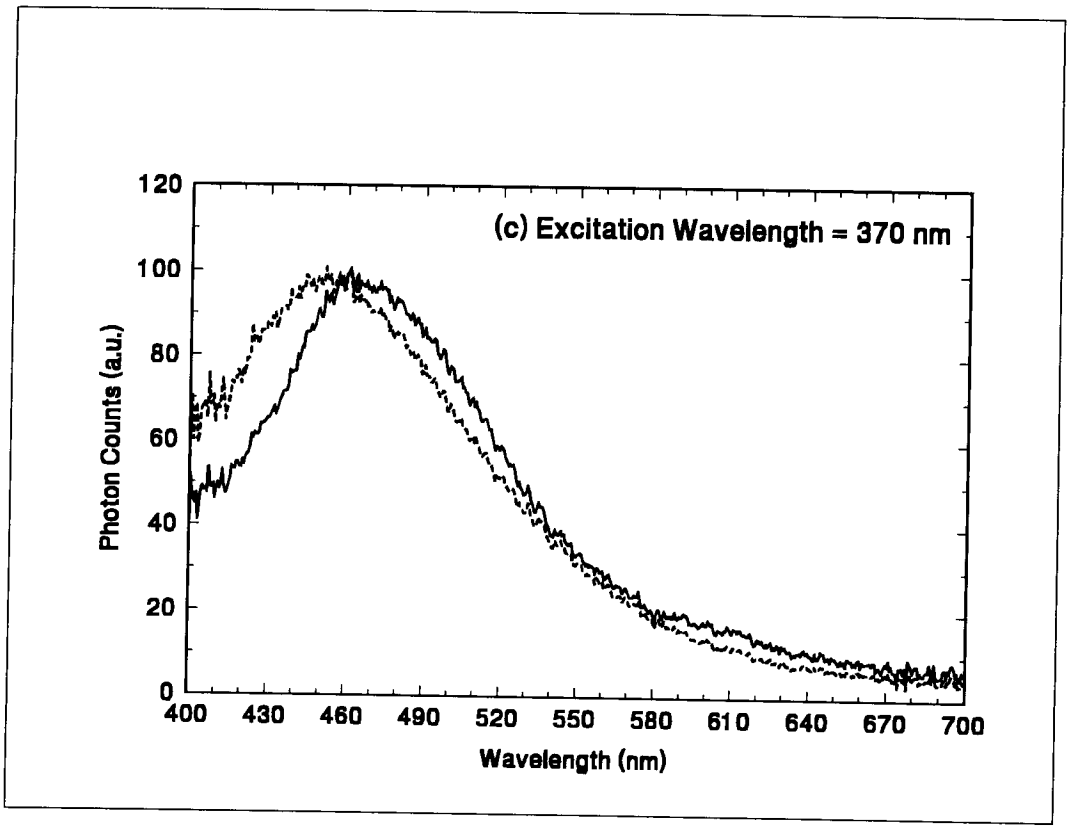
(c) Excitation Wavelength = 370 nm
Photon Counts (a.u.)
120
100
80
60
40
20
0
400 430 460 490 520 550 580 610 640 670 700
Wavelength (nm)

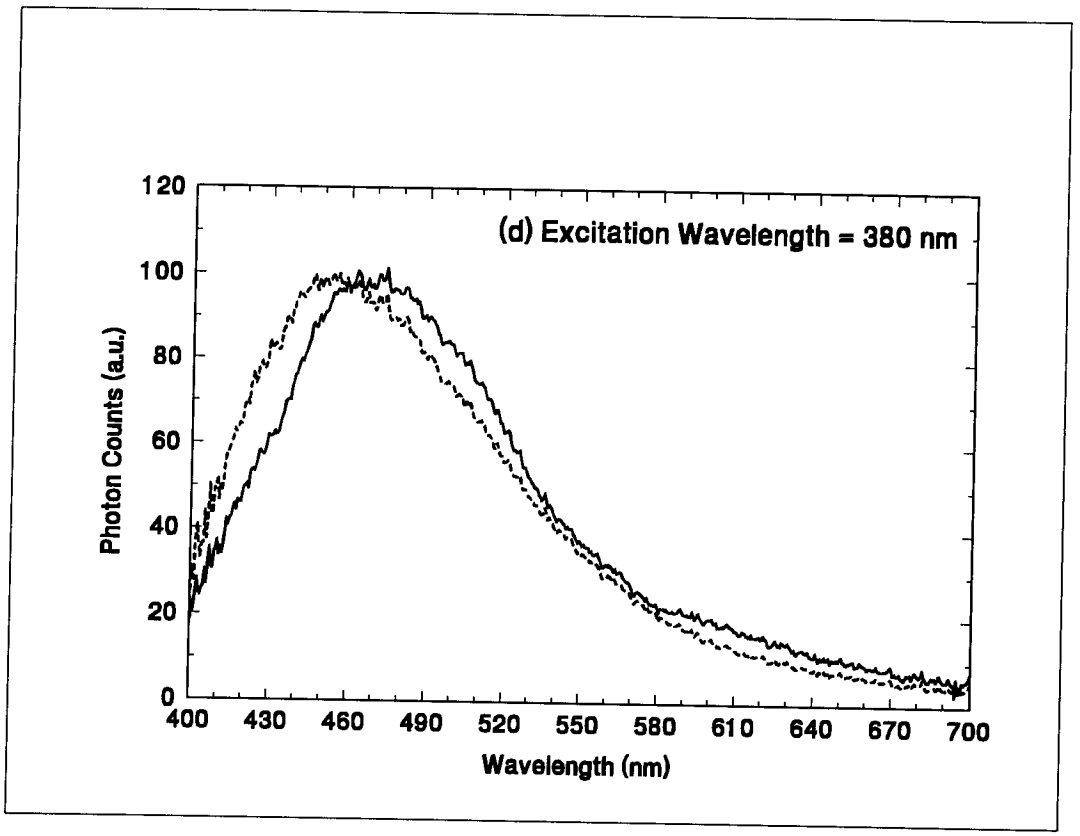
(d) Excitation Wavelength = 380 nm
Photon Counts (a.u.)
120
100
80
60
40
20
0
400
430
460
490
520
550
580
610
640
670
700
Wavelength (nm)

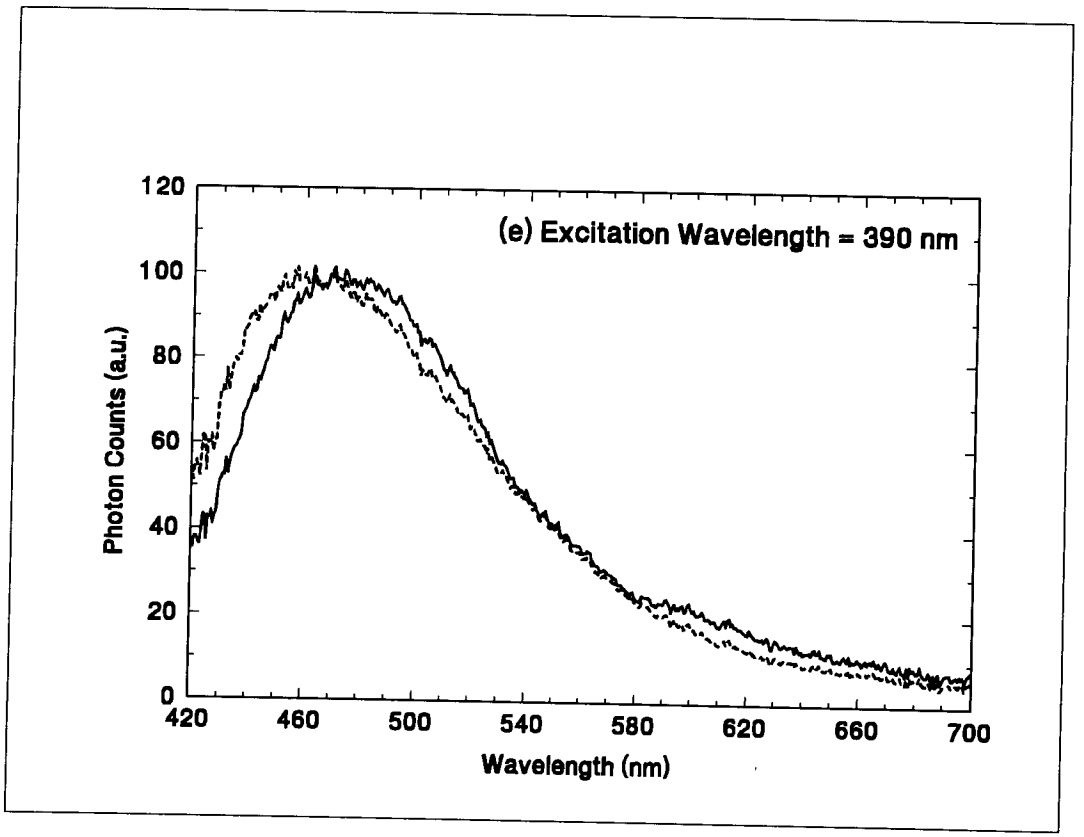
(e) Excitation Wavelength = 390 nm
Photon Counts (a.u.)
120
100
80
60
40
20
0
420
460
500
540
580
620
660
700
Wavelength (nm)

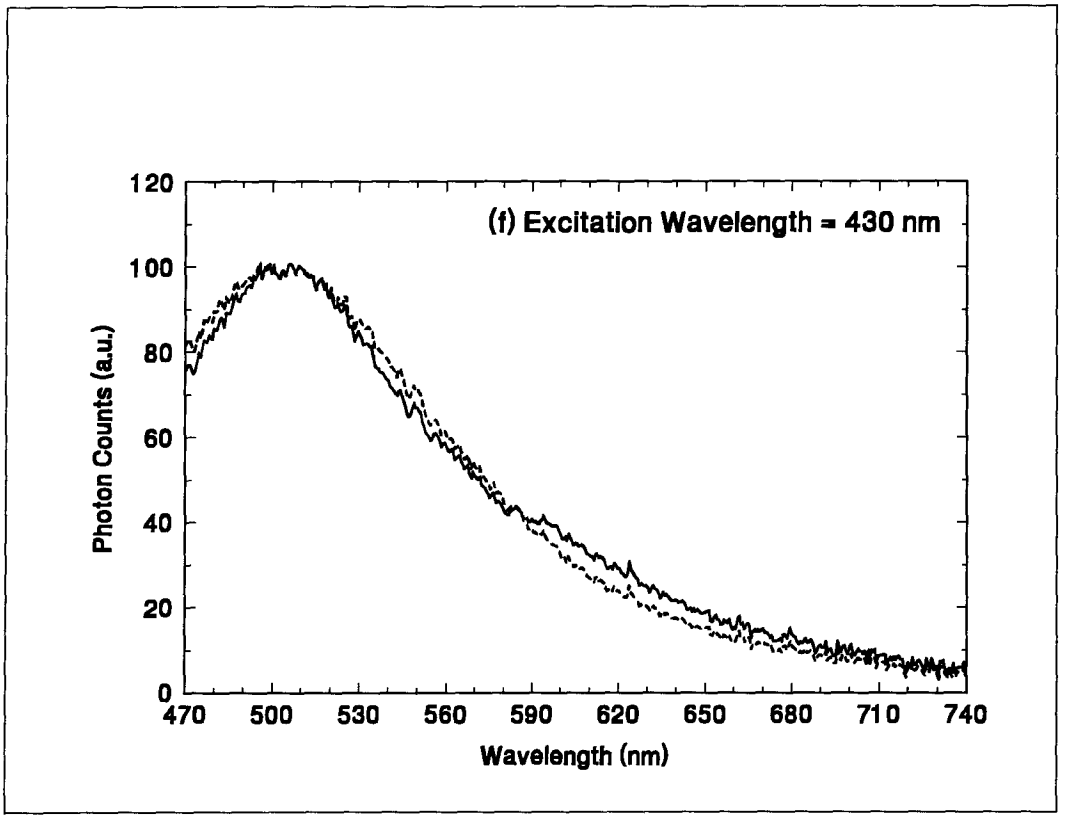
(f) Excitation Wavelength = 430 nm
Photon Counts (a.u.)
120
100
80
60
40
20
0
470
500
530
560
590
620
650
680
710
740
Wavelength (nm)

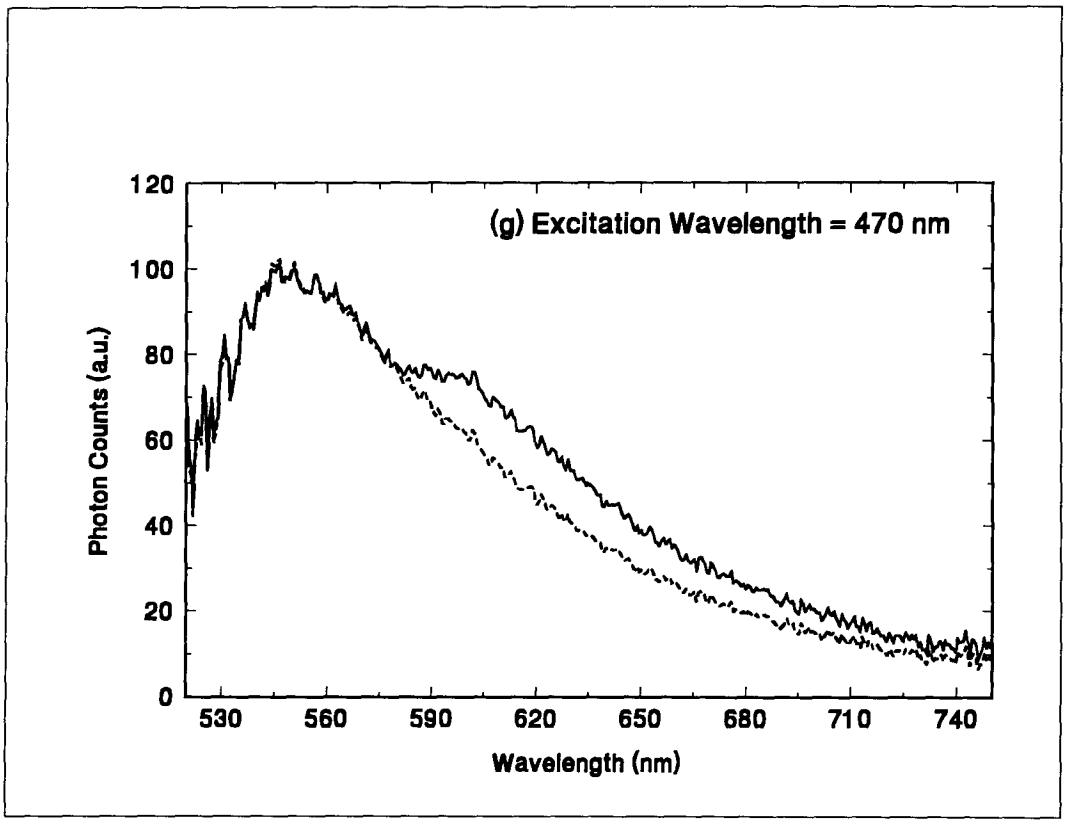
(g) Excitation Wavelength = 470 nm
Photon Counts (a.u.)
120
100
80
60
40
20
0
530
560
590
620
650
680
710
740
Wavelength (nm)

different excitation wavelengths are very different in both shape and intensity. The spectrum maximum positions shift with changing excitation wavelengths. Figure 18 shows the diffuse reflectance spectrum (a) and autofluorescence spectra at 6 different excitation wavelengths (b, 350 nm, c, 370 nm, d, 380 nm, e, 390 nm, f, 430 nm, g, 470 nm) of an Asian volunteer's hand dorsum. The solid lines denote the measured original spectra.

As mentioned in Chapter 1, tissue reabsorption and scattering distort the shape of fluorescence spectra. This motivated us to build a combined autofluorescence and diffuse reflectance spectroanalyser system in order to assess the distortion of the fluorescence spectrum by using the diffuse reflectance spectrum.

Fluorescence emission inside the tissue is isotropic, half of the emission is upward, the other half is downward (figure 19). If there is no scattering, only the upward emitted light can escape out of the tissue (assuming refraction index matched boundary). If there is scattering, the upward emitted light will be more difficult to escape out of the tissue: the larger the effective scattering coefficient $\mu_s(1-g)$, the less light of the upward emission will come out. In contrast, the light from the downward emission will have the possibility to escape out of the tissue after multiple scattering: the larger the $\mu_s(1-g)$, the more of the downward emission light will come out. However, in any case, the larger the absorption coefficient μ_a, the less the fluorescence light can escape out of the

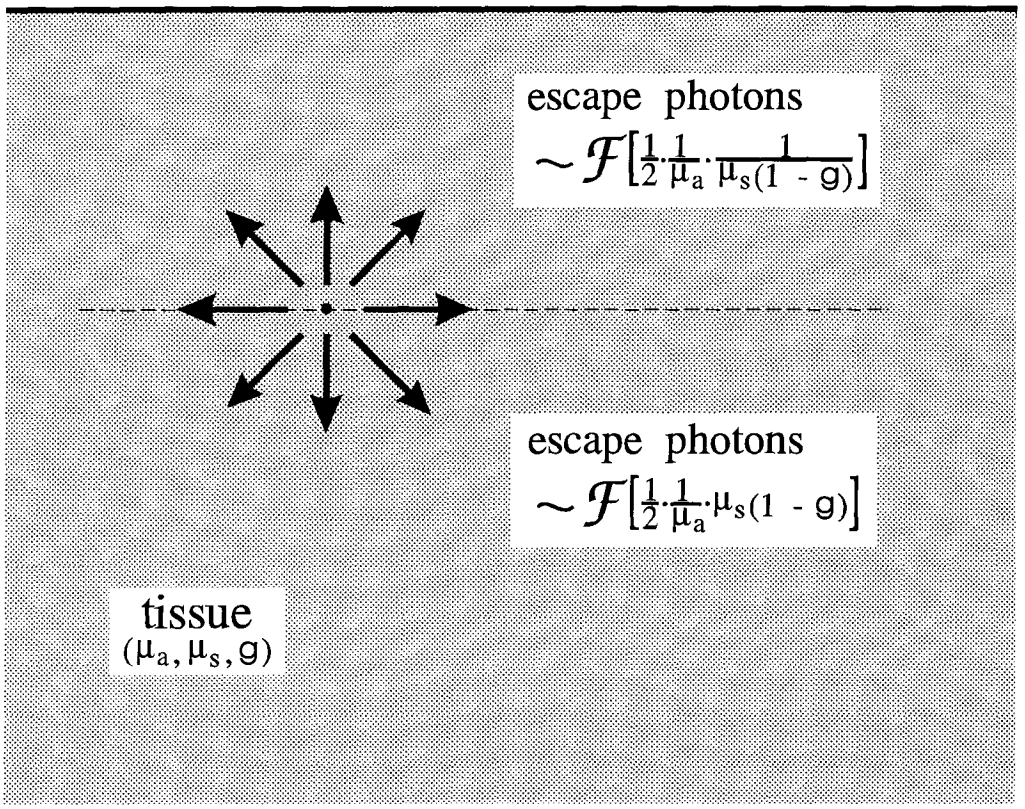

$\mathcal{F}$ is a monotonically increasing function.

Figure 19. Apparent relationship between the fluorescence distortion factor and the tissue absorption, scattering properties.

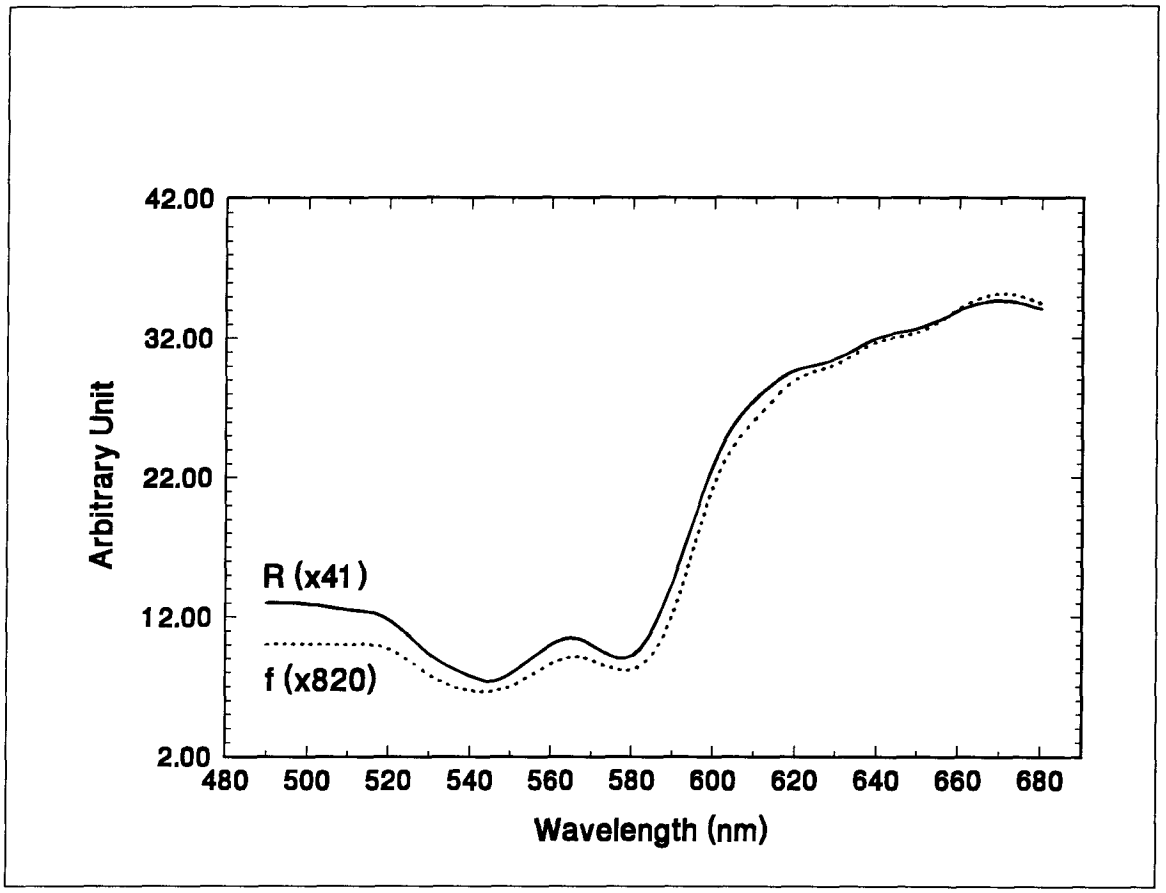

Figure 20 Comparison of the diffuse reflectance R with the fluorescence distortion factor *f* calculated by Monte Carlo simulation for a semi-infinite uniform tissue phantom. This was generated by re-analyzing data from Gardner *et al*, 1993.

tissue. The fluorescence distortion factor or escape effectiveness f can be written as:

$$f = \mathcal{J}\left\{\frac{1}{\mu_a} \bullet \frac{1}{2}\left[\frac{1}{\mu_s(1-g)} + \mu_s(1-g)\right]\right\} \qquad (21)$$

where $\mathcal{J}$ is a monotonically increasing function. While the diffuse reflectance R can be written as (see Chapter 1):

$$R = \mathcal{J}\left\{\frac{1}{\mu_a} \bullet \mu_s(1-g)\right\} \qquad (22)$$

In the skin tissue, $\mu_s(1\text{-}g)$ is a slowly varying smooth curve in the visible wavelength range (see Eq.(6) and figure 4) compared to the sharply varying absorption spectra of skin chromophores (see figure 3). The peaks, valleys, and the overall sharp increase in the reflectance curve of figure 18a must be largely due to the melanin and haemoglobin absorption. We proposed to use R as a first order approximation of f to calibrate the fluorescence spectrum. The dashed lines in figure 18b - g are the calibrated fluorescence spectra which equal the measured spectra divided by R. In all cases, the calibrated spectra have greater symmetry and are smoother compared to the measured original spectra. Also, the valleys due to the oxyhaemoglobin absorption are largely eliminated by this calibration.

Very recently, Gardner *et al* (1993) modeled the fluorescence excitation and escape processes of a semi-infinite uniform tissue phantom by Monte Carlo simulation. The fluorescence distortion factor f was calculated exactly in terms of measured diffuse reflectance R and optical properties

Table 1. The wavelengths of skin autofluorescence spectral maxima at different excitation wavelengths. The excitation wavelengths were selected by a monochromator and 10 nm band pass filters.

Excitation Wavelength (nm)	Emission Maxima Wavelength (nm) (Non-calibrated Spectra)	Emission Maxima Wavelength (nm) (Calibrated Spectra)
350 ± 5	455 ± 3	433 ± 3
360	460	440
370	465	452
380	470	454
390	475	463
410	490	484
430	504	503
450	515	516
470	548	547

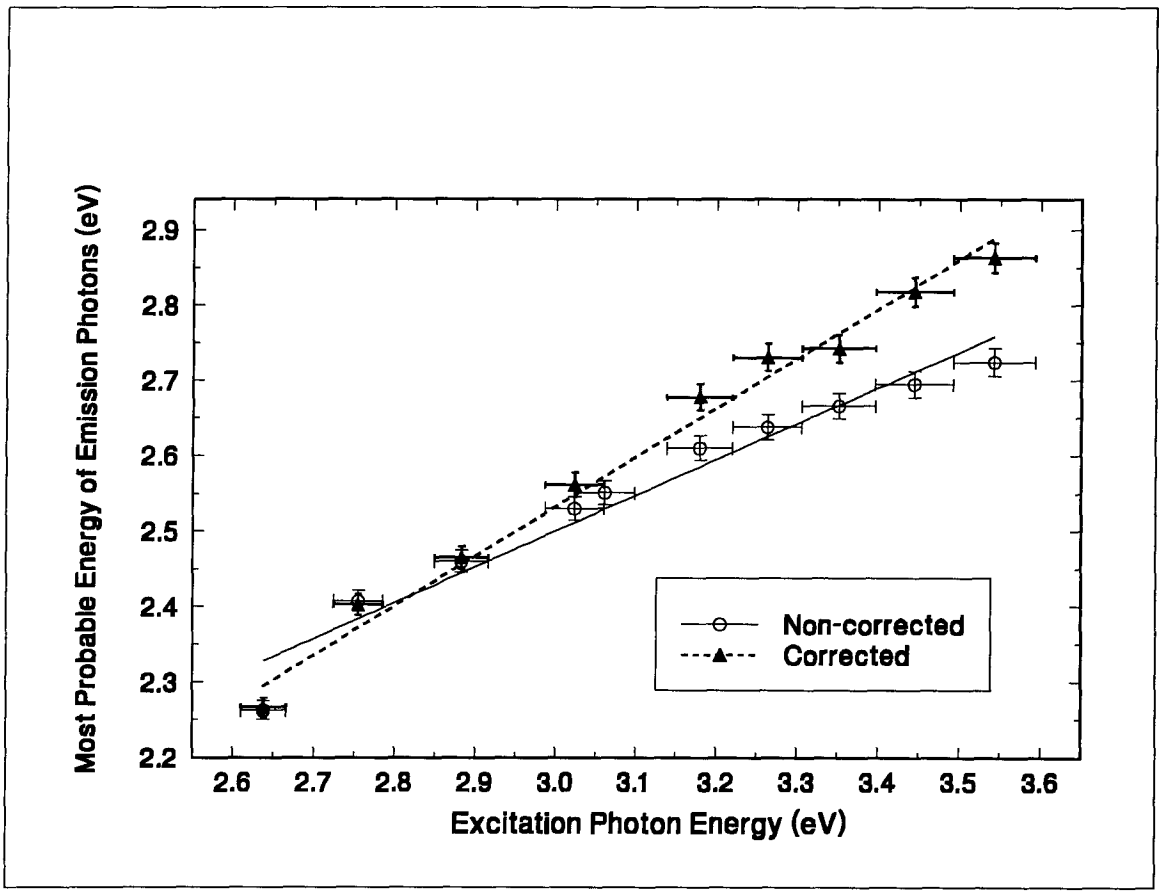

Figure 21. Most probable energy of fluorescence emission photons versus excitation photon energy. The non-calibrated data were obtained from the measured original autofluorescence spectra, while the calibrated data were obtained from the calibrated autofluorescence spectra. The solid line is described by equation, $y = (0.47 \pm 0.04)\ x + (1.1 \pm 0.1)$ with a R coefficient of 0.957. The dashed line is described by equation, $y = (0.66 \pm 0.03)\ x + (0.56 \pm 0.08)$ with a R coefficient of 0.988.

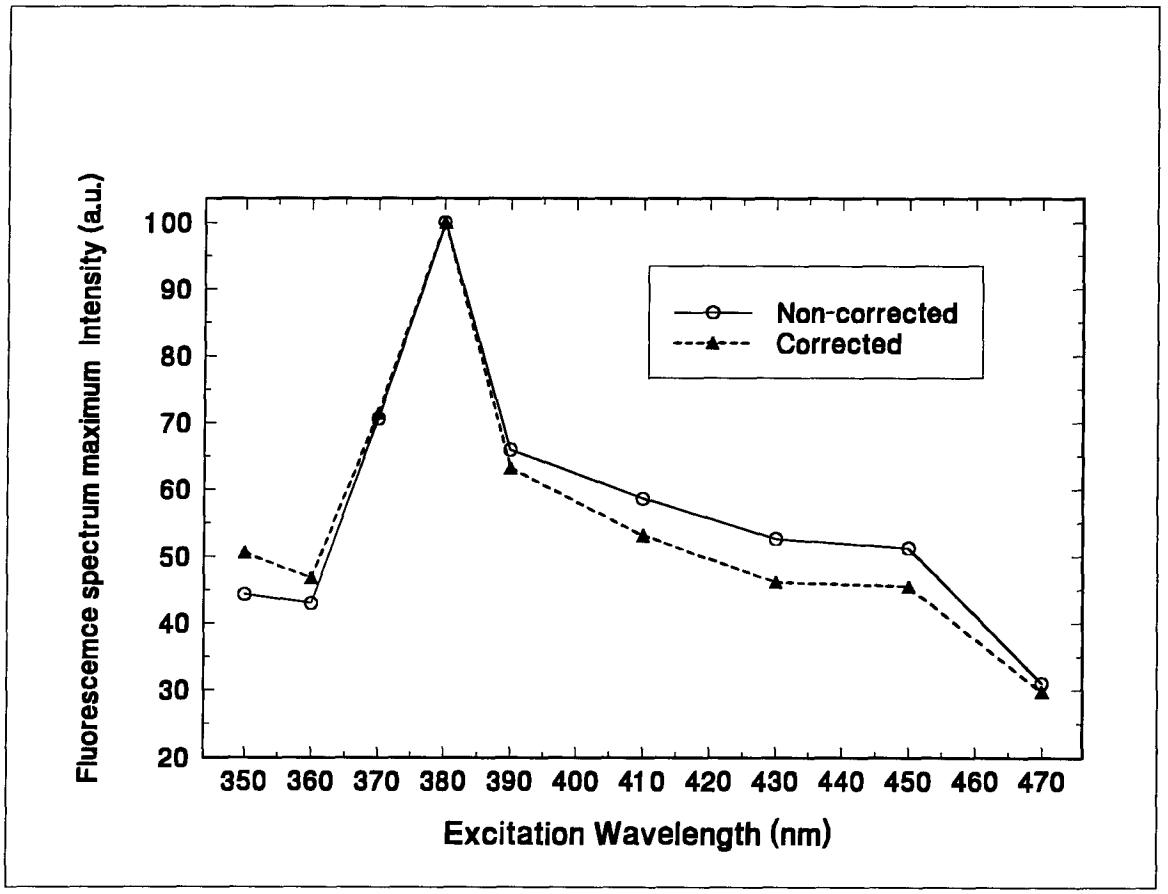

Figure 22. Excitation spectrum of skin autofluorescence emission: plot of the fluorescence spectrum maximum intensity versus the excitation wavelength. The non-calibrated data were obtained from the measured original autofluorescence spectra, while the calibrated data were obtained from the calibrated autofluorescence spectra. The most efficient excitation wavelength is 380 nm.

(μ_a, μ_s, g). We re-scaled the diffuse reflectance R and the fluorescence distortion factor f and plotted them onto the same graph (figure 20) for comparison. One can see that the two curves have very similar shapes and the difference between the re-scaled R and f is much smaller than the absolute values of the re-scaled R and f. Therefore, we believe that R represents a very good first order approximation of f for tissue fluorescence spectrum calibration.

From figure 18, one can see that at different excitation wavelengths, the maximum positions of skin autofluorescence spectra are different. Table 1 gives the wavelengths of skin autofluorescence spectral maxima at different excitation wavelengths for the data set shown in figure 18. We then converted the wavelength into energy of photons in units of electron volts (ev). The energy corresponding to the wavelength at the spectral maximum is the most probable energy of fluorescence emission photons. Figure 21 is the most probable energy of fluorescence emission photons versus excitation photon energy plot. The solid line and open circle symbols denote data obtained from the measured original spectra, while the dashed line and solid triangles denote data obtained from the calibrated spectra. The most probable emission energy tends to increase linearly with increasing excitation photon energy. The calibrated data showed better linearity. The slopes of the two straight lines (0.47 for solid line and 0.66 for dashed line) are very different from 1.

Usually, for a simple fluorophore molecule, the shape of the emission spectrum is independent of the excitation wavelength (Lakowicz, 1983). The data shown in table 1 and figure 21 suggest two possibilities about the skin fluorophores. One possibility is that there is more than one type of fluorophore molecules inside the skin tissue which are responsible for the visible autofluorescence. Different fluorophores have different excitation and emission spectra. This may explain that the emission spectrum shape depends on the excitation wavelength but will be hard to explain the continuously linear increasing trend shown in figure 21. The second possibility is that there is only one predominant type of fluorophore molecules which is responsible for the visible autofluorescence emission. This fluorophore must have a complicated structure and special properties which lead to the phenomenon shown in figure 21.

Since the emission spectrum shape depends on the excitation wavelength, we plotted the fluorescence spectrum maximum intensity versus the excitation wavelength as the excitation spectrum of skin autofluorescence emission (figure 22). One can see that 380 nm is the most effective excitation wavelength. The conventional definition of fluorescence excitation spectrum is the fluorescence emission intensity at a selected wavelength as a function of the excitation wavelength. If the fluorescence emission spectrum shape is independent of the excitation wavelength, the measured excitation spectrum should be the same no matter which emission wavelength is

selected to do the measurements. However, the autofluorescence emission spectrum shape of skin is excitation wavelength dependent as mentioned above, therefore, the skin excitation spectra using conventional definition must be emission wavelength dependent. The human skin excitation spectra reported very recently by Kollias *et al* (1993) do change with the emission wavelength. Their data and our data support each other although different measurement modalities (emission spectra vs. excitation spectra) were employed in the two studies. The different ways of data analyses may lead to different insights about the skin autofluorescence properties.

To understand these phenomena, the skin fluorophores must be identified. Chemical isolation of fluorophore in biological tissue is a task requiring multi-discpline collaborations and the isolated molecules may have different fluorescence properties from those presented in the *in vivo* tissue due to the chemical environment changes (Baraga *et al*, 1991). This is out of the scope of this thesis. Our attention instead was directed towards the temporal dynamics of skin autofluorescence.

3.3 Laser induced autofluorescence decay of *in vivo* skin

To characterize laser induced autofluorescence decay of *in vivo* skin, we measured the autofluorescence decay processes during continuous He-Cd laser (442 nm) exposure on the inner forearm of 5 volunteers at different illumination power

densities. The autofluorescence recovery processes after terminating the laser exposure were also monitored.

3.3.1 Autofluorescence decay dynamics of *in vivo* skin during CW laser exposure

Non-linear regression fitting of all measured autofluorescence decay curves revealed that the autofluorescence decays followed a double exponential function:

$$I(t) = a \exp(-t/\tau_1) + b \exp(-t/\tau_2) + c \quad (23)$$

with a fast process (first term) and a slow process (second term). The time constants (τ_1, τ_2) of the two processes differed by an order of magnitude. Parameters a, b, c were normalized to satisfy the condition that I(0) = 1 at t = 0, i.e.:

$$a + b + c = 1 \quad (24)$$

Figure 23 shows an example of such data. It was obtained from the inner forearm of a volunteer of Chinese ancestry under an illumination power density of 64 mW/cm^2. I(t) represents the integral intensity over a 10 nm wavelength band at 520 nm. The upper part of the graph gives the 120 original data points, the fitted double exponential decay curve (solid line), and the equation. The parameters (a, b, c, τ_1, τ_2) and their standard deviations derived by the non-linear regression program are given in the caption. The lower part of the graph shows the residual curve at a magnified Y axis scale. The residuals fluctuate randomly around zero value with amplitudes of less

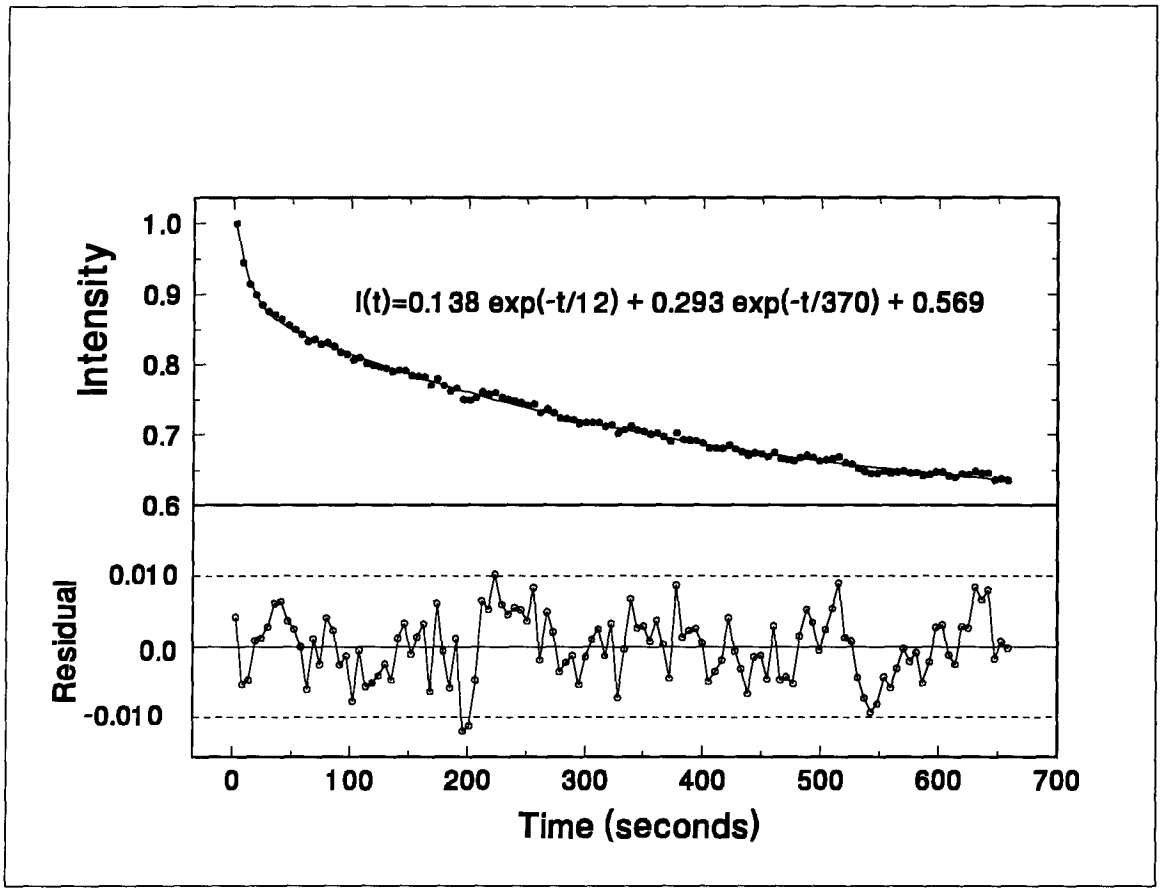

Figure 23. A sample of autofluorescence decay during continuous laser exposure (location: inner forearm, exposure power: 64 mW/cm^2). Fitted parameters: a = 0.138 ± 0.007, b = 0.293 ± 0.004, c = 0.569 ± 0.005, τ_1 = 12 ± 1, τ_2 = 370 ± 14.

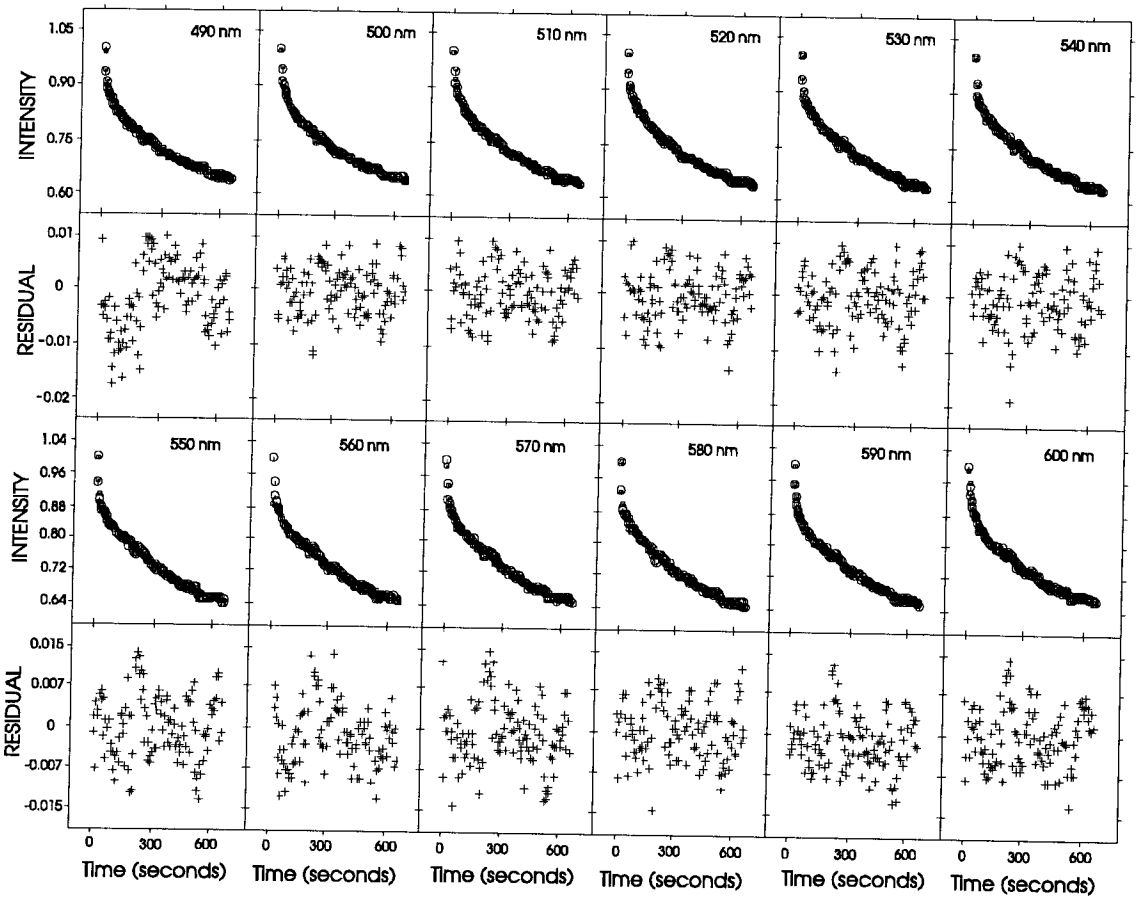

Figure 24. Autofluorescence decays of 12 different wavelength bands. The small circles denote the original data points, while the squares denote the points predicted from the fitted double exponential curves. For the 560 nm curve, the first three original data points are far away from the predicted points, their residuals are out of the maximum y axis scale (0.015). This graph is an output of the BMDP software.

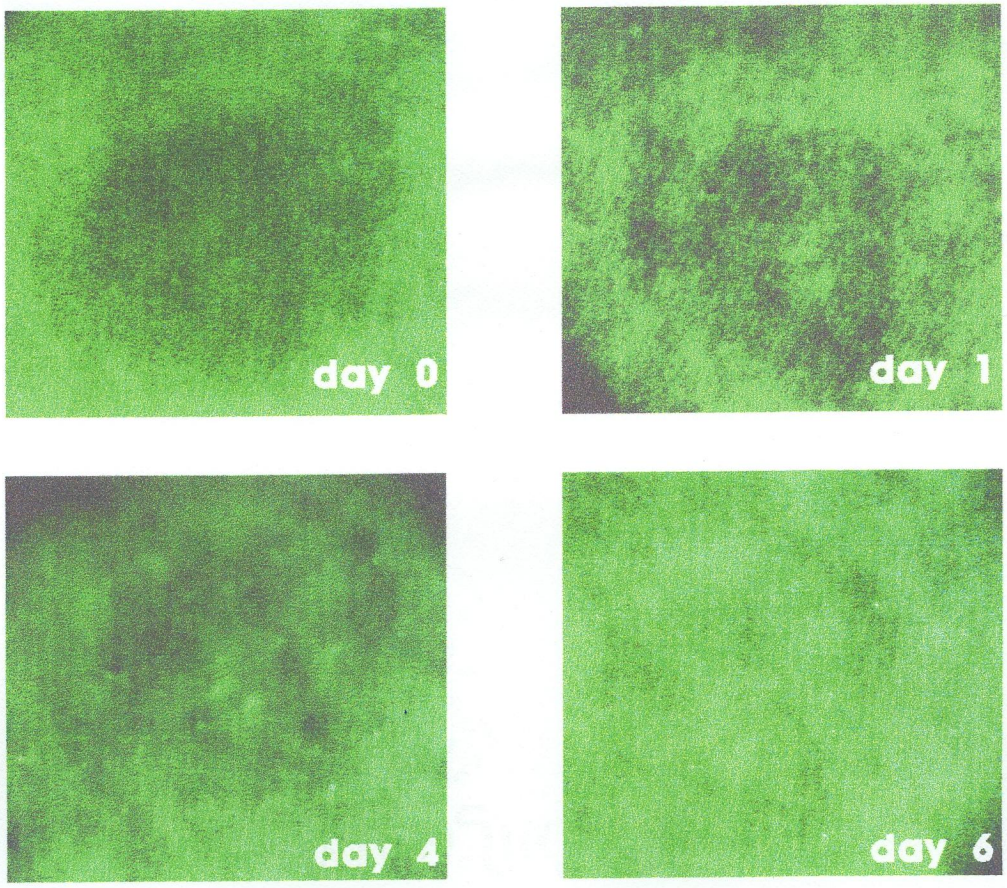

Figure 25. Autofluorescence images taken at different times (days) after the inner forearm of a volunteer continuously exposed to 442 nm laser light (power density: 28 mW/cm^2) for 11 minutes. The picture for day 0 was taken right after the termination of the laser irradiation.

than 0.012 supporting selection of the double exponential function as the best fit to the experimental data.

Figure 24 shows the fitted double exponential decay curve for 12 different wavelength bands, generated from the same spectra as described in figure 23. All curves show excellent double exponential fitting and have random residual distributions except for the 560 nm band curve. The fitted parameters (a, b, c, τ_1, τ_2) have some small differences for different wavelengths and therefore the average parameters over all bands were calculated. The standard deviation of these parameters were also calculated and used as an estimation of the experimental errors.

3.3.2 Autofluorescence recovery process after prolonged laser exposure

To assess the autofluorescence recovery process after laser exposure, we monitored the autofluorescence emission spectra at 5 minute intervals for 50 minutes immediately following the termination of the laser exposure. During this period of time, no fluorescence recovery was noted. Autofluorescence imaging revealed the exposed skin site as a dark circular spot. In contrast, white light diffuse reflectance images showed no differences between the exposed skin site and the surrounding (unexposed) sites. Figure 25 shows four images of a series of autofluorescence images taken after the termination of the continuous laser exposure. With

time, the dark spot in the images became brighter until it reached the same intensity as the surrounding unexposed skin. Figure 25 shows that after continuous skin exposure to 442 nm, 28 mW/cm^2 laser light for 11 minutes, complete recovery of the autofluorescence took about 6 days. The random pattern of recovery images (figure 25, day 1 and day 4) suggests that the autofluorescence recovery is not due to the diffusion of the fluorophores from the unexposed area to the exposed area.

3.3.3 Autofluorescence decay parameters change with exposure intensity

To study the possible differences of skin autofluorescence decay processes under different exposure intensity, we measured the autofluorescence decays of four very close skin sites on the inner forearm of the same volunteer under four different exposure intensities (64 mW/cm^2, 42 mW/cm^2, 27 mW/cm^2, 3.8 mW/cm^2 respectively).

Figure 26 shows the autofluorescence decay curves at the wavelength band of 520 nm for the four different exposure intensities. Similar curves exist for other wavelength bands. Table 2 gives the respective average decay parameters under these exposure intensities. For the very low exposure intensity (3.8 mW/cm^2), the fitted curve is a very slow single exponential decay, while all other three curves are double exponential functions. The errors shown in table 2 are the standard deviations calculated from the parameters for the 12

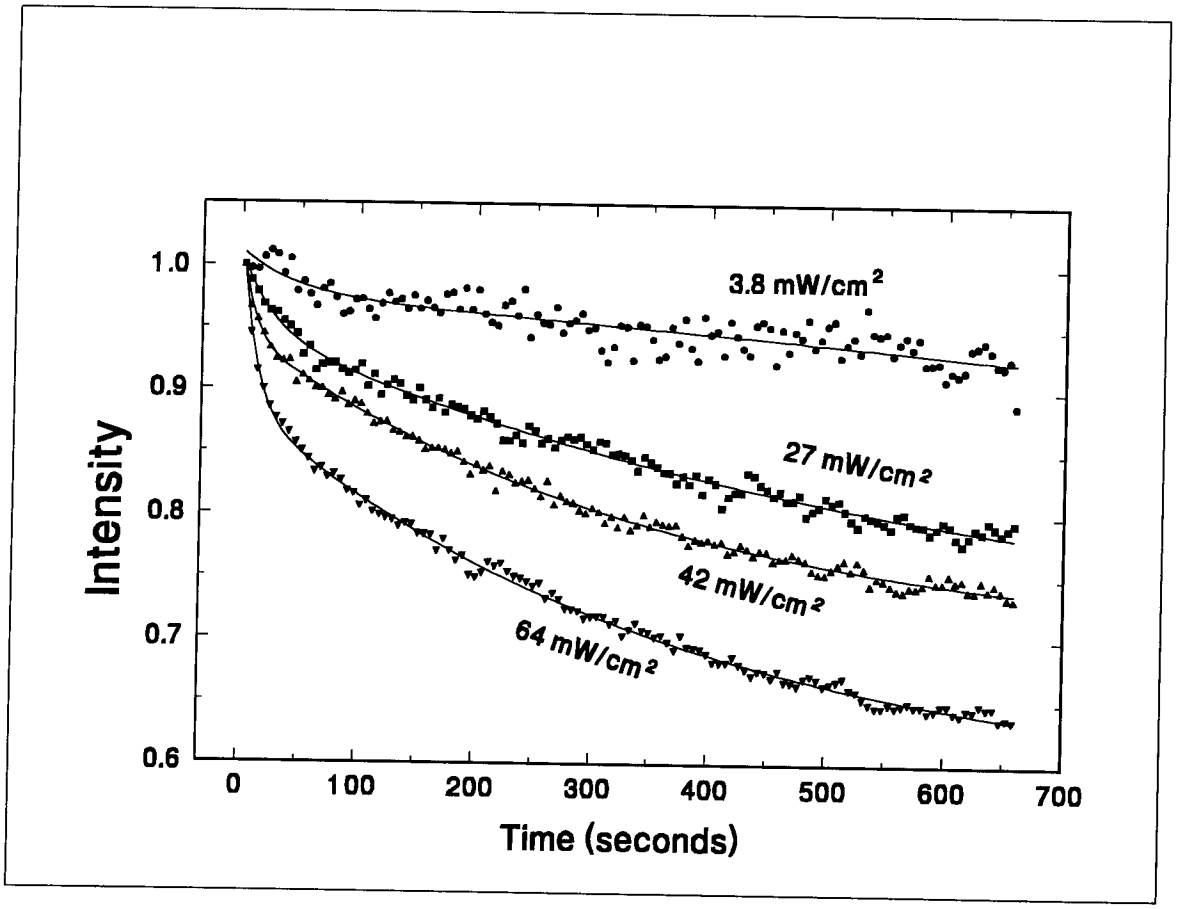

Figure 26. Differences of the autofluorescence intensity decay induced with different exposure intensities.

Table 2. Skin autofluorescence intensity decay parameters (*a*, *b*, *c*, τ_1, τ_2) induced with different exposure intensities

exposure intensity / parameters	64 mw/cm^2	42 mw/cm^2	27 mw/cm^2	3.8 mw/cm^2
a	0.14 ± 0.01	0.081 ± 0.008	0.0521 ± 0.0008	0.054 ± 0.003
b	0.29 ± 0.01	0.234 ± 0.007	0.26 ± 0.02	
c	0.56 ± 0.04	0.685 ± 0.009	0.69 ± 0.02	0.95 ± 0.01
τ_1(sec.)	10 ± 3	8 ± 2	25 ± 3	196 ± 5
τ_2(sec.)	400 ± 48	385 ± 15	625 ± 78	

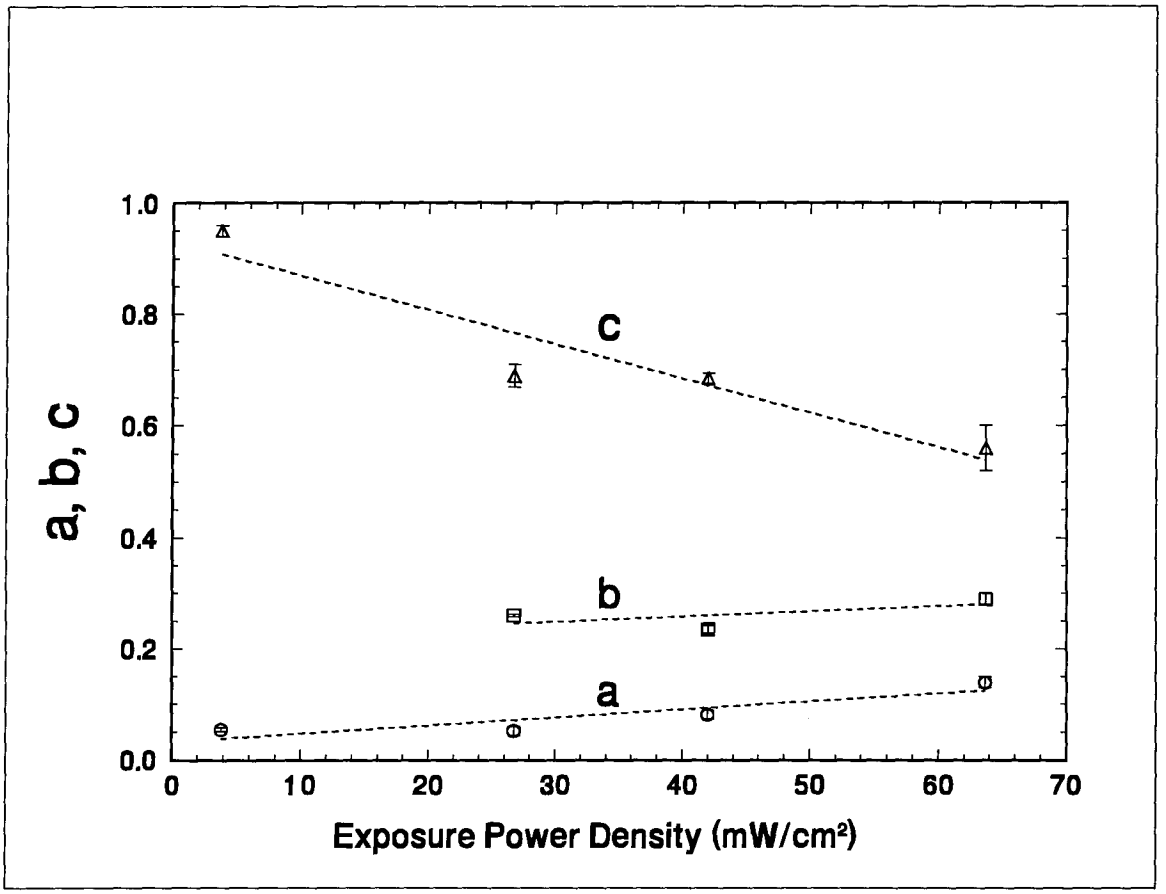

Figure 27. Skin autofluorescence intensity decay parameters *a*, *b*, *c* change with exposure intensity

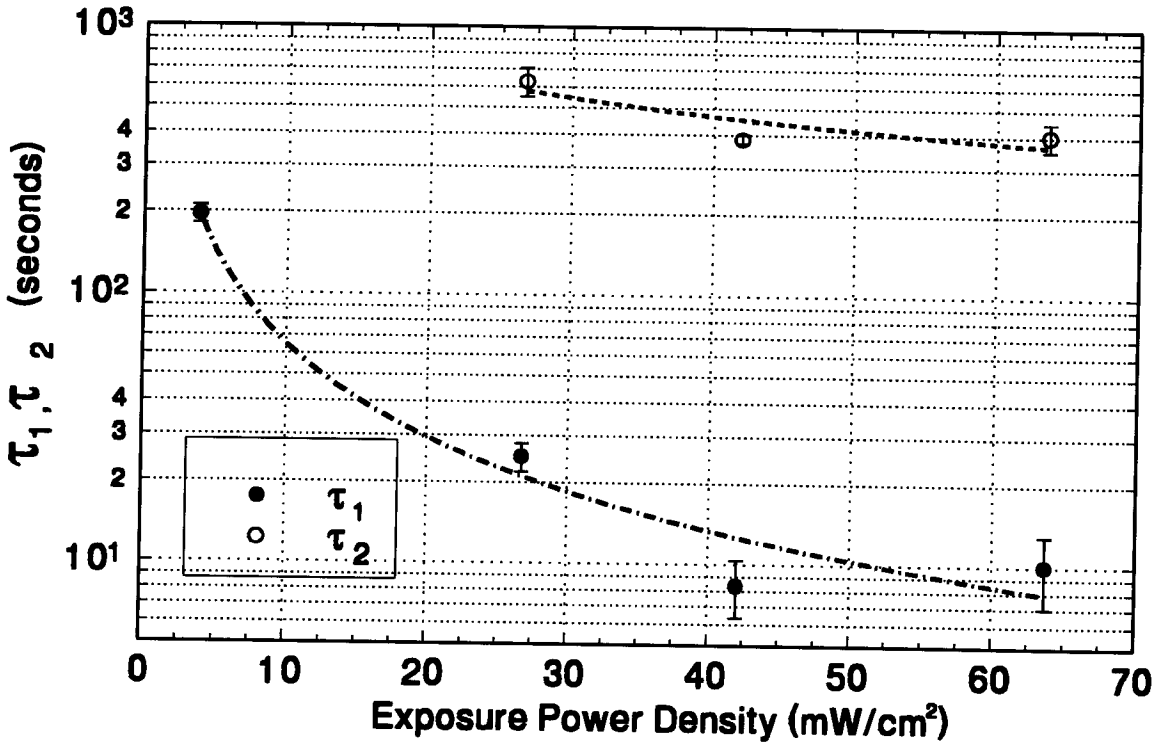

Figure 28. Skin autofluorescence intensity decay parameters τ_1 and τ_2 change with exposure intensity

wavelength bands, not including possible errors caused by the differences of the four measured skin locations. Figure 27 and 28 show how these parameters change with time graphically: *a* and *b* have the tendency to increase when the exposure intensity increases, while *c* has the tendency to decrease with increasing exposure intensity; τ_1 and τ_2 decrease when the exposure intensity increases. At the very low exposure intensity (3.8 mW/cm^2), τ_2 can not be measured with an 11 minute exposure experiment.

CHAPTER 4: UNDERSTANDING THE DYNAMICS OF SKIN AUTOFLUORESCENCE DECAY

4.1 Hypothesis on the mechanism of skin autofluorescence decay dynamics

It may seem plausible that the double exponential decay is simply due to two different types of fluorophores. However, the decay parameters change with exposure intensity. As the skin is a multi-layered inhomogeneous turbid medium, excitation laser light distribution inside the skin tissue will not be uniform. Due to the scattering and absorption, the fluorescence emission from different depths of the skin will have different escape efficiencies and therefore, different fractional contributions to the detected total autofluorescence signal.

We postulated that the decay dynamics is determined by (1) the excitation laser light distribution pattern in skin tissue, (2) the number of fluorophore types and their chemical environment(s), (3) the escape efficiency of fluorescence light from different depths inside the tissue; and that (4) the measured decay dynamics may be used to determine various information about the skin, especially, to determine the fractional contributions of different skin layers to the total *in vivo* autofluorescence signal.

The remainder of this thesis is a description how we tested and elaborated on the details of this hypothesis. Items

(1) and (3) were examined by Monte Carlo simulation of excitation laser light distribution in the skin and excited autofluorescence escape from the skin tissue based on a seven layer skin optical model. Because currently the exact skin fluorophores have not been identified, we measured the autofluorescence distributions in unstained skin tissue sections and their spectral differences using the previously described MSP system (section 2.2) in order to examine item (2). Item (4) was tested by comparing the calculated autofluorescence fractional contributions using Eq.(20) with the decay parameters, *a*, *b*, *c*.

4.2 Microscopic morphology and spectroscopy of *in vitro* skin tissue sections

Skin tissue samples were cut into sections of about 10 μm thick (kept unstained and unfixed), and then placed on glass slides for examination. The examination was performed by the MSP system described in chapter 2. White light images and fluorescence images were recorded by the CCD camera. For spectroscopic measurements, a 10x objective and a 1 mm core diameter collection fiber were used. The resulting sampling spot diameter on the slide was thus 40 μm (= 1000 μm/(10x2.5)) which was again consistent with measurements through the eyepiece reticules.

To measure the transmittance of the tissue sections, white light illumination was used. First, a reference spectrum was

recorded on a tissue free location on the slide, and then a spectrum at the selected tissue location was recorded. Division of the two spectra gave the transmittance spectrum.

For autofluorescence measurements, a 442 nm He-Cd laser beam was used to illuminate the skin sample. Before acquisition of the tissue fluorescence spectra, background fluorescence subtraction and intensity calibration had to be performed first. To acquire the background autofluorescence spectrum of the system, the detection fiber was aligned with a tissue-free location on the slide. In this way, the background fluorescence emission from all components of the microscope, including the glass slide, was acquired, and subsequently subtracted from the tissue autofluorescence signal. Intensity calibration of the fluorescence spectra was performed using an EG&G Gamma Scientific RS-10 standard lamp and the supplied data. Light from the RS-10 lamp was conducted through a fiber (which was measured to have a constant transmittance in the 400 nm to 800 nm spectral range) into the microscope illumination port to illuminate the sample slide. The calibration spectrum was collected from a tissue-free location on the slide and then used in combination with the supplied RS-10 spectral data to complete the intensity calibration by the OMA software. This procedure calibrated the wavelength dependence of the microscope and the OMA.

Thirty sections from three human skin samples were examined and all showed similar results. Figure 29 shows typical autofluorescence images of the skin tissue section.

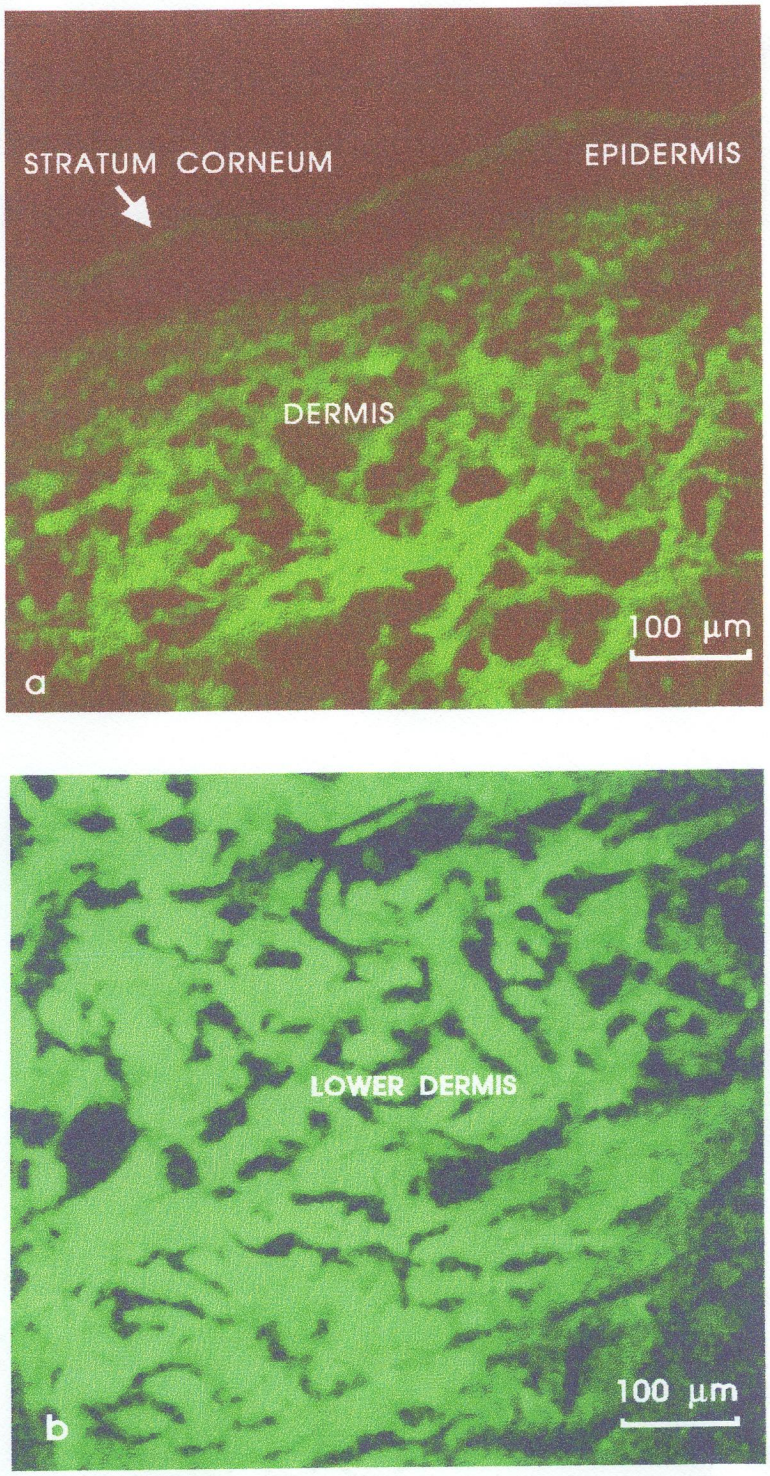

Figure 29. Typical autofluorescence images of the excised human skin tissue section; a) shows the upper part of the section, while b) shows the lower dermis part.

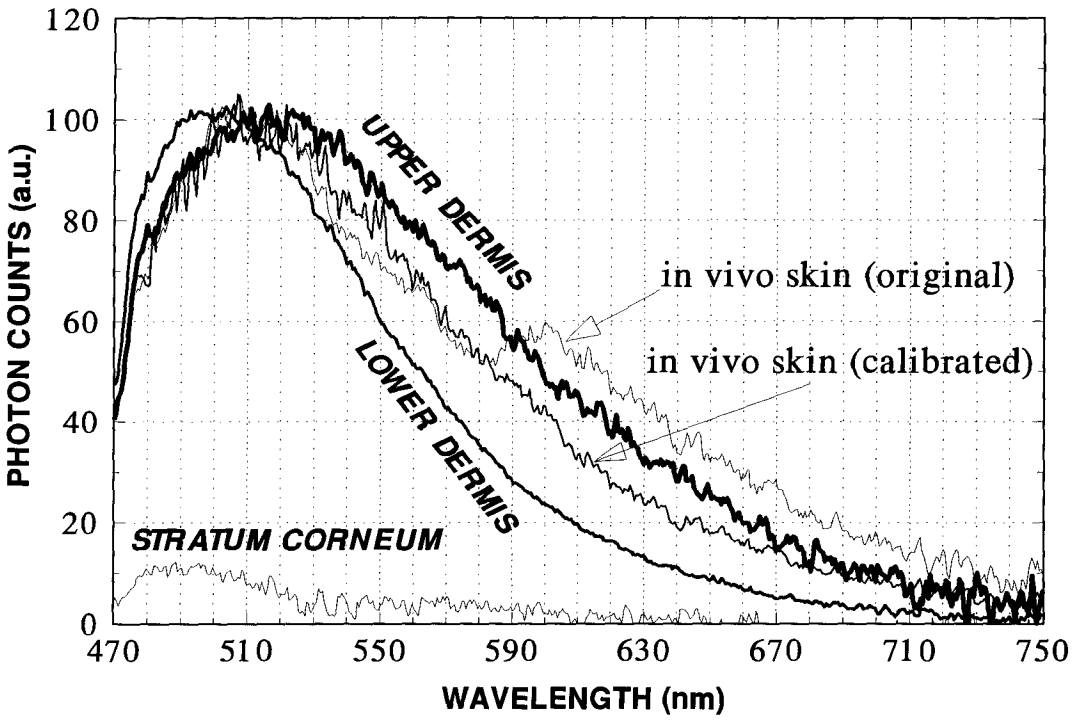

Figure 30. Typical autofluorescence spectra measured by the MSP from different locations of a sliced skin tissue section. For comparison, the *in vivo* skin autofluorescence spectra under the same 442 nm laser light excitation are also shown.

The dominant autofluorescence color is green. The dermis and the subcutaneous fat have strong autofluorescence emission, the stratum corneum autofluoresces with a weak signal, while the epidermis yields even less autofluorescence. The color of the autofluorescence from the upper dermis and the lower dermis is quite different. The upper dermis autofluorescence is more yellow and the lower dermis is more green. Figure 30 shows typical autofluorescence spectra of different skin layers measured from the tissue sections by the MSP. The spectrum of the lower dermis shifts toward the short wavelength end. The positions of the spectrum maxima of the upper and lower dermis differ by 20 nm. This difference may be related to the different chemical compositions of the papillary dermis and the reticular dermis. For example, the papillary dermis contains predominantly type III collagen and lesser amounts of type I, while the reticular dermis contains mostly type I collagen and lesser amounts of type III (Montagna *et al*, 1992).

For comparison, in figure 30, the *in vivo* skin autofluorescence spectra are also shown which were excited by the 442 nm laser light. The calibrated (using diffuse reflectance) *in vivo* spectrum is quite close to the spectrum of the upper dermis. The fact that the two spectra are not exactly coincident could be due to the calibration of the *in vivo* spectrum by only a first order approximation and/or due to the fact that the *in vivo* spectrum contains contributions from both the upper dermis and the stratum corneum. In the next section, we show a proof that the lower dermis has a negligible

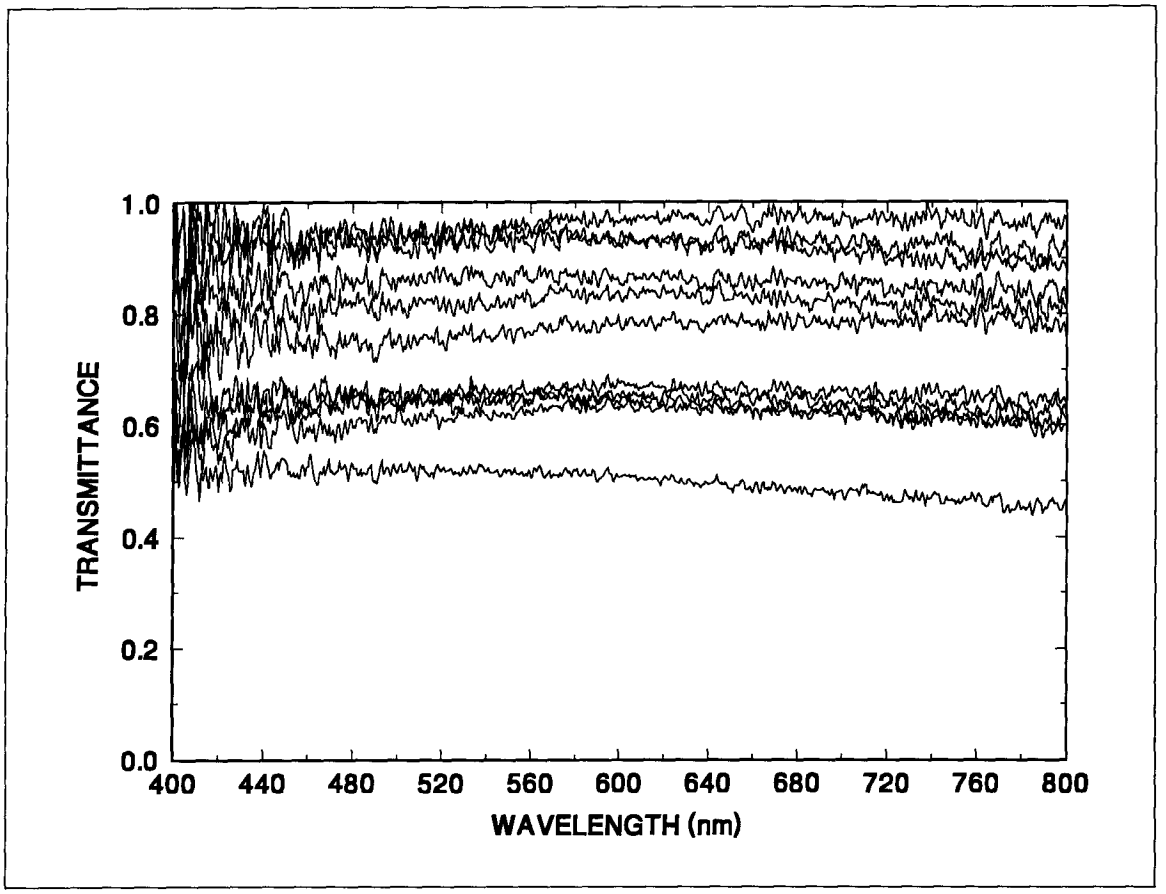

Figure 31. Transmittance spectra measured by the MSP from different locations of a sliced skin tissue section.

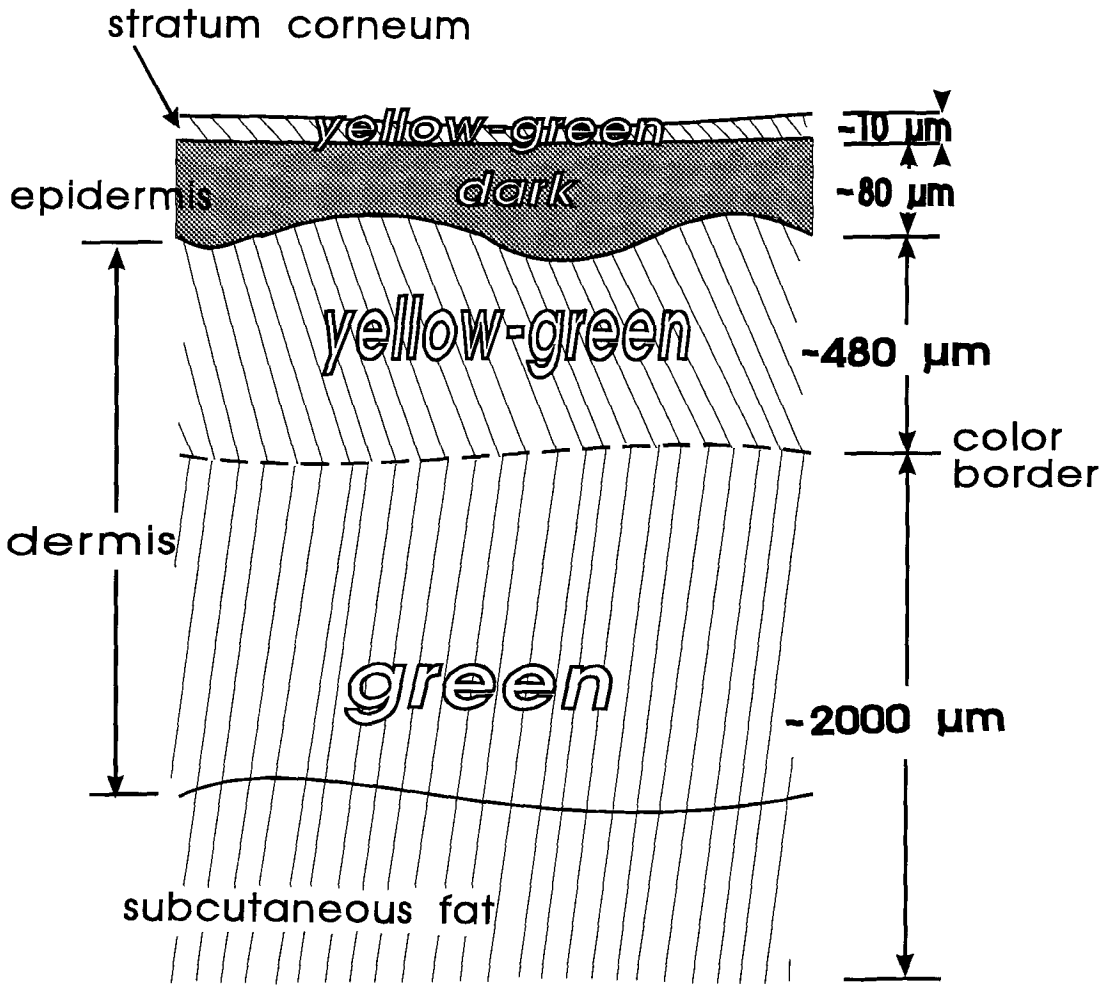

Figure 32. Schematic diagram of a typical autofluorescence distribution in skin tissue.

contribution to the measured total *in vivo* autofluorescence signal under 442 nm blue light excitation.

Figure 31 shows several transmittance spectra measured at different spots across the sample. These spectra were all essentially flat lines indicating very little absorption structures. These were consistent with the bright field images of those samples in which no color was observed. On the other hand, this also indicates that the measured fluorescence spectra in figure 30 were not unduly distorted by absorption. It seems that the concentration of skin chromophores (e.g. melanin) is not high enough to be easily measured by the transmittance spectra of such thin samples. However, the more sensitive fluorescence techniques show the existence of some native fluorophore molecules and their spatial distribution inside the skin tissue (figures 29 and 30). Principally, an increase in signal over a zero background signal is measured in fluorescence methods, while in transmittance or reflectance methods, the analogous quantity, absorbed or scattered light, is measured indirectly as the difference between the incident and the transmitted or reflected light. This small decrease in the intensity of a very large signal is measured in transmittance and reflectance techniques leading to a correspondingly large loss in sensitivity (Guilbaut, 1973).

In summary, figure 32 shows a schematic diagram of a typical autofluorescence distribution in skin tissue (the dimensions shown were measured through the eyepiece reticules). The border of the two different autofluorescence color areas is

located approximately 480 μm below the dermal-epidermal junction. All of the autofluorescence spectroscopic properties, morphological structures, and the dimensions shown in figure 32 were used to construct a skin optical model as described in the next section.

4.3 Monte Carlo simulation of excitation laser light distribution in and autofluorescence escape from skin tissue

4.3.1 The skin optical model

The structure of skin is complicated. For theoretical modeling, a considerably simplified skin optical model must be developed first. According to the anatomy structure of skin and the available intrinsic optical parameters of skin, a seven layer skin optical model was constructed for Monte Carlo simulation. Table 3 outlined this model by giving the thickness (d), the refraction index (n), and the transport parameters (μ_a, μ_s, g) of each layer.

The total thickness of the model skin is 2 mm. The thickness of each layer is based on the MSP measurements on skin tissue sections (see figure 32). At one end, i.e. at the top, the skin is in contact with air (refractive index of 1.0), while at the bottom, the model skin is in contact with the subcutaneous fat with a refractive index of 1.46 (Bolin *et al*, 1989). The refractive index of stratum corneum is 1.45 (Solan

and Laden, 1977). For both epidermis and bloodless dermis, the refractive index was assumed to be 1.4 based on a 70-80% water content (Wilson and Jacques, 1990). The refractive index of total blood was assumed to be 1.33, i.e. the same as that of water. The optical parameters at two wavelengths are listed in table 3. The 442 nm is the excitation laser light, while the 520 nm represents the emitted autofluorescence light. The transport parameters for the stratum corneum, epidermis, and bloodless dermis were obtained from figure 4 and Eq.(6) in chapter 1. At 520 nm, the data for stratum corneum are not available, and we assumed that its optical parameters were the same as those of the epidermis. This should have caused little error because the stratum corneum is very thin compare to the epidermis. The upper blood plexus was assumed to consist of 10% blood and 90% dermis tissue (Jacques, 1991b). The lower blood plexus was assumed to contain 90% blood and 10% dermis tissue. The optical parameters (μ_a, μ_s, g, n) of these two layers were calculated by adding the fractional contributions of their components (Jacques 1991b, Jacques *et al*, 1992b). For example, the refractive index of the upper blood plexus was estimated as:

$$n = 1.4 \times 90\% + 1.33 \times 10\% = 1.39 \qquad (25)$$

In summary, these calculations can be expressed in the following matrix formula:

Table 3. The seven layer skin optical model. The upper blood plexus layer was assumed to consist of 10% blood and 90% dermis tissue, while the lower blood plexus layer was postulated to contain 90% blood and 10% dermis tissue.

Layer	d (μm)	n	g (442/520 nm)	μ_a (cm^{-1}) (442/520 nm)	μ_s(cm^{-1}) (442/520 nm)
air		1.0			
Stratum Corneum	10	1.45	0.9/	190/	2300/
Epidermis	80	1.4	0.75/0.77	56/40	570/570
Papillary Dermis	100	1.4	0.75/0.77	6.7/5	700/500
Upper Blood Plexus	80	1.39	0.77/0.79	67/24.5	680/500
Reticular Dermis	1500	1.4	0.75/0.77	6.7/5	700/500
Deep Blood Plexus	70	1.34	0.96/0.96	541/181	520/500
Dermis	160	1.4	0.75/0.77	6.7/5	700/500
Sub-cutaneous Fat		1.46			

$$\begin{bmatrix} \mu_a \\ \mu_s \\ g \\ n \end{bmatrix} = \begin{bmatrix} \mu_a^1 & \mu_a^2 \\ \mu_s^1 & \mu_s^2 \\ g^1 & g^2 \\ n^1 & n^2 \end{bmatrix} \bullet \begin{bmatrix} f_1 \\ f_2 \end{bmatrix} \qquad (26)$$

where f_1 and f_2 are the percentages of component 1 and 2, superscript 1 and 2 in the first term of the right side denote the optical properties of component 1 and 2 respectively. The absorption coefficients of blood were read from figure 3 in Jacques and Keijzer, 1991. The g value of blood is about 0.98 and its μ_s value was assumed to be about 500 cm^{-1} (Jacques and Keijzer, 1991).

4.3.2 The distribution of excitation laser light inside skin tissue

Although being simplified into seven uniform parallel layers, the above skin model is still too complicated for its transport equation to be solved analytically. We used Monte Carlo simulation to solve this problem.

In our laser induced autofluorescence decay experiments, the illumination beam was 10 mm wide and has a divergence angle of 10°. The fluorescence detection spot had a diameter of only 3 mm and therefore the edge effects to the central part (i.e. the fluorescence detection volume) could be neglected (Keijzer *et al*, 1989). In this way, our problem became a one-dimensional problem which was much easier to solve. Figure 33

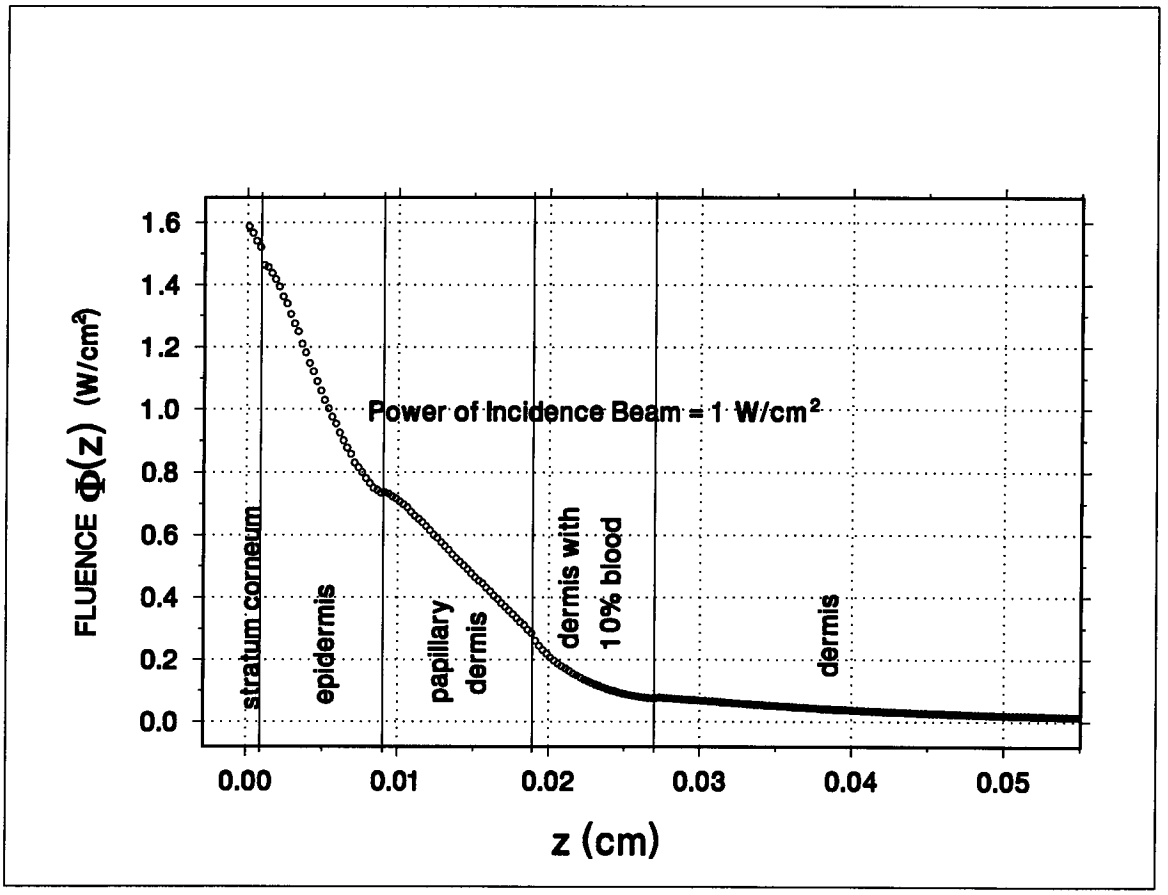

Figure 33. Monte Carlo simulation results of excitation laser light (442 nm) distribution in skin tissue (infinitely wide beam, normal incidence, 1,000,000 photons were launched).

shows the excitation light (442 nm) distribution inside the skin tissue as a function of depth z for a incident intensity of 1 W/cm^2. A million photons were launched in the Monte Carlo simulation to obtain this curve. The fluence in the stratum corneum is about 1.6 times of the incident fluence showing the photon energy pile-up near the air-tissue interface due to back-scattering. This effect does not violate the conservation of energy and has been verified experimentally (Jacques, 1989). For $z > 500$ μm (0.05 cm), the fluence $\Phi(z) \rightarrow 0$. Therefore, very little laser light (442 nm) can penetrate deeper than the color border shown in figure 32 to excite autofluorescence in the lower dermis which fluoresces in a color different from the upper dermis. The epidermis has negligible fluorescence emission. The excitation light fluence in the stratum corneum is 2 to 5 times of the fluence in the upper dermis. Considering the excitation light distribution and the fluorophore distribution, only the stratum corneum and the upper dermis ($z < 500$ μm) will be excited to fluoresce in *in vivo* autofluorescence measurements. These two skin layers have very different chemical environments (Montagna *et al*, 1992) and their fluorophores may also be different.

4.3.3 Autofluorescence escape from inside the skin tissue

Fluorescence emitted at depth z inside the tissue will be scattered and absorbed by the tissue in its way to reach the tissue surface. As a result, the fluence of an infinitely wide

plane fluorescence source will be attenuated before reaching the surface. The light from a point fluorescence source (located at depth z inside the tissue) will be attenuated and spread into a circular spot by the time it comes out of the tissue surface. The intensity distribution of the circular spot is called the fluorescence escape function, $E(\lambda_{em},r,z)$ (Kerjzer *et al*, 1989b).

Figure 34 shows the fluence distributions inside the tissue generated by three infinitely wide plane fluorescence sources located at different depths of the skin tissue. A million photons were launched to obtain each curve. The deeper the source, the more it was attenuated before the light reaches the surface. Figure 35 gives examples of fluorescence escape functions of three different depths of fluorescence point sources inside the skin tissue. The $E(\lambda_{em},r,z)$ maximum of the stratum corneum at λ_{em} =520 nm is about 30 times larger than that of the upper papillary dermis. We simulated 92 point sources located at different depths of the skin tissue (z ranging from 0 to 500 μm). When z increases, the maximum height of $E(\lambda_{em},r,z)$ decreases, while its width increases. But even for the point source located at 500 μm depth, the FWHM of $E(\lambda_{em},r,z)$ is only 0.58 mm for λ_{em} =520 nm which is still much smaller than the illumination laser beam size (10 mm). Therefore, in this specific case, we could still use the one-dimensional approximation to calculate the observed fluorescence.

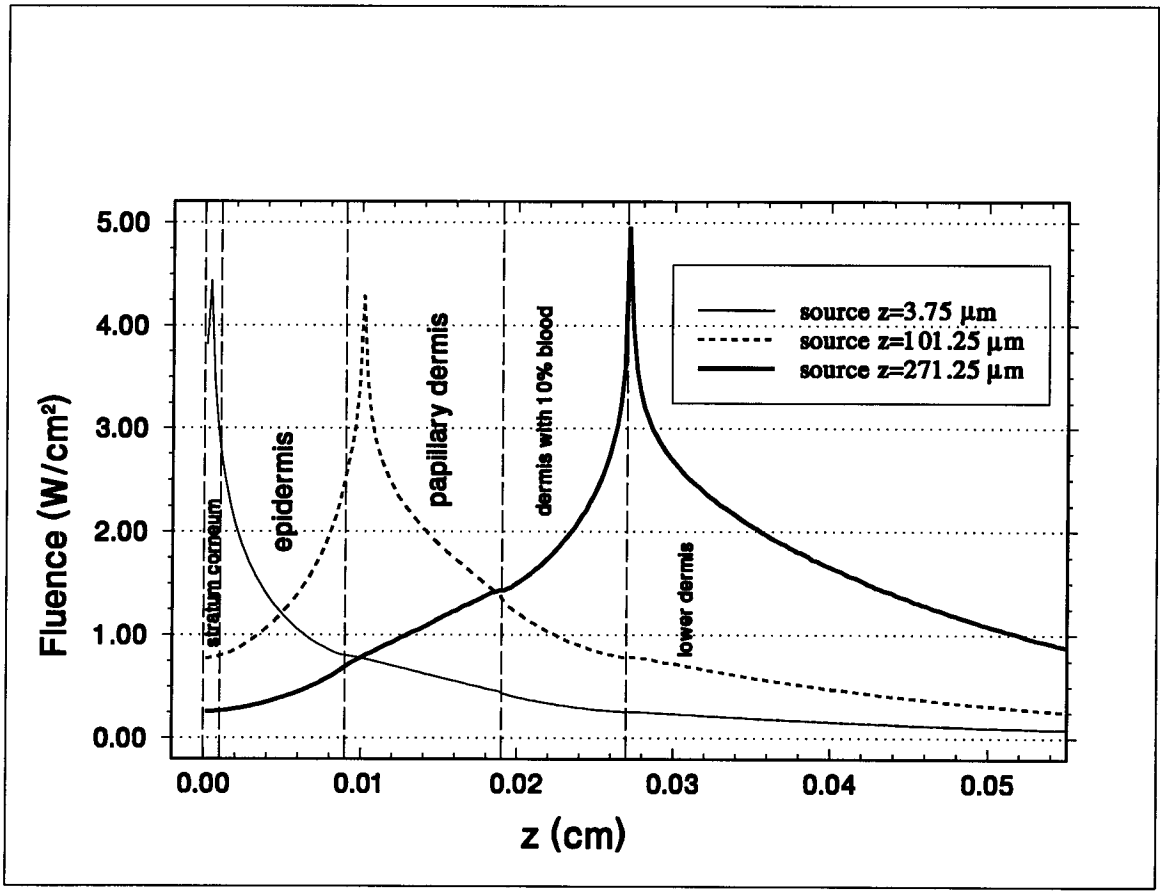

Figure 34. Fluorescence fluence vs. z as calculated by Monte Carlo simulation of infinitely wide plane fluorescence source at different depths of the skin tissue. 1,000,000 photons were launched to obtain each curve, fluorescence emission wavelength λ_{em} = 520 nm.

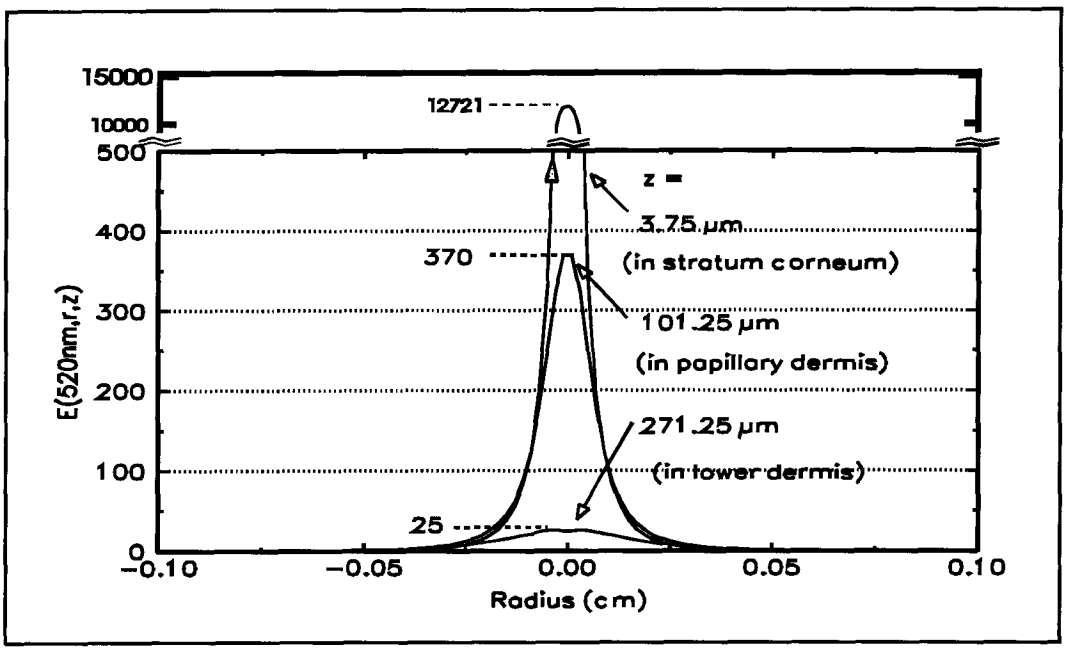

Figure 35. Fluorescence escape functions for three different depths of point sources. 1,000,000 photons were launched for each source.

4.3.4 Fluorescence fractional contributions of different skin layers

As a one-dimensional problem, once the excitation and emission wavelength are selected (442 nm and 520 nm, respectively), the excitation fluence distribution $\Phi(z)$ in our skin model is a function of z only as shown in figure 33. The intrinsic fluorescence coefficient $\beta(z)$ is also a function of z only as shown by the MSP measurements (figure 30). We can integrate the fluorescence escape function $E(\lambda_{em},r,z)$ over r and θ first in Eq.(20) in order to calculate the fractional contributions of autofluorescence of different skin layers.

$$E(\lambda_{em},z) = \int_0^{2\pi}\int_0^{\infty} E(\lambda_{em},r,z)rdrd\theta \qquad (27)$$

When the emission wavelength is selected (520 nm), this function become dependent on z only again. We denote it as $E(z)$. Then the fluorescence contribution from a specific layer (from z1 to z2) can be calculated as following:

$$F_{layer(z1\to z2)} = \int_{z1}^{z2} \Phi(z)\beta(z)E(z)dz \qquad (28)$$

$\Phi(z)$ is shown in figure 33. $E(z)$ is shown in figure 36 as calculated by Monte Carlo simulation. To obtain each data point, a million photons were launched. The intrinsic fluorescence coefficient $\beta(z)$ can be estimated from the autofluorescence images of excised skin tissue sections (figure 29) and the autofluorescence spectra on different locations of

the sections (figure 30) obtained by the MSP measurements. The autofluorescence emission in upper dermis is 10 times stronger than that of the stratum corneum. However, there is about 25% empty space (dark areas) in the autofluorescence image of upper dermis, therefore the average β value of upper dermis was estimated to be about 7.5 times that of the stratum corneum. The epidermis autofluorescence is negligible, its β value was therefore set to be zero. Figure 37 shows the β distribution inside the human skin.

The product, $\Phi(z) \bullet E(z)$, represents the effectiveness to obtained autofluorescence signal from different depths inside the skin. Figure 38 shows the $\Phi(z) \bullet E(z)$ versus z curve. It decreases faster than both $\Phi(z)$ and $E(z)$. The integration of $\Phi(z) \bullet E(z)$ over the stratum corneum (10 μm thick only) is equal to 4.53×10^{-4}, while the integration over the whole dermis is 3.49×10^{-4}. We therefore concluded that *in vivo* tissue fluorescence measurement is a surface enhanced detection technique. Fluorophores located in the surface layer are far more easy to detect than fluorophores in deep tissue layers. This is caused by both the excitation light distribution inside the tissue and the fluorescence escape efficiency, i.e., the fluorescence light which survives tissue reabsorption and scattering. The back-scattering causes the excitation photons to pile up in the near surface region of the tissue and results in even higher light intensity in this region than the incident light intensity. The fluorescence light emitted near the surface is able to escape and reach the detector much more

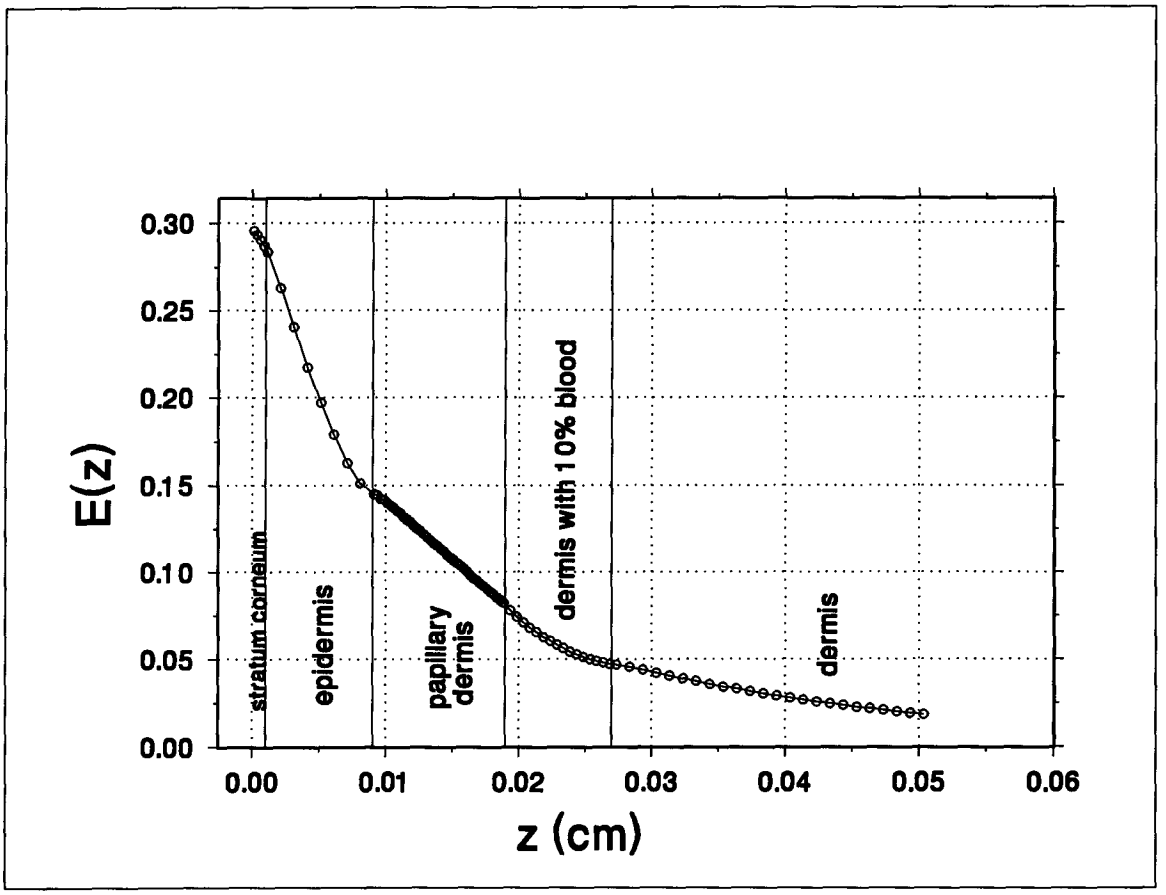

Figure 36. Fluorescence escape efficiency $E(z)$ versus the depth of the point source inside the skin tissue. To obtain each data point shown, 1,000,000 photons were launched in the Monte Carlo simulation.

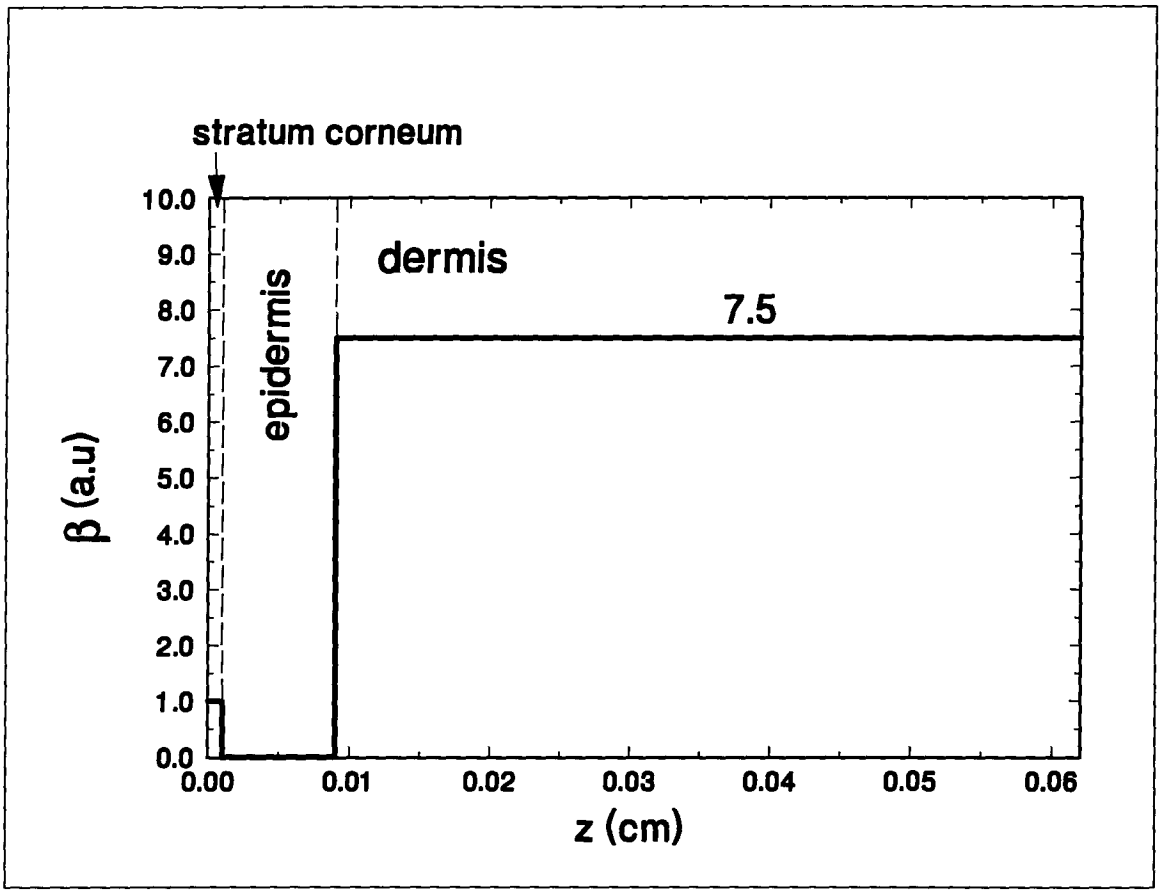

Figure 37. The intrinsic fluorescence coefficient β (relative) distribution in human skin. It was obtained by the MSP measurements of excised human skin tissue sections.

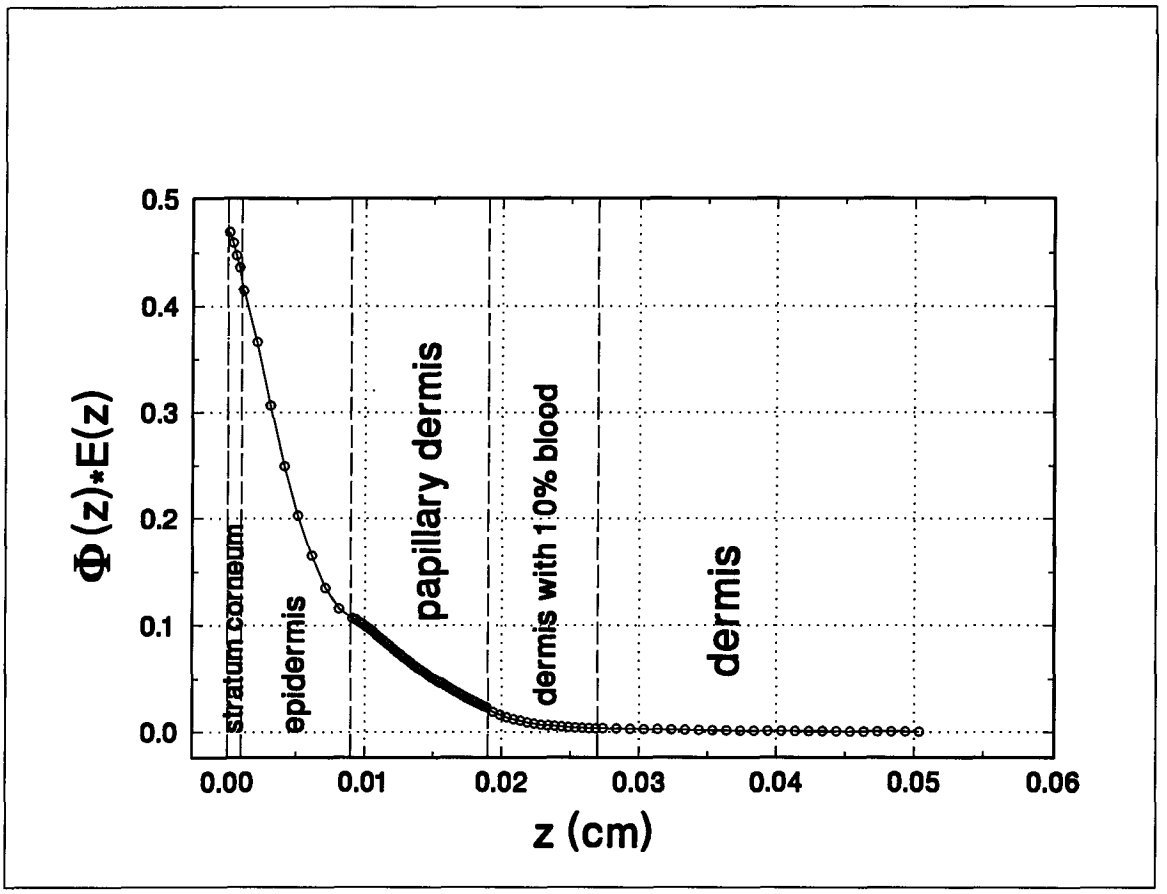

Figure 38. The effectiveness to observe autofluorescence signal from different depths inside the skin tissue — $\Phi(z) \bullet E(z)$ vs. z curve. This curve demonstrates that tissue fluorescence measurement is a surface enhanced technique. Surface fluorophores are much more easy to be detected than fluorophores deep inside the tissue.

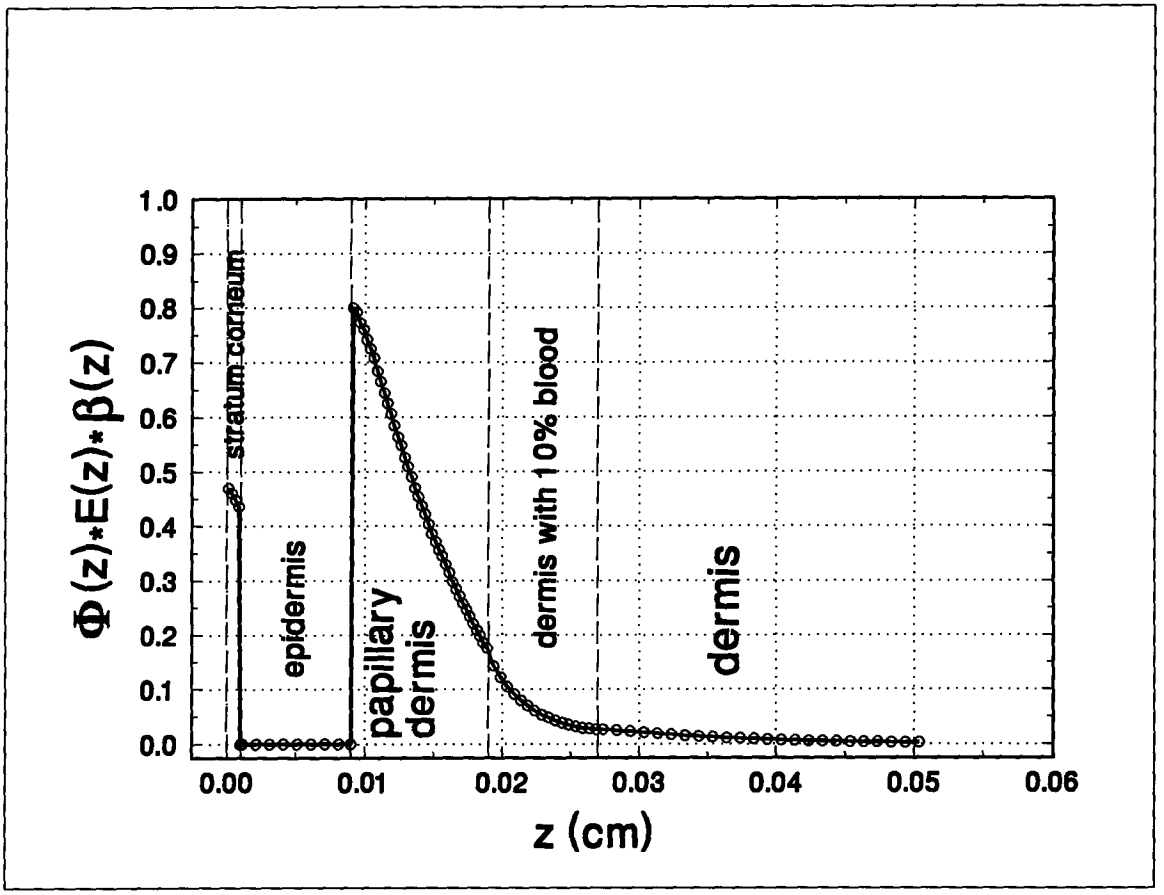

Figure 39. $\Phi(z) \bullet E(z) \bullet \beta(z)$ vs. z curve. Integration of this curve over different regions is used to calculate the fractional contributions of different skin layers to the measured total *in vivo* autofluorescence signal. Although the stratum corneum has a very weak fluorescence emission, the outermost skin layer still contributes about 15% to the observed total fluorescence signal because of both, the excitation light pile-up near the surface, and the larger values of its fluorescence escape function $E(z)$.

easily than fluorescence light emitted from deep inside the tissue.

Figure 39 shows the $\Phi(z) \bullet E(z) \bullet \beta(z)$ function versus the depth z curve. We integrated this curve to obtain the fractional contributions of different skin layers to the total measured *in vivo* autofluorescence signal. The results were:

$$F_{\text{stratum corneum}} = \int_{0}^{10\mu m} \Phi(z)\beta(z)E(z)dz = 4.53 \text{ x } 10^{-4} \qquad (29)$$

$$F_{\text{dermis}} = \int_{90\mu m}^{\infty} \Phi(z)\beta(z)E(z)dz = 26.20 \text{ x } 10^{-4}. \qquad (30)$$

The fractional contribution of the stratum corneum is

$$4.53/(4.53 + 26.20) = 0.1474 = 14.74\%, \qquad (31)$$

about 15%. The remaining 85% of the autofluorescence comes from the (upper) dermis.

4.4 Physical meaning of the double exponential decay

Under the illumination of (the laser) light, the fluorophore molecules in skin tissue are excited to higher energy states. When these excited molecules return to the ground state, they may release their energy through fluorescence emission or thermal relaxation as discussed in Chapter 1. These excited molecules may also react with nearby molecules (photochemical reactions) or they may decompose (photo-decomposition). These two processes will cause those molecules to cease fluorescing in a short period of time and

reduce the number of fluorophore molecules; therefore, a decrease of autofluorescence will be observed. We showed, in section 3.3.2, that the recovery of the skin autofluorescence takes approximately 6 days after the laser exposure. The chemical compositions of the fluorophore molecules and their detailed chemical changes induced by laser exposure are not known. Nevertheless, our quantitative measurements and mathematical analyses show that this decay is double exponential. Based on the skin autofluorescence microscopic structures, the skin optical model, and the Monte Carlo simulation results, we could elucidate the physical meaning of the double exponential decay dynamics.

Let us rewrite the autofluorescence decay equation (23) as:

$$I(t) = [a\ exp(-t/\tau_1) + c_1] + [b\ exp(-t/\tau_2) + c_2] \qquad (32)$$

Assume that the two parts of the right side of Eq. (32) originate from two separate sources. They have the same mathematical form and can be re-stated as $I = k\ exp(-t/\tau) + c$. Taking the derivative, we get

$$\frac{dI}{dt} = -\frac{k}{\tau} \cdot \exp(-t/\tau)$$
$$= -\frac{k}{\tau} \cdot \frac{I - c}{k}$$

i.e. $$dI = -\frac{I - c}{\tau} dt \qquad (33)$$

I(t) must be proportional to the number of excited fluorophore molecules N_F^e at time t. So Eq.(33) becomes

$$dN_F^e = -\frac{1}{\tau} N_F^e dt + \frac{c}{\tau} dt \qquad (34)$$

The first term of the right side of Eq.(34) means that the decrease (dN_F^e) of the number of fluorophore molecules which remain in the excited states is proportional to the number of excited fluorophore molecules (N_F^e) at the time t and the time interval dt because the larger the N_F^e and the time elapsed (dt), the more photochemical changes will occur and more fluorophore molecules will be changed into new molecules which will no longer fluoresce in a short period of time. Similarly, the higher the excitation light intensity, the more the excited molecules per unit volume and thus the faster the photochemical reaction or photo-decomposition. This is consistent with the results shown in figure 28 that τ_1 and τ_2 decrease with increasing exposure intensity.

When a beam of excitation light shines on a group of fluorophore molecules, there might be fluorophore molecules which are not in a state capable of interaction with the incoming photons. Some of these "extra fluorophore molecules" will change their states later on, get excited, and add to the N_F^e population at the time t. This amount of additional excitation is proportional to dt and consists of the second term of the right side in Eq.(34). The more the "extra fluorophore molecules", i.e. the weaker the excitation light intensity, the greater will be the contribution of this kind of "later on" excitation, i.e. the larger the parameter *c*. This agrees with the observation that c increases when the

excitation intensity decreases (figure 27). The increasing trends of parameters *a* and *b* with increasing exposure intensity are the results of both the decreasing of "extra fluorophore molecules" and the relative increasing of the fraction of fluorophore molecules which will be photochemically changed as the Eq.(24), i.e. $a + b + c = 1$, must be satisfied.

From the excitation laser light distribution and the fluorophore spatial distribution in skin tissue, we have concluded that under 442 nm laser light excitation, the observed *in vivo* skin autofluorescence mainly comes from two distinct areas: stratum corneum and upper dermis. The non-fluorescing epidermis separates these two skin layers. The chemical environments of these two areas are very different (Montagna *et al*, 1992). Their respective fluorophore molecules are also probably quite different. In addition, the excitation light fluence in the stratum corneum is much larger than in the dermis. Therefore, the rates of the laser induced photochemical changes of the two areas are very likely to show a large magnitude of difference. From table 2, one can see that the fast decay term has a small pre-exponential coefficient (small τ_1, small *a*). From the preceding section, we know that the stratum corneum contributes only about 15% to the observed *in vivo* autofluorescence signal, while the dermis contributes about 85%. We therefore concluded that the fast decay term in Eq.(23) or (32) corresponds to the laser induced chemical changes of the stratum corneum, while the slow decay term corresponds to the dermis. Parameter τ is a measure of the

speed of the laser induced photochemical changes of the fluorophores, while *a* and *b* represent the fractions, which decay due to laser induced photochemical changes, of the total fluorescence signal at time zero, and the constant term *c* (or c_1 and c_2) represents that there are some "extra fluorophore molecules" which will be excited eventually and continuously contributed to the excited fluorophore molecule population.

From table 2, at high excitation light intensity (64 mW/cm^2), *a* is equal to 0.14. It is probable that at such high excitation intensity, the non-photochemically changed fraction c_1 is small, and therefore *a* = 14% is close to the actual fractional contribution of the stratum corneum to the total detected signal. The calculated value using the seven layer skin optical model and Monte Carlo simulation in the preceding section is 15%. These two values are indeed very close, confirming our conclusion that the fast decay process represents the photochemical changing of the fluorophore(s) of the stratum corneum, while the slow process represents photochemical changing of the fluorophore(s) in the dermis. According to this postulate, the measured skin autofluorescence decay dynamics can be used to determine the fractional contributions of different skin layers to the measured total *in vivo* autofluorescence signal. We believe that the hypothesis in section 4.1 has been substantially proven.

4.5 Further test on the hypothesis of skin autofluorescence decay dynamics

To further test our conclusion in the preceding section that the two exponentials of the skin autofluorescence decay function correspond to the laser induced photochemical changes of the stratum corneum and the dermis respectively, two more experiments were carried out. One was to irradiate the excised skin tissue sections and measure the autofluorescence decay by using the MSP system. The other experiment was to irradiate the *in vivo* dermis directly.

Figure 40 shows the autofluorescence decay curve of the *in vitro* upper dermis measured by the MSP system. It is a slow single exponential decay. The fluorescence emission from the stratum corneum on the excised tissue section is too weak to allow accurate decay dynamics measurements.

To directly irradiate the dermis *in vivo*, the epidermis of a spot larger than 10 mm on the inner forearm of a volunteer was peeled off by developing a blister using a topical cantharone application. Monte Carlo simulation results of the light distribution in the skin with epidermis peeled off are shown in figure 41. In this situation too, only very little light can penetrate into the lower dermis ($z > 500$ μm). Therefore, the detected autofluorescence signal will again come mainly from the upper dermis ($z < 500$ μm). Figure 42 shows the autofluorescence decay curve on the skin spot with the epidermis peeled off. This curve decays slowly with time. It

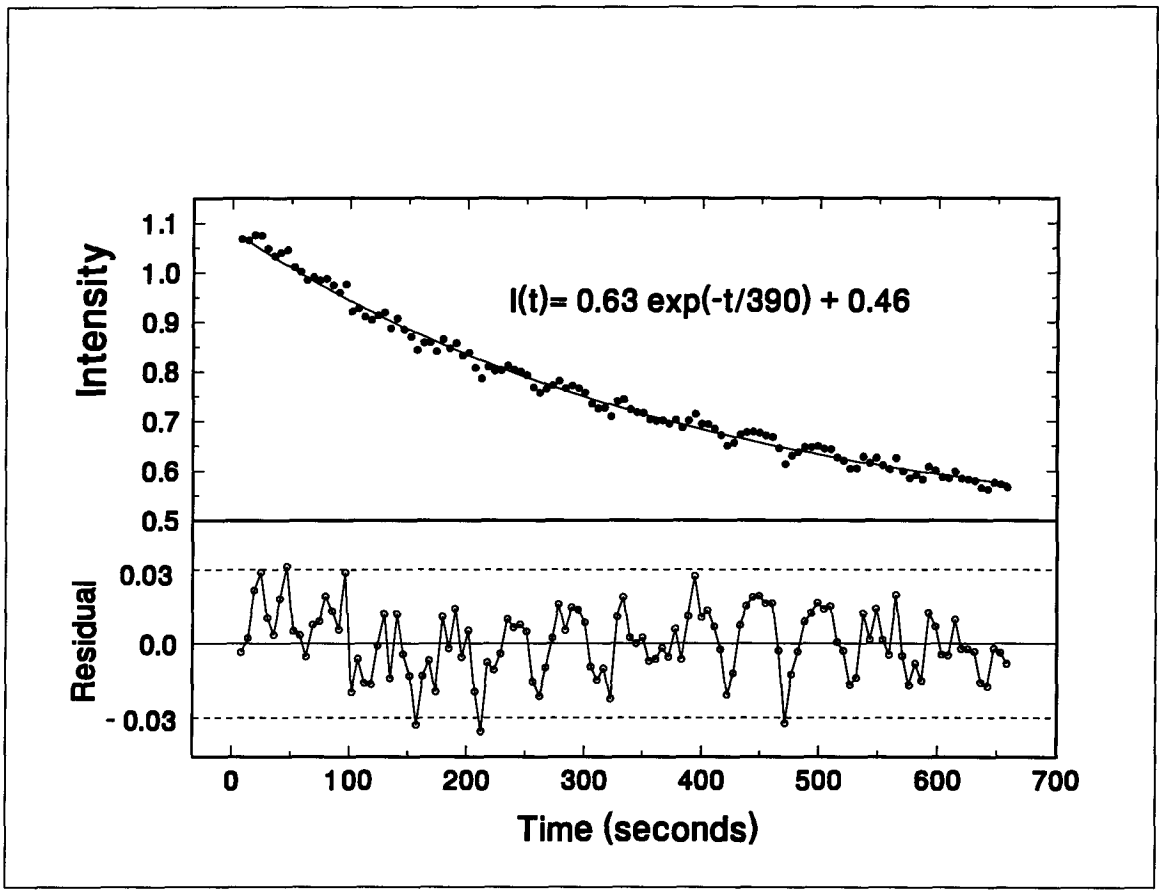

Figure 40. Autofluorescence decay of the upper dermis part on the excised skin tissue section during continuous 442 nm He-Cd laser exposure measured by the MSP system.

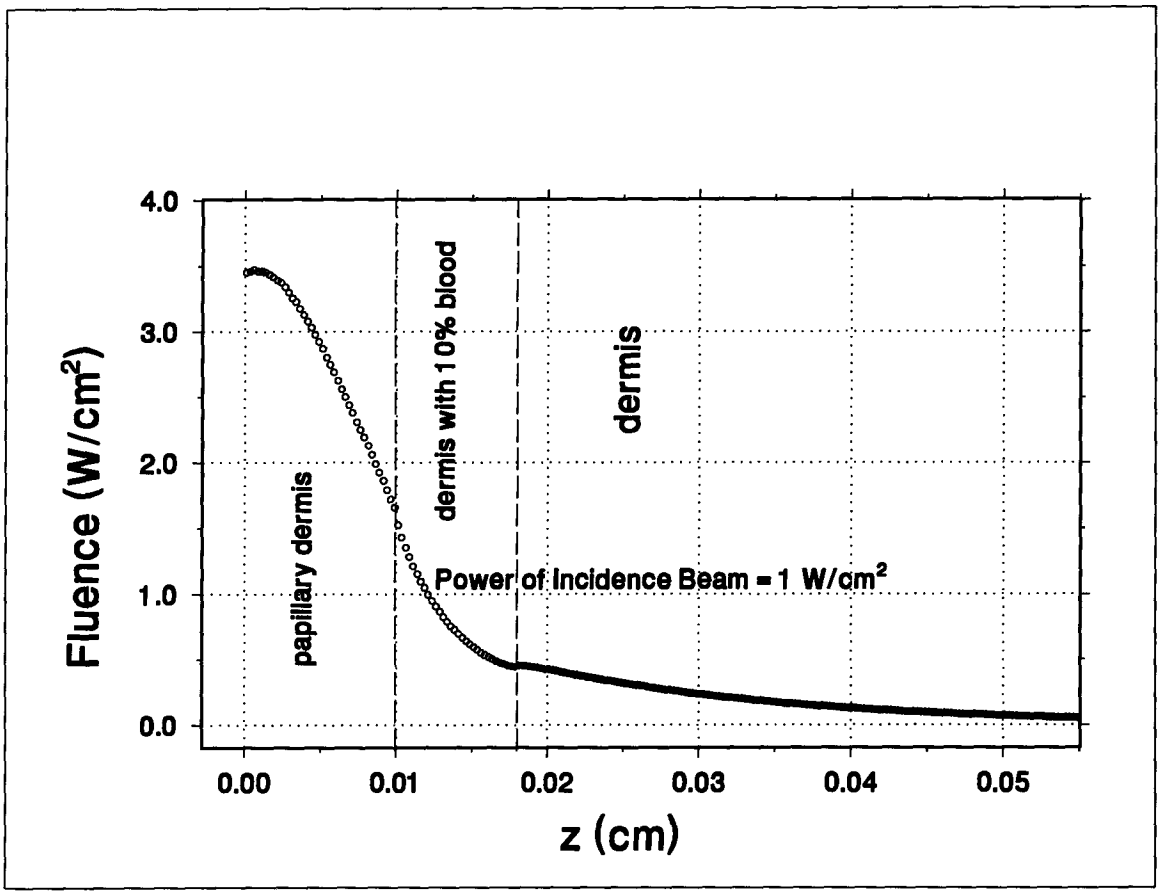

Figure 41. Excitation laser light (442 nm) distribution inside the *in vivo* skin with the epidermis peeled off. The results were obtained by the Monte Carlo simulation with 1,000,000 launched photons using optical parameters shown in table 3.

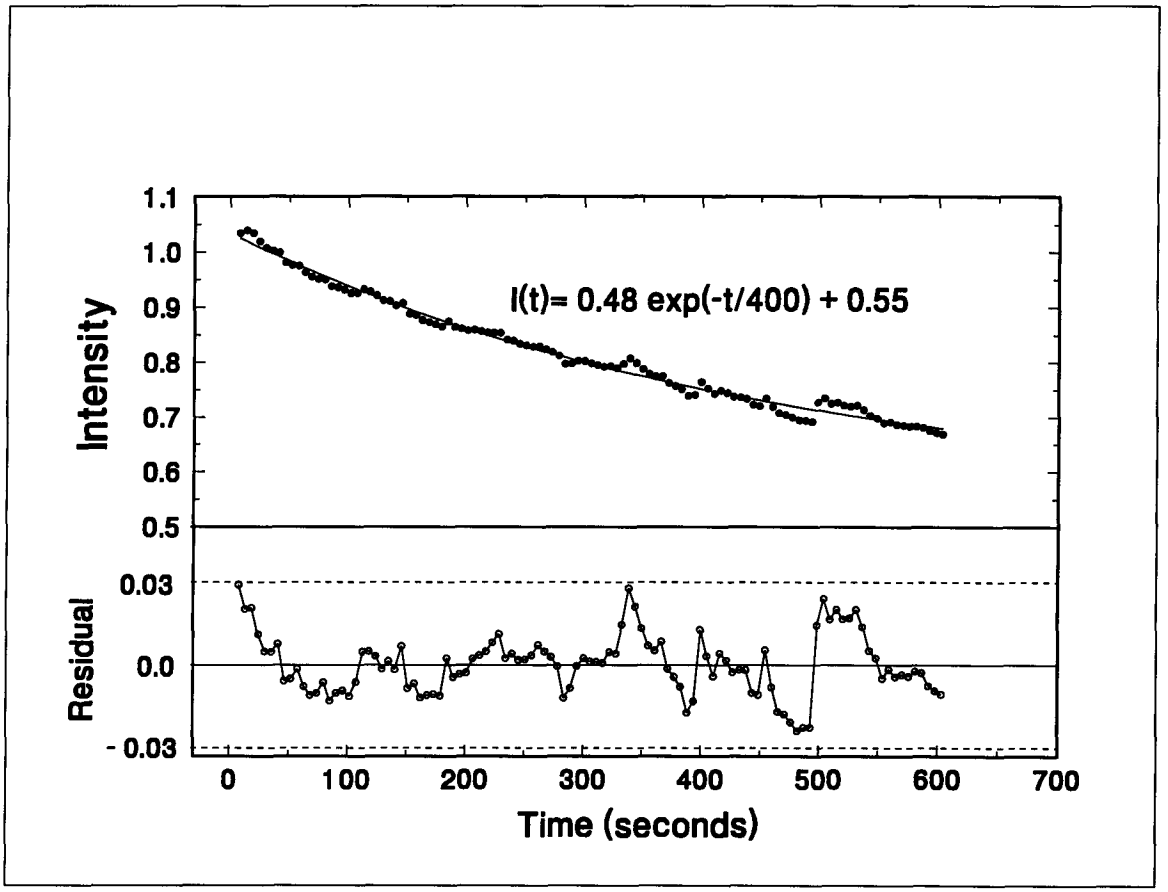

Figure 42. Autofluorescence decay of dermis *in vivo*. The epidermis was peeled off by developing a blister using a topical cantharone application.

shows large fluctuations probably because of the instability of the skin tissue system. For example, after the epidermis was peeled off, some fluid kept flowing out of the wound. The curve can be fitted to a single exponential but with large residuals.

These two experiments further confirmed our hypothesis that in the double exponential decay equation (23) or (32), the fast decay term corresponds to the laser induced photochemical changes of the stratum corneum, while the slow decay term represents the dermis.

CHAPTER 5: CONCLUSIONS AND DIRECTIONS FOR FUTURE RESEARCH

5.1 Conclusions

In conclusion, through experimental studies and theoretical modeling, the thesis hypotheses have been proven. Although the skin is composed of complicated inhomogeneous sub-structures, its optical properties can be quantitatively modeled and various modalities of *in vivo* skin spectroscopy can be used to extract information on skin status.

We have achieved significant progresses in both experimental studies of the optical properties and theoretical modeling of the basic light-tissue interaction in the human skin. The following are the major achievements of this work:

(1) Improvement in the instrumentation of *in vivo* skin spectroscopy. A computerized autofluorescence and diffuse reflectance spectroanalyser system using fiber optics and OMA techniques was designed and built allowing almost instantaneous spectrum acquisition (in less than 1 second) with high accuracy. A specially designed fiber holder allowed the illumination angle, pick-up angle, and the size of the illumination spot and the size of the pick-up spot to be changed as desired. Using this system, a combined diffuse reflectance and autofluorescence measurement procedure was implemented to assure correct interpretation and calibration of the autofluorescence spectra.

(2) Invention of a novel MSP for microscopic morphology and spectroscopy studies of *in vitro* skin tissue sections. Based on a unique fiber optic alignment mechanism, a novel MSP was developed and built which has all the functions of a conventional microscope plus the capability to provide spectral analyses on a selected micro area as small as a few microns of a microscopic object. The new system is easy to construct, easy to use, has higher spectral resolution and much shorter data acquisition time in comparison to conventional MSPs. Using this device, we obtained the autofluorescence microscopic morphology as well as intrinsic fluorescence spectra of different skin layers by examining excised skin tissue sections. This MSP has also been used to study the cell DNA staining in both absorbance and fluorescence microscopy modes. The system has now been used extensively at the B.C. Cancer Agency by researchers from Vancouver and elsewhere.

(3) Design of methods for quantitative monitoring of laser induced autofluorescence decay in *in vivo* skin. A measurement method was developed based on a computerized autofluorescence and diffuse reflectance spectroanalyser system. A fiber with a microlens was used to achieve uniform illumination. Special procedures were developed to remove autofluorescence signal fluctuations caused by the laser output power instability and the relative movements between the fiber holder and the subject being measured during 10 - 20 minutes of exposure time. A fluorescence imaging system was constructed to monitor the autofluorescence recovery after laser exposure.

A program was written to process the kinetic spectral data and non-linear curve fitting was used for mathematical analysis of the time function of the autofluorescence decay. Using these methods, the photophysical processes of laser induced skin autofluorescence decay were elucidated.

(4) Angular resolved diffuse reflectance spectra suggesting new way of obtaining information from different skin layers *in vivo*. Taking advantage of the fiber holder, the diffuse reflectance spectra of different body locations were measured on volunteers at different illumination angle and pick-up angle combinations. We found that the spectral shape is changed at different illumination and pick-up angles. This suggests that at different angles, the detected light penetrates into different depths inside the skin tissue due to the strong forward scattering properties of skin. The angular resolved diffuse reflectance $R(\alpha,\beta,\gamma)$ may be used as a new modality to derive information from multi-layered tissue (like skin) *in vivo*. Other modalities are spatial resolved and time resolved reflectance techniques (see chapter 1). However, the successful applications of these modalities in practice require further breakthrough in theoretical studies of light propagation in multi-layered biological tissue.

(5) Complete study of the autofluorescence spectroscopic properties of *in vivo* skin. Skin autofluorescence spectra at different excitation wavelengths from 350 nm to 470 nm were measured. We found that the emission spectra change with excitation wavelengths. When the excitation wavelength

increases, the wavelength corresponding to the maximum intensity on the emission spectrum also increases. In terms of energy, the most probable energy of fluorescence emission photons tends to increase linearly with the increasing excitation photon energy. The plot of the fluorescence spectrum maximum intensity versus the excitation wavelength shows a maximum at 380 nm.

It has been commonly assumed that, for a simple fluorophore molecule, the shape of the emission spectrum is independent of the excitation wavelength. The unusual behavior of skin autofluorescence properties suggests two distinct possibilities about the skin fluorophores. One possibility is that there are more than one predominant type of fluorophore molecule inside the skin tissue responsible for the visible autofluorescence. The other possibility is that there is only one type of fluorophore molecule, but that this fluorophore has a complicated structure and special properties (e.g. multiple fluorescing sites) which lead to the above unusual phenomenon. A complete understanding of these physical properties of skin autofluorescence emission must be based on the chemical identification of the skin fluorophores.

(6) Using diffuse reflectance spectrum to calibrate autofluorescence spectrum. Based on some intuitive considerations on the fluorescence escape processes and diffuse reflectance measurements, we proposed that diffuse reflectance (R) can be used as a first order approximation of the fluorescence distortion factor (f) to calibrate the

autofluorescence spectrum. The calibrated spectrum is equal to the measured spectrum divided by R. We calibrated our skin autofluorescence spectra at different excitation wavelengths. The results showed that in all cases, the calibrated spectra were more symmetric and also smoother in comparison to the measured, original spectra. The valleys due to the oxyhaemoglobin absorption are also eliminated by this calibration. Monte Carlo simulations have demonstrated that R is a good first order approximation of f at least for semi-infinite uniform turbid media.

(7) Discovery of skin fluorophore spatial distribution and spectral differences. Using the new MSP, we worked out the natural fluorophore distribution in skin tissue and their spectral differences by examining excised skin tissue sections under 442 nm laser excitation. Microscopic fluorescence imaging showed that the dermis and the subcutaneous fat have strong autofluorescence emission, the stratum corneum autofluoresces with a weak signal, while the epidermis yields negligible autofluorescence. The color of the autofluorescence from the upper dermis and the lower dermis is quite different. The upper dermis autofluorescence is more yellow and the lower dermis is more green. Autofluorescence spectra of these two areas measured by the MSP showed significant differences. The spectrum of the lower dermis shifts toward the shorter wavelengths. The positions of the spectrum maxima of the upper and lower dermis differ by 20 nm. This difference may be

related to the different chemical compositions of the papillary dermis and the reticular dermis.

(8) Discovery of the double exponential decay of skin autofluorescence intensity during continuous laser exposure. Our quantitative measurements and mathematical analyses revealed that *in vivo* skin autofluorescence decays double exponentially with a fast process and a slow process during a continuous 442 nm laser exposure. The time constants of the two processes differed by an order of magnitude. The decay parameters (a, b, c, τ_1, τ_2, see Eq.(23)) change with exposure intensity. Parameters a and b have the tendency to increase when the exposure intensity increases, while c has the tendency to decrease with increasing exposure intensity; τ_1 and τ_2 decrease when the exposure intensity increases. Autofluorescence imaging showed that a complete recovery of the autofluorescence on the exposed skin site takes about 6 days.

(9) Development of a seven layer skin optical model. Based on the anatomy structure of the human skin, the optical parameters of different skin layers published in literature, and our own MSP measurements on excised skin tissue sections, a seven layer skin optical model was developed to explain the autofluorescence decay dynamics. This is the most practical skin optical model available since we obtained a true fluorophore distribution and true intrinsic autofluorescence spectra by the MSP measurements. Other tissue optical models assume a uniform fluorophore distribution in tissue which is not true according to the MSP results.

(10) Monte Carlo simulation to solve the Boltzmann equation of radiative transfer for the seven layer skin optical model. Monte Carlo simulation was used to numerically solve the transport equation of the seven layer model skin. The distribution of excitation laser light in the skin tissue and the fluorescence escape efficiencies for point sources located at different depths of the skin were obtained. There is very little light that can penetrate into the lower dermis ($z > 500$ μm). The fluence of the excitation light in the stratum corneum is much higher than that of the dermis. Furthermore, fluorescence light sources in the stratum corneum have much higher fluorescence escape efficiency than sources in the dermis. Therefore, tissue fluorescence measurement is a surface enhanced technique. Fluorophores located near the tissue surface are much easier to detect than fluorophores deep inside the tissue. In our model skin, the outermost layer, stratum corneum, is very thin (10 μm) and has a much lower intrinsic fluorescence coefficient than the dermis. Nevertheless it still contributes about 15% to the observed *in vivo* autofluorescence signal, while the upper dermis contributes the remaining 85%.

(11) Elucidation of the physical meanings of the skin autofluorescence decay dynamics. Combining the fluorophore micro-distribution, the Monte Carlo simulation results, and the decay parameters changing trends with increasing exposure intensity, we elucidated the physical meanings of the skin autofluorescence double exponential decay dynamics. The

observed *in vivo* skin autofluorescence mainly comes from two distinct sub-structures: the stratum corneum and the upper dermis. These two layers are separated by a non-fluorescing epidermis and have very different chemical environments. Their respective fluorophores are probably different also. The excitation light fluence in the stratum corneum is much larger than that of the dermis. Therefore, the rates of the laser induced photochemical changes of the two areas are very likely to show a large difference. The fast decay term (in Eq.(23) or (32)) corresponds to the laser induced photochemical changes of the stratum corneum, while the slow decay term represents the dermis. Parameter τ is a measure of the speed of the laser induced photochemical changes of the fluorophores, while parameters *a* and *b* represent the fractions which will decay due to laser induced photochemical changes among the total fluorescence signal at time zero. The constant term *c* (or c_1 and c_2) represents the presence of some "extra fluorophore molecules" which will be excited eventually and continuously contributing to the excited fluorophore molecule population.

The measured skin autofluorescence decay dynamics can be used to determine the fractional contributions of different skin layers to the measured total *in vivo* autofluorescence signal. From the measured normal skin autofluorescence decay parameters (table 2), we estimated that the fractional contribution of the stratum corneum to the measured total *in vivo* autofluorescence signal is about 14%, while the calculated value for our model skin by Monte Carlo simulation is 15%

showing excellent agreement between estimated value and theoretical modeling. The dermis contributes the remaining 85% of the observed *in vivo* signal.

5.2 Directions for future research

As outlined above, studies has been completed on the optical properties of normal skin in terms of macroscopic *in vivo* diffuse reflectance spectroscopy, autofluorescence spectroscopy, and temporal behavior of autofluorescence signal during continuous laser exposure as well as microscopic *in vitro* fluorophore distribution and spectral differences. As a result, several interesting physical phenomena have been discovered. Using the MSP *in vitro* measurement results and the published optical parameters of different skin layers and of blood, we built up a seven layer skin optical model. Monte Carlo simulation of light propagation in the model skin revealed the distribution pattern of excitation laser light in the skin and the fluorescence escape efficiencies of point sources located inside different depths of the skin tissue. The theoretical modeling unified the microscopic properties with the macroscopic *in vivo* skin measurements. It gives us a very clear physical picture about the *in vivo* skin autofluorescence processes. The physical meanings of the skin autofluorescence double exponential decay dynamics were also elucidated.

However, the chemical composition of skin fluorophores, their photochemical changes during continuous laser exposure, and the biological mechanisms of autofluorescence recovery after laser exposure are not yet known and deserve further studies. The identification of the skin fluorophores will also help understanding the interesting phenomenon of the skin autofluorescence emission spectrum shift, i.e., that the most probable energy of fluorescence emission photons tends to increase linearly with the increasing excitation photon energy. Even without the biochemical data, after further improvement of the understanding on the physics of the normal skin optical properties, our next step will be to study the optical properties of malignant and pre-malignant skin tissues. We believe that the differences of the optical properties of the normal and malignant skin tissues exist and that these can be exploited for diagnosis of various skin lesions non-invasively. This principle can also be used to follow the progress of skin lesion treatment with either physical or chemical methods.

5.2.1 Chemical identification of skin fluorophores

Identifying fluorophores in a biological tissue is a comprehensive task because the chemical composition of tissue is very complex. The fluorescence properties of fluorophores may be altered by the extraction procedures and the fluorescence spectra may be dependent on the local molecular environment (e.g. tryptophan is a typical example, Baraga *et*

al, 1991). This research needs a multi-disciplinary cooperation of chemists, biochemists, and physicists. For example, the fluorophore distribution in skin tissue revealed by our MSP measurements suggests that one should search for the fluorophores in the dermis, not in the epidermis.

If the skin fluorophores are identified and their relationships with metabolic activities are worked out, autofluorescence spectroscopy can become a very powerful tool for skin biology studies. Another interesting subject will be to study the laser induced photochemical changes of these fluorophores. These will help us to understand the chemical mechanism of the laser induced skin autofluorescence decay. In turn, the autofluorescence decay can be used to study these photochemical changes. More interestingly, the biological mechanism of autofluorescence recovery after laser exposure may be very significant for the everyday interaction of our skin, an optical organ, with sunlight.

5.2.2 Applications of skin optics in non-invasive diagnoses

As reviewed in chapter 1, many applications have been found for diffuse reflectance and autofluorescence in skin disease diagnoses. To assess the potential and improve the reliability of the existing techniques as well as to develop new diagnosis modalities, a complete study of the optical properties of various malignant and pre-malignant skin tissues should be carried out in the future. Instruments, methods of

in vivo macroscopic and *in vitro* microscopic measurements and imaging, as well as theoretical modeling developed in this thesis could find important applications in these future developments. For example, the angular resolved diffuse reflectance may be used to estimate the depth of the invading disease, e.g. melanoma. The MSP can determine the distribution of fluorophores in a lesion and their intrinsic spectra. This knowlegde can then be used as an input into the Monte Carlo simulation program which can readily be used to extract further information from the measured *in vivo* signals. Although, usually, using large illumination intensity can improve the signal to noise ratio of fluorescence measurements, our results in the laser induced autofluorescence changes suggest that large exposure intensity causes fast autofluorescence signal decay which will lead to inaccuracy in quantitative studies. A trade-off between the signal to noise ratio and the systematic error caused by the laser induced autofluorescence decay must be considered. Measures must be taken to avoid unnecessary strong light exposure during the measurements. However, if the experiment is properly designed and implemented, the autofluorescence decay dynamics measurement upon laser exposure can be used to derive structure information of the normal tissue and diseased tissure in a non-invasive way.

To localize the exact position of a disease, imaging modalities based on spectroscopic data must be developed. As we have already concluded, fluorescence measurement is a very sensitive technique and specifically fluorescence measurement

of turbid biological tissue is a surface enhanced technique. We predict that autofluorescence imaging will find important applications[3] in non-invasive diagnoses of diseases in skin, as well as other organs of our body. The autofluorescence imaging system for monitoring the autofluorescence recovery after laser exposure can be used as a starting point in these future developments. As an example of further applications of our skin optical model and Monte Carlo simulation, the following is an estimate of the spatial resolution of skin autofluorescence imaging.

When imaging a turbid biological tissue using autofluorescence, one can only focus on the surface of the tissue due to scattering. A point fluorescence source located at depth z will become a circular spot at the surface because of the re-absorption and scattering of the tissue to the fluorescence light. This will cause the spatial resolution of tissue autofluorescence imaging to become worse than that determined by diffraction effect. The intensity distribution of the circular spot is determined by the fluorescence escape function $E(\lambda_{em},r,z)$. We define the spatial resolution (δ) to be equal to the FWHM of the $E(\lambda_{em},r,z)$ function as shown in figure 43. We have already calculated $E(\lambda_{em},r,z)$ for our model skin in

---

[3] Significant differences in autofluorescence spectra (excited by 366 nm UV light) of normal skin and melanomas have already been reported by Lohmann *et al*, (1988, 1991). There has been no report of the use of autofluorescence imaging for skin diseases diagnoses yet. For applications of autofluorescence imaging in other organs, see references given in chapter 1.

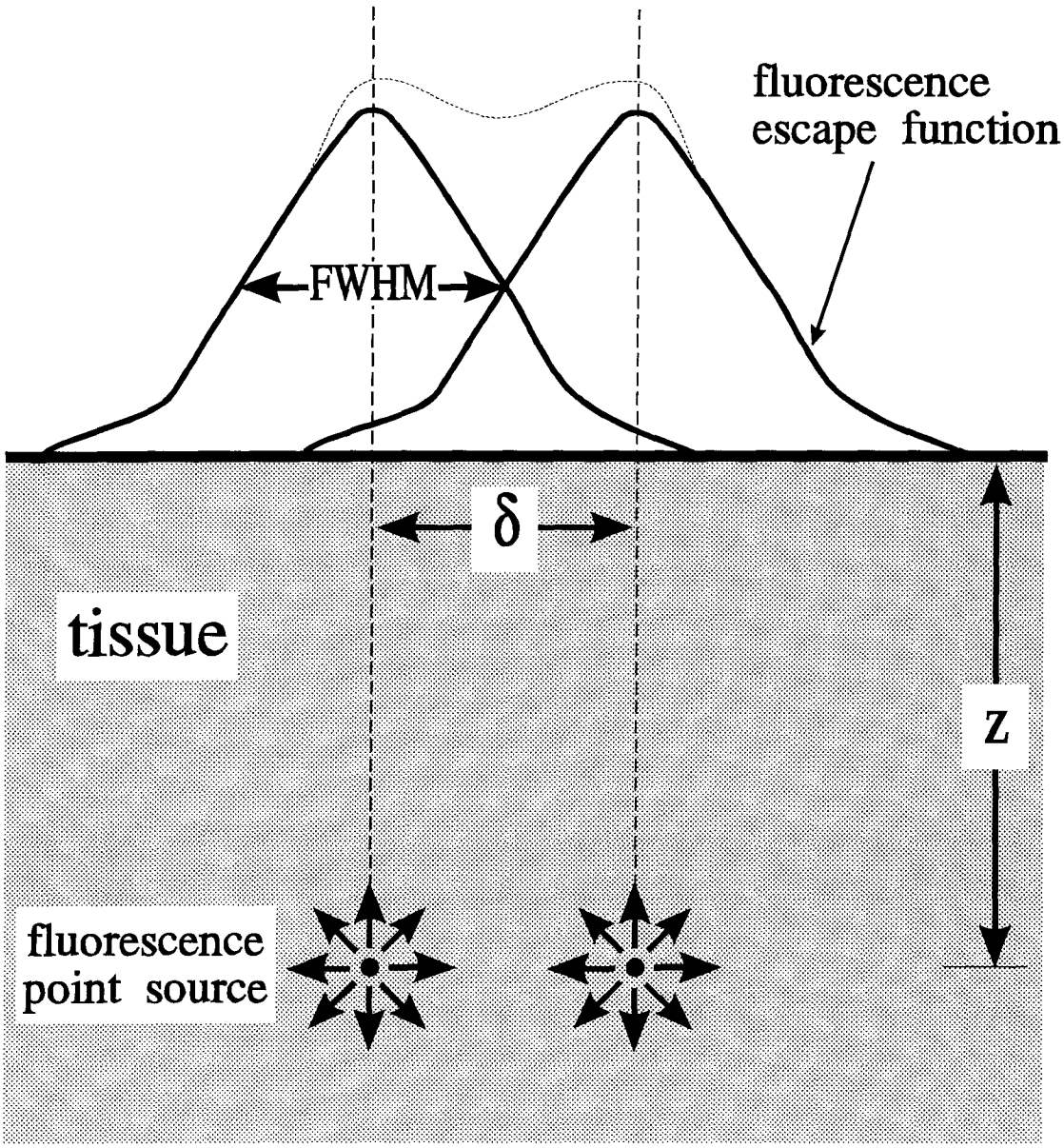

Figure 43. Definition of the spatial resolution for tissue fluorescence imaging. A point fluorescence source located in depth z will become a circular spot due to tissue re-absorption and scattering. The FWHM of the spot is defined as the spatial resolution δ.

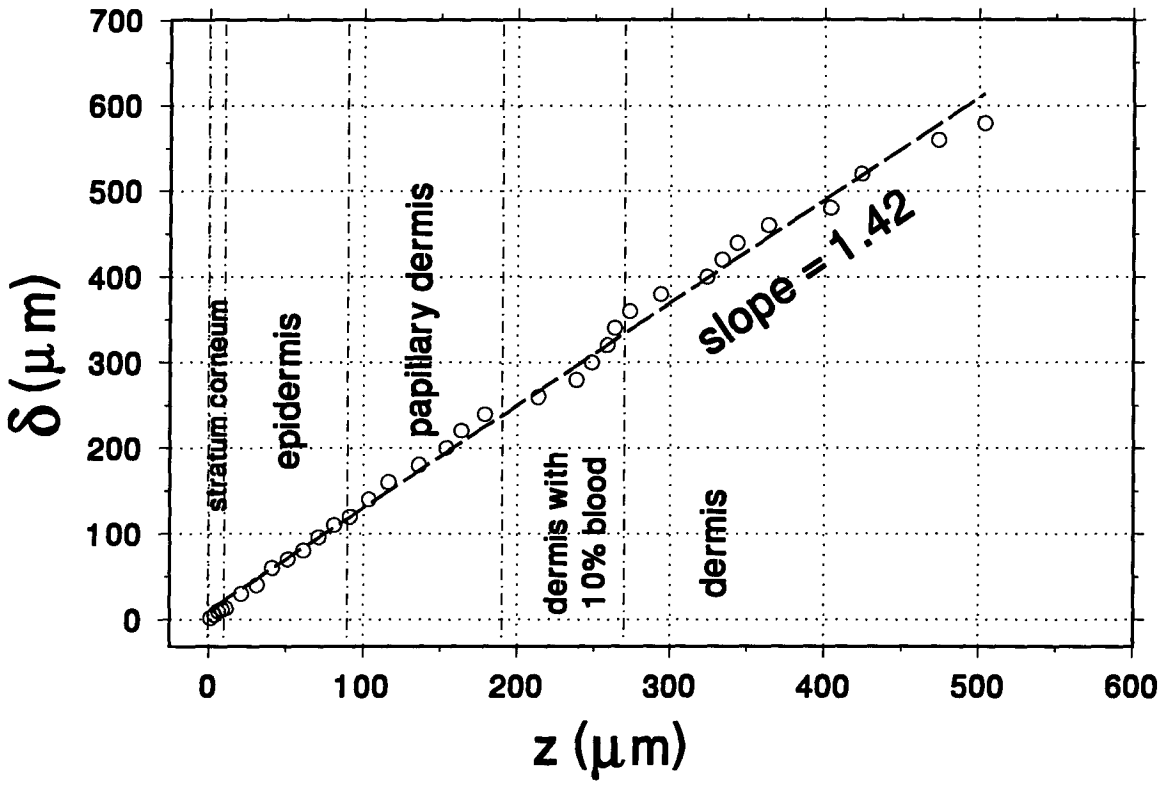

Figure 44. Spatial resolution (δ) of skin autofluorescence imaging changes as a function of depth z where the fluorescence point sources are located. The data were calculated using the seven layer skin optical model and the Monte Carlo simulation technique. Note that the minimum δ data point on the graph is 1.8 μm which corresponds to a source depth of 1.25 μm inside the tissue. This δ value is still larger than the fluorescence wavelength (λ = 520 nm = 0.52 μm). The diffraction limited spatial resolution of imaging is equal to the wavelength of light.

chapter 4 using Monte Carlo simulation. Figure 44 shows that δ changes as a function of depth z where the fluorescence point sources are located. One can see that δ increases almost linearly with the increasing source depth z ($\delta \approx 1.4z$). The minimum δ data point on figure 44 is 1.8 μm which corresponds to a source depth of 1.25 μm inside the tissue. This δ value is still large than the fluorescence wavelength (λ = 520 nm = 0.52 μm). The diffraction limited spatial resolution of an image is equal to the wavelength of light used. When the source is put on the surface (z = 0), the calculated δ value is smaller than λ and the spatial resolution at this case is determined by diffraction effect. The δ vs. z curve further confirmed that tissue fluorescence measurement is a surface enhanced technique. Not only is it difficult to detect fluorescence sources deep inside the tissue, but also the spatial resolution of fluorescence imaging for deep sources becomes significantly degraded. This example also demonstrates how different is skin optics from the traditional geometric optics and wave optics of homogeneous media.

When imaging a tissue using diffusely reflected light, the spatial resolution could also be obtained using methods developed in this thesis. First, we could calculate the reflected light distribution on the tissue surface, R(x,y), using Monte Carlo simulation. Then, the angular distribution of the local radiance, $L(\mathbf{r},\mathbf{s})$, at an interested point inside the tissue could be calculated. The negative of this radiance, $-L(\mathbf{r},\mathbf{s})$, could be used to launch photons at that point, and

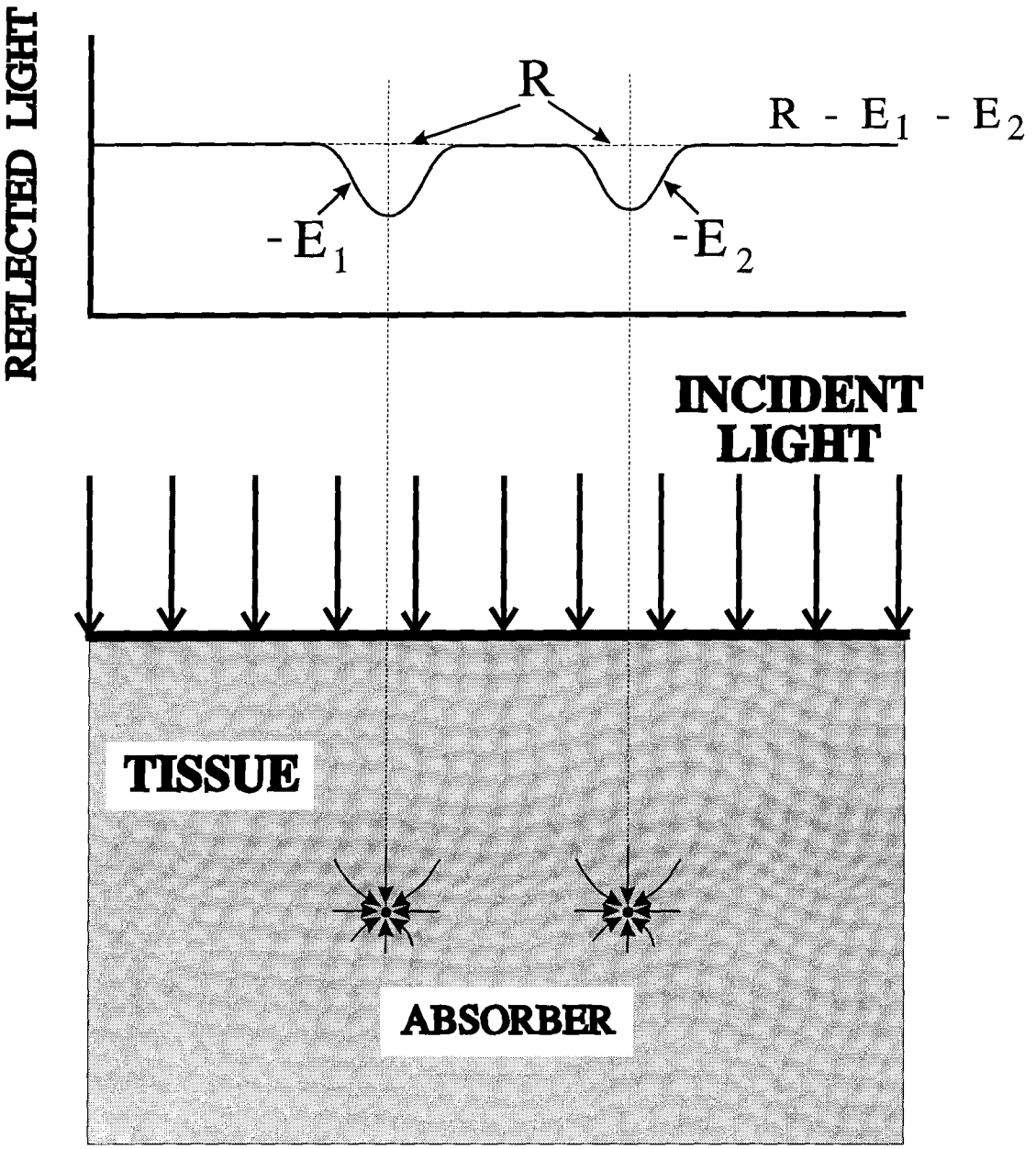

Figure 45. Schematic diagram of how to calculate the light distribution on the tissue surface when perfect absorbers are embedded inside the tissue, using the principle of superposition. The spatial resolution of diffuse reflectance image could be calculated from the R - E_1 - E_2 curve.

Monte Carlo simulation could again be used to calculate the escape function, E(x,y), of this point source. Imagine that a perfect absorber is put at the same point, all light comes to this point is absorbed. According to the principle of superposition, the light distribution on the tissue surface is now equal to R(x,y) - E(x,y). All these proposed computing procedures are shown in figure 45. Finally, the spatial resolution could be calculated from the R - E_1 - E_2 curve shown in figure 45. Comparing figures 43 and 45, one can see that the fluorescence signal is detected on a zero background, while the small absorption signal, -E(x,y), is detected on a larger background signal R(x,y). This clearly demonstrated that the fluorescence technique has much higher sensitivity than the reflectance (or transmittance) technique does.

Currently X-ray imaging and magnetic resonance imaging (MRI) are the two major physical diagnostic methods in clinical use. Other methods include ultrasound and positron emission tomography (PET) etc. (Profio, 1993). Examination of the underlying physical principles shows that, X-ray imaging only gives the element distribution in tissues. The high energy X-ray absorption by tissue is caused by striking out the inner shell electrons of an atom and therefore, is not sensitive to the chemical state (outer shell electronic states) of the molecules. The MRI exploits the nuclear spin to form an image of certain nuclide (i.e. ^1H) distribution in tissue. MRI is capable of deriving chemical information and has many advantages over X-ray. Optical diagnostic methods are

currently being intensively studied. The light absorption and fluorescence emission are determined by the outer shell electronic states of an atom in its compound. Therefore, using optical methods, we detect or image the chemical states of the biological tissue. We believe that in the future, optical spectroscopy and imaging will become complimentary methods of diagnoses to X-ray and MRI. They may be more powerful in detection of pre-malignant lesion or detection of a lesion in its early stage before the element re-distribution becomes visible under X-rays or MRI. Optical methods are also more suitable for surface lesion detection. For these future developments, the study of tissue optical properties will be rewarding.

CHAPTER 6: BIBLIOGRAPHY

Alfano, R.R., Tata, D.B., Cordero, J. Tomashefshy, P., Longo, F.W., and Alfano, M.A. Laser induced fluorescence spectroscopy from native cancerous and normal tissue. *IEEE J. Quantum Electronics,* **20**: 1507-1511, 1984.

Alfano, R.R., Tang, G.C., Pradhan, A., Lam, W., Choy, D.S.J., and Opher, E. Fluorescence spectra from cancerous and normal human breast and lung tissues. *IEEE J. Quantum Electronics,* **23**: 1806-1811, 1987.

Alfano, R.R., Tang, G.C., Pradhan, A., Bleich, M., Choy, D.S,J., and Opher, E. Steady state and time-resolved laser fluorescence from normal and tumor lung and breast tissues. *J. of Tumor Marker Oncology,* **3**: 165-174, 1988.

Anderson, R.R., Hu, J., and Parrish, J.A. Optical radiation transfer in human skin and applications in *in vivo* remittance spectroscopy. In *Proceedings of the Symposium on Bioengineering and the Skin, Cardiff, Wales, July 19-21, 1979*. London: MTP Press, Ltd., pp. 253-265, 1981.

Anderson, R.R. and Parrish, J.A. The optics of human skin. *J. of Invest. Dermatol.* **77**: 13-19, 1981.

Anderson, R.R. and Parrish, J.A. Optical properties of human skin. In *The Science of Photomedicine,* Regan, J.D. and Parrish, J.A. (eds), New York and London: Plenum Press, pp. 147-194, 1982.

Anderson, R.R. and Parrish, J.A. Selective photothermolysis: precise microsurgery by selective absorption of pulsed radiation. *Science,* **220**: 524-527, 1983.

Anderson, R.R. *In vivo* fluorescence of human skin. *Arch Dermatol,* **125**: 999, 1989.

Anderson, R.R., Beck, H., Bruggemann, U., Farinelli, W., Jacques, S.L., and Parrish, J.A. Pulsed photothermal radiometry in turbid media: internal reflection of backscattered radiation strongly influences optical dosimetry. *Appl. Opt.*, **28**: 2256-2262, 1989.

Anderson-Engels, S., Baert, L., D'Hallewin, M.A., Johansson, J., Stenram, U., Svanberg, K., and Svanberg, S. Fluorescence characteristics of atherosclerotic plaque and malignant tumors. *SPIE, Optical methods for tumor treatment and early diagnosis: mechanisms and techniques* **1426**: 31-43, 1991.

Archer, S.N. and Lythgoe, J.N. The visual pigment basis for cone polymorphism in the guppy, *poecilia reticulata.*, *Vision Res.*, **30**: 225-233, 1990.

Arndt, K.A., Noe, J.M., Rosen, S. (ed) *Cutaneous Laser Therapy: Principles and Methods*. Chichester: Johns Wiley & Sons, 1983.

Arnfield, M.R., Tulip, J., and McPhee, M.S. Optical propagation in tissue with anisotropic scattering. *IEEE Trans. Biomed. Eng.*, **35**: 372-381, 1988.

Atkins, J.T. Optical properties of turbid materials. In *The Biologic Effects of Ultraviolet Radiation (with Emphasis on the Skin)*. Urbach, F. eds. Oxford: Pergamon Press, pp. 141-150, 1969.

Ballowitz, L. and Avery, M.E. Spectral reflectance of the skin-studies on infant and adult humans, wistar and gunn rats. *Biol. Neonate*,**15**: 348-360, 1970.

Baraga, J.J., Rava, R.P., Fitzmaurice, M., Tony, L.L., Taroni, P., Kittrell, C., and Feld, M.S.: Characterization of the fluorescence morphological structures in human arterial wall using ultraviolet-excited microspectrofluorimetry. *Atherosclerosis* **88**:1-14, 1991.

Becker, R.S. *Theory and Interpretation of Fluorescence and Phosphorescence*. John Wiley & Sons, Inc., New York, 1969.

Bloom, M. The physics of soft, natural materials. *Physics in Canada* **48**: 7-16, 1992.

Bloom, M. and Mouritsen, O.G. The evolution of membranes. In *Biophysics Handbook on Membranes I: Structure and Conformation*. Lipowsky, R. and Sackmann, E. (eds), Elsevier Pub. Co., 1993 (in press).

Bolin, F.P., Preuss, L.E., Taylor, R.C., and Ference, R.J. Refractive index of some mammalian tissue using a fiber optic cladding method. *Appl. Opt.*, **28**: 2297-2303, 1989.

Bonner, R.F., Nossal, R., Havlin, S., and Weiss, G.H. Model for photon migration in turbid biological media. *J. Opt. Soc. Amer.*, **4**: 423-432, 1987.

Bowes, W.A., Corke, B.C., and Hulka, J. Pulse oximetry: a review of the theory, accuracy, and clinical applications. *Obstetrics & Gynecology,* **74**: 541-546, 1989.

Bowmaker, J.K., Astell, S., Hunt, D.M., and Mollon, J.D. Photosensitive and photostable pigments in the retinae of old world monkeys., *J. Exp. Biol.* **156**: 1-19, 1991.

Brinkman, R., Zijlstra, W.G., and Koopmans, R.K. A method for continuous observation of percentage oxygen saturation in patients. *Arch. Chir. Ned.*, **1**: 333, 1949.

Brinkman, R., Cost, W.S., Koopmans, R.K., and Zijlstra, W.G. Continuous observation of percentage oxygen saturation of capilary blood in patients. *Arch. Chir. Ned.*, **1**: 184, 1949.

Bruls, W.A.G. and van der Leun, J.C. Forward scattering properties of human epidermal layers. *Photochem. Photobiol.*, **40**: 231-242, 1984.

Bulnois, J.L. Photophysical processes in recent medical laser developments: A review. *Lasers Med.Sci.* **1**: 47-66, 1986.

Butler, J.P., Suzuki, S., Oldmixon, E.H., and Hoppin, F.S. A theory of diffuse light scattering by lungs. *J. Appl. Physiol.*, **58**: 89-96, 1985.

Caplan, R.M. Medical uses of the Wood's lamp. *JAMA*, **202**: 1035-1038, 1967.

Cascinelli, N., Ferrario, M., Tonelli, T., and Leo, E. A possible new tool for clinical diagnosis of melanoma: the computer. *J. Am. Acad. Dermatol.*, **16**: 361-367, 1987.

Cashwell, E.D. and Everett, C.J. *A Practical Manual on the Monte Carlo Methods for Random Walk Problems*. Pergmon Press, new York, 1959.

Casperson, T., Lomakka, G., and Rigler, R. Physikalisch - optische methoden in der histochemie. *Acta Histochem. Suppl.*, **6**: 21-33, 1965.

Chance, B. Comparison of time-resolved and -unresolved measurements of deoxyhemoglobin in brain. *Proc. Natl. Acad. Sci.*, **85**: 4971-4975, 1988.

Chance, B., Nioka, S., Kent, J., McCully, K., Fountain, M., Greenfeld, R., and Holtom, G. Time-resolved spectroscopy of hemoglobin and myoglobin in resting and ischemic muscle. *Anal. Biochem.*, **174**: 698-707, 1988.

Cheong, W.F., Prahl, S.A., and Welch, A.J. A review of the optical properties of biological tissues. *IEEE J. Quantum Electronics*, **26**: 2166-2184, 1990.

Chester, A.N., Martellucci,S., Scheggi, A.M. (ed) *Laser Systems for Photobiology and Photomedicine*. New York: Plenum Press, 1991.

Claridge, E., Hall, P.N., Keefe, M., and Allen, J.P. Shape analysis for classification of malignant melanoma. *J. Biomed. Eng.*, **14**: 229-234, 1992.

Clarke, R.H., Isner, J.M., Gauthier, T., Nakagawa, K., Cerio, F., Hanlon, E., Gaffney, E., Rouse, E., and DeJesus, S. Spectroscopic characterization of cardiovascular tissue. *Lasers in Surgery and Medicine* **8**: 45-89, 1988.

Cotheren, R.M., Richards-Kortum, R., Sivak, M.V., Fitzmaurice, M., Rava, R.P., Bayce, G.A., Doxtader, M., Blackman, R., Ivanc, T.B., Hayes, G.B., Feld, M.S., and Etras, R.E.: Gastrointestinal Tissue diagnosis by laser-induced fluorescence spectroscopy at endoscopy. *Gastrointestinal Endoscopy* **36**:105-111, 1990.

Crilly, R.J., Cheong, W.F., Motamedi, M., and Spears, J.R. Simulation of fluorescent measurements in a turbid media. *Laser Surg. Med.*, **Supplement 4**: 4, 1992.

Daniels, F. and Imbrie, J.D. Comparision between visual grading and reflectance measurements of erythema produced

by sunlight. *J. Investigative Dermatol.*, **30**: 295-304, 1957.

David, G.B. and Galbraith, W. The Denver universal microspectroradiometer (DUM). *J. Microscopy,* **103**: 135-178, 1975.

Dawson, J.B., Ellis, D.J., Grassam, E., Cotterill, J.A., Fisher, G.W., and Feather, J.W. A theoretical and experimental study of light absorption and scattering by *in vivo* skin. *Phys. Med. Biol.* **25**: 695-709, 1980.

Deckelbaum, L.I., Lam, J.K., Cabin, H.S., Clubb, K.S., and Long, M.B. Discrimination of normal and atherosclerotic aorta by laser- induced fluorescence. *Lasers in Surgery and Medicine* **7**:330-335, 1987.

Dhawan, A.P. and Sicsu, A. Sigmentation of images of skin lesions using color and texture information of surface pigmentation. *Computerized Medical Imaging and Graphics,* **16**: 163-177, 1992.

Diffey, B.L. Ultrviolet radiation physics and the skin. *Phys. Med. Biol.*, **25**: 405-426, 1980.

Diffey, B. Photobiology of the skin. *Phys. Bulletin,***35**: 69-72, 1984.

Duck, F.A. *Physical Properties of Tissue.* Academic Press, London and New York, 1990.

Edwards, E.D. and Duntley, S.Q. The pigments and color of living human skin. *The American J. of Anatomy,* **65**: 1-33, 1939.

Edwards, E.D., Finklestein, N.A., and Duntley, S.Q. Spectrophotometry of living human skin in the ultraviolet range. *J. Invest. Dermat.*,**16:** 311-321, 1951.

Everett, M.A., Yeargers, E., Sayre, R.M., and Olsen, R.L. Penetration of epidermis by ultraviolet rays. *Photochem. Photobiol.*, **5**: 533-542, 1966.

Farrel, T.J., Patterson, M.S., Wilson, B.C. A diffusion theory model of spatially resolved, steady-state diffuse

reflectance for the noninvasive determination of tissue optical properties *in vivo*. *Med. Phys.*, **19**:879-888, 1992.

Feather, J.W., Ryatt, K.S., Dawson, J.B., Cotterill, J.A. Barker, D.J., and Ellis, D.J. Reflectance spectrophotometric quantification of skin color changes induced by topical corticosteroid preparations. *Br. J. Dermatol.*, **106:** 437-444, 1982.

Feather, J.W., Ellis, D.J., and Leslie, G. A portable reflectrometer for rapid quantification of cutaneous hemoglobin and melanin. *Phys. Med. Biol.*, **33**: 711-722, 1988.

Feather, J.W., Hajizadeh-Saffar, M., Leslie, G., and Dawson, J.B. A portable scanning reflectance spectrophotometer using visible wavelength for the rapid measurement of skin pigments. *Phys. Med. Biol.*, **34**: 807-820, 1989.

Findlay, G.H. The measurement of epidermal melanin by reflectance. *Br. J. Dermatol.*, **78**: 528-530, 1966.

Findlay, G.H. Blue skin. *Br. J. Dermatol.*, **83**: 127-134, 1970.

Fitzmanrice, M., Bordagaray, T.O., Engelmann, G.L., Richards-Kortum, R., Kolubayev, T., Feld, M.S., Ratliff, N.B., and Kramer, J.R. Argon Ion Laser-excited autofluorescence in normal and atherosclerotic aorta and coronary arteries -- morphologic studies. *American Heart Journal* **118**:1028-1038, 1989.

Flock, S.T., Wilson, B.C., and Patterson, M.S. Hybrid Monte Carlo-diffusion theory modeling of light distribution in tissue. *SPIE Series* **908**: 20-28, 1988.

Flock, S.T., Wilson, B.C., and Patterson, M.S. Monte Carlo modeling of light propagation in highly scattering tissue. *IEEE Trans. Biomed. Eng.*, **30**: 1162-1173, 1989.

Frank, L., Rapp, Y., and Bergman, L.V. An instrument for the objective measurement of erythema. *J. Investigative Dermatol.*, **34**: 21-24, 1961.

Galbraith, W., Marshall, P.N., Lee, E.S., and Bacus, J.W. Studies on Papanicolaou staining. *Analytical and Quantitative Cytology*, **1**: 160-168, 1979.

Gardner, C.M. and Welch, A.J. Improvements in the accuracy and statistical variance of the Monte Carlo simulation of light distribution in tissue. *SPIE Proc.: Laser-Tissue Interaction III,* **1664**: 400-409, 1992.

Gardner, C.M., Jacques, S.L., and Welch, A.J. Fluorescence and reflectance spectra specify intrinsic fluorescence spectrum corrected for tisuue optics distortion. *SPIE Proc.*,**1885**, 1993 (in press).

Gilchrest, B.A., Fitzpatrick, T.B., Anderson, R.R., *et al*, Localization of melanin pigmentation with Wood's lamp. *Br. J. Dermatol.*, **96**: 245-248, 1977.

Goldman, L. (ed) *The Biomedical Laser*. New York: Springer Verlag, 1981.

Goldman, L. (ed) *Laser Non-Surgical Medicine.* Technomic Publishing Co. Inc. 1991.

Goldman, L. and Kerr, J.H. Laser biomedical subsurface imaging. *J. Laser Appl.*, **3**: 63-65, 1991.

Goldzieher, J.W., Roberts, I.S., Rawls, W.B., and Goldzieher, M.A. "Chemical" analysis of the intact skin by reflectance spectrophotometry. *Archives of Dermatology and Syphilology,* **64**: 533-548, 1951.

Golston, J.E., Stoecker, W.V., and Moss, R.H. Automatic detection of irregular borders in melanoma and other skin tumors. *Computerized Medical Imaging and Graphics,* **16**: 199-203, 1992.

Govardoviskii, V.I., Byzov, A.L., Zueva, L.V., Polisczuk, N.A., and Baburina, E.A. Spectral characteristics of photoreceptors and horizontal cells in the retina of the Siberia sturgeon *acipenser baeri* brandt. *Vision Res.* **31**: 2047-2056, 1991.

Graaff, R., Dassel, A.C.M., Koelink, M.H., de Mul, F.F.M., Aarnoudse, J.G., and Zijlstra, W.G. Optical properties of human dermis *in vitro* and *in vivo*. *Appl. Opt.*, **32**: 435-447, 1993.

Green, A., Martin, N. McKenzie, Pfitzner, J., Quintarelli, F., Thomas, B.W., O'Rourke, M., and Knight, N. Computer imaging analysis of pigmented skin lesions. *Melanoma Research,* **1**: 231-236, 1991.

Green, C., Diffey, B.L., and Hawk, J.L.M. Ultraviolet radiation in the treatment of skin disease. *Phys. Med. Biol.,* **37**: 1-20, 1992.

Groenhuis, R.A.J., Ferwerda, H.A., and Ten Bosch, J.J. Scattering and absorption of turbid materials determined from reflection measurements, 1: Theory. *Appl. Opt.,* **22**: 2456-2462, 1983.

Guilbault, G.G. *Practical Fluorescence - Theory, Methods, and Techniques*. Marcel Dekker, Inc., New York, 1973.

Gupta, B.D. and Williams, T.P. Lateral diffusion of visal pigments in toad (*Bufo marimus*) rods and in catfish (*Ictalurus punctatus*) cones. *J. Physiology* **430**: 483-496, 1990.

Halaby, S.A. and Vance, M.E. Computer controlled spectral measurements of blood cells. *IEEE Trans. Biomed. Eng.,* **BME-26**: 34-43, 1979.

Hannemann, R.E., Dewitt, D.P., and Wiechel, J.F. Neonatal serum bilirubin from skin reflectance. *Pediat. Res.,* **12**: 207-210, 1978.

Hardy, J.D., Hammel, H.T., and Murgatroyd, D. Spectral transmittance and reflectance of excised human skin. *J. Appl. Physiol.,***9**: 257-264, 1956.

Haselgrove, J., Leigh, J., Yee, C., Wang, N.G., Maris, M., and Chance, B. Monte Carlo and diffusion calculations of photon migration in non-infinite highly scattering media. *SPIE Proc.,* **1431**: 30-41, 1991.

Hebden, J.C. and Kruger, R.A. Transillumination imaging performance: spatial resolution simulation studies. *Med. Phys.,* **17**: 41-47, 1990.

Henyey, L.G. and Greenstein, J.L. Diffuse radiation in the galaxy. *Astrophys J.* **93**: 70-83, 1941.

Herbin, M., Venot, A., Devaux, J.Y., and Piette, C. Color quantitation through image processing in dermatology. *IEEE Trans. Medical Imaging,* **9**: 262- 269, 1990.

Hoerman, K.C. The optical properties of skin and its biomedical substituents. In *Biophysical Properties of the Skin*. Elden, H.R. Eds., John Wiley & Sons, Inc., New York, pp. 153-186, 1971.

Holick, M.F., MacLaughlin, Parrish, J.A., and Anderon, R.R. The photochemistry and photobiology of Vitamin D_3. in *The Science of Photomedicine*, Regan, J.D. and Parrish, J.A. (eds), Plenum Press, New York and London, pp 195-218, 1982.

Holmquist, J., Imasato, Y., Bengtsson, E., Olsem, B., and Stenkvist, B. A microspectrophotometric study of Papanicolaou-stained cervical cells as an aid in computerized image processing. *J. Histoochem. Cytochem.*, **24**: 1218-1224, 1976.

Hung, J., Lam, L., LeRiche, J.C., and Palcic, B. Autofluorescence of normal and malignant bronchial tissue. *Laser Surg. Med.*, **11**: 99-105, 1991.

Ishimaru, A. *Wave Propagation and Scattering in Random Media. Vol.1*.New York: Academic, 1978.

Jacques, S.L. and Prahl, S.A. Modeling optical and thermal distributions in tissue during laser irradiation. *Lasers in Surg. Med.*, **6**: 494-503, 1987.

Jacques, S.L., Alter, C.A., and Prahl, S.A. Angular dependence of He-Ne laser light scattering by human dermis. *Laser Life Sci.*, **1**: 309-333, 1987b.

Jacques, S.L. Simple theory, measurements, and rules of thumb for dosimetry during photodynamic therapy. *Proc. SPIE,* **1065**: 100-108, 1989.

Jacques, S.L. Time-resolved reflectance spectroscoopy in turbid tissue. *IEEE Trans. Biomed. Eng.*, **36**: 1155-1161, 1989b.

Jacques, S.L. and Keijzer, M. Dosimetry for lasers and light in dermatology — Monte Carlo simulation of 577 nm pulsed laser penetration into cutaneous vessels. *SPIE Series* **1422:** 2-13, 1991.

Jacques, S.L. The role of skin optics in diagnostic and therapeutic uses of lasers. In *Lasers in Dermatology,* Steiner, R., Kaufmann, R. Landthaler, M., and Braun-Falco, O. Eds., Springer-Verlag, Berlin, Heidelberg, pp. 1-21, 1991b.

Jacques, S.L. Laser-tissue interactions: photochemical, photothermal, and photomechanical. *Lasers in General surgery,* **72**: 531-558, 1992.

Jacques, S.L., Rastegar, S., Motamedi, M., Thomsen, S.L., Schwartz, J., Torres, J., and Mannonen, I. Liver photocoagulation with diode laser (805 nm) vs Nd:YAG laser (1064 nm). *SPIE Proc. Laser-Tissue Interaction III,* **1646**: 107-117, 1992b.

Jacques, S.L. *Optical Dosimetry and Tissue Optics*. SPIE Short Course, SC 7, Los Angeles, California, USA, January 1993.

Jacquez, J.A., Kuppenheim, H.F., Dimitroff, J.M., McKeehan, W., and Huss, J. Spectral reflectance of human skin in the region 235-700 mμ. *J. Appl. Physiol.*, **8**: 212-214, 1955.

Jacquez, J.A., Huss, J., McKeehan, W., Dimitroff, J.M., and Kuppenheim, H.F., Spectral reflectance of human skin in the region 0.7-2.6 μ. *J. Appl. Physiol.*, **8**: 297-299, 1955b.

Kapadia, C.R., Cutruzzola, F.W., O'Brien, K.M., Stetz, M.L., Enriquez, R., and Deckelbaum, L.I. Laser-induced fluorescence spectroscopy of human colonic mucosa - detection of adenomatous transformation. *Gastroenterology* **99**:150-157, 1990.

Karagiannes, J.L., Zhang, Z., Grossweiner, B., and Grossweiner, L.I. Applications of the 1-D diffusion approximation to the optics of tissues and tissue phantoms. *Appl. Opt.*, **28**: 2311-2317, 1989.

Keijzer, M., Star, W.M., and Storchi, R.M. Optical diffusion in layered media. *Appl. Opt.*, **27**: 1820-1824, 1988.

Keijzer, M., Jacques, S.L., Prahl, S.A., and Welch, A.J. Light distribution in artery tissue — Monte Carlo simulation for finite-diameter beams. *Lasers Surg. Med.*, **9**: 148-154, 1989.

Keijzer, M., Richards-Kortum, R., Jacques, S.L., and Feld, M.S. Fluorescence spectroscopy of turbid media: autofluorescence of the human aorta. *Appl. Opt.*, **28**: 4286-4292, 1989b.

Kenet, R.O., Kang, S., Kenet, B.J., Fitzpatrick, T.B., Sober, A.J., and Barnhill, R.L. Clinical diagnosis of pigmented lesions using digital epiluminescence microscopy. *Arch. Dermatol.*, **129**: 157-174, 1993.

Kittrell, C., Willett, R.L., de los Santos-Pacheo, C., Ratliff, N.B., Kramer, J.R., Malk, E.G., and Feld, M.S. Diagnosis of fibrous atherosclerosis using fluorescence. *Applied Optics* **24**:2280-2281, 1985.

Knowles, A. and Dartnall, H.J.A. The photobiology of vision. In *The Eye* **2B**, Davson, H. Eds., Academic, London, pp. 557-579, 1977.

Kochevar, I.E. Photobiology-basic science. *Dermatologic Clinics*,**4**: 171-179, 1986.

Kollias, N. and Baqer, A. An experimental study of the changes in pigmentation in human skin *in vivo* with visible and near infrared light. *Photochem. Photobiol.* **39**: 651-659, 1984.

Kollias, N. and Baqer, A. Spectroscopic characteristics of human melanin *in vivo*. *J. Investigative Dermatol.*, **85**: 38-42, 1985.

Kollias, N. and Baqer, A. On the assessment of melanin in human skin *in vivo*. *Photochem. Photobiol.* **43**: 47-54, 1986.

Kollias, N. and Baqer, A. Absorption mechanisms of human melanin in the visible, 400-720 nm. *J. Investigative Dermatol.*, **89**: 384-388, 1987.

Kollias, N. and Baqer, A. Quantitative assessment of UV-induced pigmentation and erythema. *Photodermatol.* **5**: 53-60, 1988.

Kollias, N., Baqer, A.H., and Sadiq, I. UVA and PUVA induced neomelanogenesis studied with diffuse reflectance spectroscopy. *Photochem. Photobiol.*, **49**: 16s, 1989.

Kollias, N., Gillies, R., and Anderson, R.R. Fluorescence spectra of human skin - preliminary report. (Abstract for the 1993 Annual Meeting of the Society for Investigative Dermatology, Washington, D.C., April, 1993) *J. Invest. Dermatol.*, **100**: 530, 1993

Kubelka, P. and Munk, F. Ein Beitrag zur Optik der Farbanstriche. *Z. technichse Physik* **12**: 593-601, 1931.

Kubelka, P. New contributions to the optics of intensely light-scattering materials. I. *J. Opt. Soc. Am.* **38:** 448-457, 1948.

Kubelka, P. New contributions to the optics of intensely light-scattering materials. II: Nonhomogeneous layers. *J. Opt. Soc. Am.* **44:** 330-335, 1954.

Kuppenheim, H.F. and Raymond, R.H. Spectral reflectance of white and negro skin between 440 and 1000 mμ. *J. Appl. Physiol.*,**4**: 800-806, 1952.

Labella, F.S. Cross-links in elastin and collagen. In *Biophysical Properties of the Skin.* Elden, H.R. Eds., John Wiley & Sons, Inc., New York, pp. 243-301, 1971.

Lakowicz, J.R. *Principles of Fluorescence Spectroscopy.* Plenum Press, New York and London, 1983.

Lakowicz, J.R., Berndt, K., and Johnson, M.L. Frequency- and time-domain measurements of photon migration in tissues. *Photochem. Photobiol.*, **49**:825, 1989.

Lam, S., MacAulay, C., and Palcic, B. Detection and localization of early lung cancer by imaging techniques. *Chest,* **103**: 12s-14s, 1993.

Leveque, J.L., Poelman, M.C., Legall, F., and de Rigal, J. New experimental approach to measure the skin-reflected light. application to cutaneous erythema and blanching. *Dermatologica,* **170**: 12-16, 1985.

Leffell, D.J., Stetz, M.L., Milstone, L.M., and Deckelbaum, L.I. *In vivo* fluorescence of human skin - a potential marker of photoaging. *Arch Dermatol*. **124**: 1514-1518, 1988.

Lohmann, W. and Paul, E. *In situ* detection of melanomas by fluorescence measurements. *Naturwissenschaften,* **75**: 201-202, 1988.

Lohmann, W., Nilles, M., and Bodeker, R.H. *In situ* differentiation between nevi and malignant melanomas by fluorescence measurements. *Naturwissenschaften,* **78**: 456-457, 1991.

Lomax, R.B., Daglish, A., Taylor, R.J., Gordon, M.T., and Robertson, W.R. Rapid continuous monitoring of enzyme activity in tissue sections: experience with the M85A and Zeiss UMSP-30 systems. *Histochemical Journal* **21**: 595-599, 1989.

Long, F.H., Nishioka, N.S., and Deustch, T.F. Measurement of the optical and thermal properties of biliary calculi using pulsed photothermal radiometry. *Lasers Surg. Med.,* **7**: 461-466, 1987.

Lucas, A., Radosavljevic, M.J., Lu, E., and Gaffney, E.J. Characterization of human coronary artery atherosclerotic plaque fluorescence emission. *Canadian J. of Cardiology* **6**:219-228, 1990.

MacLeod, J.S., Blanc, D., and Colles, M.J. Measurement of the optical absorption coefficients at 1.06 μm of various tissues using the photoacoustic effect. *Lasers Surg. Med.,* **8**: 143, 1988.

MacNichol, E.F. A photon counting microspectrophotometer for the study of single vertebrate photoreceptor cells. In *Frontiers in Visual Science,* Cool, S.J. and Smith E.L. Eds., Spring-Verlag, Berlin, pp.194-208, 1977.

Magnus, I.A. *Dermatological Photobiology*. Oxford: Blackwell Scientific Publications, 1976.

Marchesini, R., Brambilla, M., Clemente, C., Maniezzo, M., Sichirollo, A.E., Testori, A., Venturoli, D.R., and Cascinelli, N. *In vivo* spectrophotometric evaluation of neoplastic and non-neoplastic skin pigmented lesions — I. reflectance measurements. *Photochem. Photobiol.*, **53**: 77-84, 1991.

Marchesini, R., Cascinelli, N., Brambilla, M., Clemente, C., Mascheroni, L., Pignoli, E., Testori, A., and Venturoli, D.R. *In vivo* spectrophotometric evaluation of neoplastic and non-neoplastic skin pigmented lesions. II: discriminant analysis between nevus and melanoma. *Photochem. Photobiol.*, **55**: 515-522, 1992.

Marchesini, R., Clemente, C., Pignoli, E., and Brambilla, M. Optical propertiesof *in vitro* epidermis and their possible relationship with optical properties of *in vivo* skin. *J. Photochem. Photobiol. B: Biol.*, **16**: 127-140, 1992b.

Marijnissen, J.P.A. and Star, W.M. Phantom measurements for light dosimetry using isotropic and small aperture detectors. In *Porphyrin Localization and Treatment of Tumors,* Doiron, D.R. and Gomer, C.J., Eds. New York: Alan Liss, pp. 133-148, 1984.

Marijnissen, J.P.A., Star, M.W., van Delft, J.L., and Franken, N.A.P. Light intensity measurements in optical phantoms and *in vivo* during HPD-photoradiation treatment using a miniature light detector with isotropic response. In *Photodynamic Therapy of Tumors and Other Diseases,* Jori, G. and Perria, C., Eds. Padova: Libreria Progetto, pp. 387-390, 1985.

Marshall, R.J. Infrared and ultraviolet photography in a study of the selective absorption of radiation by pigmented lesions of skin. *Medical and Biological Illustration,* **26**: 71-84, 1976.

Marshall, R.J. Evaluation of a diagnostic test based on photographic photometry of infrared and ultraviolet radiation reflected by pigmented lesions of skin. *J. of Audiovisual Media in Medicine,* **3**: 94-98, 1980.

Marshall, R.J. Ultraviolet photography in detecting 'latent halos of pigmented lesions. *Audiovisual Media in Medicine,* **4**: 127-129, 1981.

Marshall, R.J. A television method for measuring infrared and ultraviolet reflectances of pigmented lesions. *Audiovisual Media in Medicine,* **5**: 51-55, 1982.

Martellucci, S. and Chester, A.N. (ed) *Laser Photobiology and Photomedicine*. New York and London: Plenum Press, 1985.

Mendelson, Y. and McGinn, M.J. Skin reflectance pulse oximetry: in vivo measurements from the forearm and calf. *J. Clinical Monitoring,* **7**: 7-12, 1991.

Mendelson, Y. and Yocum, B.L. Noninvasive measurement of arterial oxyhemoglobin saturation with a heated and a non-heated skin reflectance pulse oximeter sensor. *Biomedical Instrumentation & Technology,* **25**: 472-480, 1991.

Montagna, W., Kligman, A.M., Carlisle, K.S. *Atlas of Normal Human Skin*. New York: Springer-Verlag, 1992.

Montan, S. and Strombland, L.G.: Spectral characterization of brain tumors utilizing laser-induced fluorescence. *Lasers in the Life Sciences* **1**:275-285, 1987.

Moser, J.G., Ruck, A., Schwarzmaier, H.J., and Westphal-Frosch, C. Photodynamic cancer therapy: fluorescence localization and light absorption spectra of chlorophyll-derived photosensitizers inside cancer cells. *Opt. Eng.*,**31**: 1441-1446, 1992.

Moss, R.H., Stoecker, W.V., Lin, S.J., Muruganandhan, S., Chu, K.F., Poneleit, M., and Mitchell, C.D. Skin cancer recognition by computer vision. *Computerized Medical Imaging and Graphics,* **13**: 31-36, 1989.

Murray, A.E. A routine method for the quantification of physical change in melanocytic naevi using digital image processing. *J. of Audiovisual Media in medicine,* **11**: 52-57, 1988.

Nossal, R., Keifer, J., Weiss, G.H., Bonnar, R., Taitelbaum, H., and Havlin, S. Photon migration in layered media. *Appl. Opt.*, **27**: 3382-3391, 1988.

Nossal, N., Bonner, R.F., and Weiss, G.H. Influence of pathlength on remote optical sensing of properties of biological tissue. *Appl. Opt.*, **28**: 2238-2244, 1989.

Oraevsky, A.A., Letokhov, V.S., Ragimov, S.E., Omel' Yanenko, V.G., Belyaev, A.A., Shekhonin, B.V., and Akchurin, R.S. Spectral properties of human atherosclerotic blood vessel wall. *Lasers in Life Sciences* **2**:275-288, 1988.

Palcic, B., Lam, S., Hung, J., and MacAulay, C. Detection and localization of early lung cancer by imaging techniques. *Chest,* **99**: 742-743, 1991.

Parrish, J.A., Anderson, R.R., Urbach, F., and Pitts, D. *UV-A Biological Effects of Ultraviolet Radiation with Emphasis on Human Responses to Longwave Ultraviolet*. Chichester: John Wiley), 1978.

Parrish, J.A. and Wilson, B.C. Current and future trends in laser medicine. *Photochemistry and Photobiology,***53**: 731-738, 1991.

Patterson, M.S., Schwartz, E, and Wilson, B.C. Quantitative reflectance spectrophotometry for the noninvasive measurement of photosensitizer concentration in tissue during photodynamic therapy. *Proc. SPIE,* **1065**: 115-122, 1989.

Patterson, M.S., Chance, B., and Wilson, B.C. Time resolved reflectance and transmittance for noninvasive measurement of tissue optical properties. *Appl. Opt.*, **28**: 2331-2336, 1989b.

Patterson, M.S., Wilson, B.C., and Wyman, D.R. The propagation of optical radiation in tissue. I: Models of radiation transport and their application. *Laser Med. Sci.*, **6**:155-168, 1991.

Patterson, M.S., Wilson, B.C., and Wyman, D.R. The propagation of optical radiation in tissue. II: Optical properties of

tissues and resulting fluence distributions. *Laser Med. Sci.*, **6**: 379-390, 1991.

Perednia, D.A., White, R.G., and Schowengerdt, A. Localization of cutaneous lesions in digital images. *Computers and Biomedical research,* **22**: 374-392, 1989.

Perednia, D.A. What dermatologists should know about digital imaging. *J. Am. Acad. Dermatol.*, **25**: 89-108, 1991.

Perednia, D.A. and White, R.G. Automatic registration of multiple skin lesions by use of point pattern matching. *Computerized Medical Imaging and Graphics,* **16**: 205-216, 1992.

Peter, V.G., Wyman, D.R., Patterson, M.S., and Frank, G.L. Optical properties of normal and diseased human breast tissues in the visible and near infrared. *Phys. Med. Biol.*, **35**: 1317-1314, 1990.

Picton, W., Devitt, H., and Forgie, M.A. Practical applications of the Quantimet 720, an image analysing computer, in the field of investigative dermatology. *Br. J. Dermatol.*, **95**: 341-348, 1976.

Prahl, S.A., Keijzer, M., Jacques, S.L. and Welch, A.J. A Monte Carlo model of light propogation in tissue. In *Dosimetry of Laser Radiation in Medicine and Biology, SPIE Series* **IS 5**: 102-111, 1989.

Prahl, S.A., Vitkin, I.A., Bruggemann, U., Wilson, B.C., and Anderson, R.R. Determination of optical properties of turbid media using pulsed photothermal radiometry. *Phys. Med. Biol.*, **37**: 1203-1217, 1992.

Prahl, S.A., van Gemert, M.J.C., and Welch, A.J. Determining the optical properties of turbid media using the adding-doubling method. *Appl. Opt.*, **32**:559-568, 1993.

Profio, A.E. (ed) *Biomedical Engineering*. New York: John Wiley & Sons, Inc., 1993.

Regan, J.D. and Parrish, J.A. (ed) *The Science of Photomedicine*. New York and London: Plenum Press, 1982.

Richards-Kortum, R., Metha, A., Hayes, G., Cothren, R., Kolubayev, T., Kittrell, C., Ratliff, N.B., Kramer, J.R., and Feld, M.S. Spectral diagnosis of atherosclerosis using an optical fiber laser catheter. *American Heart Journal* **118**:381-391, 1989.

Richards-Kortum, R., R., Rava, Fitzmaurice, M., Tong, L., Ratliff, N.B., Kramer, J.R., and Feld, M.S. A one-layer model of laser induced fluorescence for diagnosis of diseases in human tissue: applications to human tissue. *IEEE Trans. Biomed. Eng.*, **36**: 1222-1232, 1989b.

Richards-Kortum, R., Rava, R.P., Petras, R.E., Fitzmaurice, M., Sivak, M., and Feld, M.S. Spectroscopic diagnosis of colonic dysplasia. *Photochemistry and Photobiology* **53**:777-786, 1991.

Richardson, J.H. *Handbook for the light microscope — a user's guide*. Noyes Publications, Park Ridge, New Jersey, pp. 291-293, 1991.

Rosen, C.F., Jacques, S.T., Stuart, M.E., and Gange, R.W. Immediate pigment darkening: visual and reflectance spectrophotometric analysis of action spectrum. *Photochem. Photobiol.*, **51**: 583-588, 1990.

Satori, M.P., Bossaller, C., Weilbacher, D., Henry, P.D., Roberts, R., Chin, B., Valderrama, J., and Berry, M.J. Detection of atherosclerotic plaques and characterization of arterial wall structure by laser-induced fluorescence. *Circulation* **74(Suppl II)**:II-7, 1986.

Satori, M., Weilbaecher, D., Valderrama, G.L., Kubodera, S., Chin, R.C., Berry, M.J., Tittel, F.K., Sauerbrey, R., and Henry, P.D. Laser-induced autofluorescence of human artery. *Circ. Res.* **63**:1053-1059, 1988.

Sayre, R.M. *The Influence of Ultraviolet Light on Skin*. Ph.D. Thesis, State University of New York at Buffalo, 1973.

Schneckenburger, H., Strauss, W., Ruck, A., Seidlitz, H.K., and Wessels, J.M. Microscopic fluorescence spectroscopy and diagnosis. *Opt. Eng.*, **31**: 995-999, 1992.

Schwarzmaier, H.J., Heintzen, M.P., Muller, W., Kaufmann, R., and Wolbarsht, M.L. Optical density of vascular tissue before and after 308 nm excimer laser irradiation. *Opt. Eng.*, **31**: 1436-1440, 1992.

Schomacker, K., Frisoli, J.K., Compton, C.C., Flotte, T.J., Richter, J.M., Nishioka, N.S., and Deutsch, T.F. Ultraviolet laser-induced fluorescence of colonic tissue -

basic biology and diagnostic potential. *Lasers in Surgery and Medicine* **12**:63-78, 1992.

Seidlitz, H.K., Stettmaier, K., Wessels, J.M., and Schneckenburger, H. Intracellular fluorescence polarization, picosecond kinetics, and light-induced reactions of photosensitizing porphyrins. *Opt. Eng.*, **31**: 1482-1486, 1992.

Solan, J.L. and Laden, K. Factors affecting the penetration of light through stratum corneum. *J. Soc. Cosmet Chem.*, **28**: 125-137, 1977.

Star, W.M., Marijnissen, J.P.A., Jansen, H., and van Gemert, M.J.C. Light dorsimetry: status and prospects. *J. Photochem. Photobiol.*, **B1**: 149-167, 1987.

Star, W.M., Marijnissen, P.A., and Van Gemert, M.J.C. Light dosimetry in optical phantoms and in tissues: I. multiple flux and transport theory. *Phys. Med. Biol.*, **33**: 437-454, 1988.

Steinke, J.M. and Shepherd, A.P. Diffusion model of the optical absorbance of whole blood. *J. Opt. Soc. Am. A*, **5**: 813-822, 1988.

Stoecker, W.V., Chiang, C.S., and Moss, R.H. Texture in skin images: comparision of three methods to determine smoothness. *Computerized Medical Imaging and Graphics*, **16**: 179-190, 1992.

Stoecker, W.V., Li, W.W., and Moss, R.H. Automatic detection of asymmetry in skin tumors. *Computerized Medical Imaging and Graphics*, **16**: 191-197, 1992.

Stoecker, W.V. and Moss, R.H. Editoral: digital imaging in dermatology. *Computerized Medical Imaging and Graphics*, **16**: 145-150, 1992.

Stone, J.L., Peterson, R.L., and Wolf, J.E. Digital imaging techniques in dermatology. *J. Am. Acad. Dermatol.*, **23**: 913-917, 1990.

Swairjo, M.A., Kollias, N., Baqer, A.H., and Sadiq, I. Modeling of UV induced erythema as measured by diffuse

reflectance spectroscopy. *Photochem. Photobiol.*, **49**: 16s, 1989.

Takatani, S., and Graham, M.D. Theoretical analysis of diffuse reflectance from a two-layer tissue model. *IEEE Trans. Biomed. Eng.*, **BME-26**: 656-664, 1979.

Tang, S. and Wan, S. The spectrophotometer and measurement of skin color. in *Cutaneous Laser Therapy: Principles and Methods*, Arndt, K.A., Noe, J.M., and Rosen, S. (eds), John Wiley & Sons Ltd, Chichester, New York, Brisbane, Toronto, and Singapore, pp.27-39, 1983.

Tang, G.C., Pradhan, A., and Alfano, R.R. Spectroscopic differences between human cancer and normal lung and breast tissues. *Lasers in Surgery and Medicine* **9**:290-295, 1989.

Tinet, E. and Avrillier, S. Monte Carlo modelisation of laser induced fluorescence signals in turbid media: determination of original fluorescence spectra. *SPIE Proc.*, **1887**, 1993 (in press).

Towne, B. and Huls, F.S. Generational change in skin color variation among Habbani Yemeni Jews. *Human Biol.* **62**: 85-100, 1990.

Tregear, R.T. *Physical Functions of Skin*. London: Academic, 1966.

Turner, J.N., Weir, B., and Collins, D.N. Standard specimens for stain calibration — application to Romanowsky-Giemsa staining. *Stain Technology* **65**: 55-67, 1990.

Umbaugh, S.E., Moss, R.H., and Stoecker, W.V. An automatic color segmentation algorithm with application to identification of skin tumor borders. *Computerized Medical Imaging and Graphics*, **16**: 227-235, 1992.

Urbach, F. (ed) *The Biologic Effects of Ultraviolet Radiation with Emphasis on the Skin*. Oxford: Pergamon, 1969

Van de Hulst, H.C. *Multiple Light Scattering: Tables, Formulas and Applications*. New York: Academic, 1980.

Van Gemert, M.J.C. and Star, W.M. Relations between the Kubelka-Munk and the transport equation models for anisotropic scattering. *Lasers in Life Sci.* **1**: 287-298, 1987.

Van Gemert, M.J.C., Welch, A.J., Star, W.M., Motamedi, M., and Cheong, W.F. Tissue optics for a slab geometry in the diffusion approximation. *Lasers in Med. Sci.*, **2**: 295-302, 1987.

Van Gemert, M.J.C., Schets, G.A.C.M., Bishop, M.S., Cheong, W.F., and Welch, A.J. Optics of tissue in a multi-layer slab geometry. *Lasers in Life Sci.*, **2**: 1-18, 1988.

Van Gemert, M.J.C., Jacques, S.L., Sterenborg, H.J.C.M., and Star, W.M. Skin optics. *IEEE Trans. Biomed. Eng.* **36**: 1146-1154, 1989.

Wan, S., Anderson, R.R., and Parrish, J.A. Analytical modeling for the optical properties of the skin with *in vitro* and *in vivo* applications. *Photochem. Photobiol.*, **34**: 493-499, 1981.

Wan, S., Jaenicke, K.F., and Parrish, J.A. Comparision of the erythemogenic effectiveness of ultraviolet B (290-320 nm) and ultraviolet A (320-400 nm) radiation by skin reflectance. *Photochem. Photobiol.*, **37**: 547-552, 1983.

Wang, L. and Jacques, S.L. *Monte Carlo Modeling of Light Transport in Multi-Layered Tissue in Standard C.* University of Texas M.D. Anderson Cancer Center, Houston, 1992.

Weatherall, I.L. and Coombs, B.D. Skin color measurements in terms of CIELAB color space values. *J. Investigative Dermatol.*, **99**: 468-473, 1992.

Wessels, J.M., Strauss, W., Seidlitz, H.K., Ruck, A., and Schneckenburger, H. Intracellular localization of mesotetraphenylporphyrine tetrasulfonate probed by time-resolved and microscopic fluorescence spectroscopy. *J. Photochem. Photobiol. B* **12**: 275-284, 1992.

White, R.G. and Perednia, D.A. Automatic derivation of initial match points for paired digital images of skin.

Computerized Medical Imaging and Graphics, **16**: 217-225, 1992.

Wied, G.L., Bahr, G.F., Oldfield, D.G., and Bartels, P.H. Computer assisted identification of cells from uterine adenocarcinoma. *Acta Cytologica* **13**: 21-26, 1969.

Wilksch, P.A., Jacka, F. and Blake, A.J. Studies of light propagation in tissue. In *Porphyrin localization and treatment of tumors*. Doiron, D.R. and Gomer, C.J. Eds. Alan R. Liss, New York, pp. 149-161, 1984.

Wilson, B.C. and Adam, G. A Monte Carlo model for the absorption and flux distribution of light in tissue. *Med. Phys*. **10**: 824-830, 1983.

Wilson, B.C. and Patterson, M.S. The physics of photodynamic therapy. *Phys. Med. Biol.*, **31**: 327-360, 1986.

Wilson, B.C., Patterson, M.S., Flock, S.T., and Wyman, D.R. Tissue optical properties in relation to light propagation models and in vivo dosimetry. In *Photon Migration in Tissues,* Chance, B. Eds. New York: Plenum, pp. 25-42, 1988.

Wilson, B.C., Park, Y., Hefetz, Y., Patterson, M.S., Madsen, S., and Jacques, S.L. The potential of time-resolved reflectance measurements for the noninvasive determination of tissue optical properties. *Proc. SPIE*, **1064**: 97-106, 1989.

Wilson, B.C. and Jacques, S.L. Optical reflectance and transmittance of tissue: principles and applications. *IEEE J. Quantum Electronics,* **26**: 2186-2198, 1990.

Wilson, B.C. Modeling and measurements of light propagation in tissue for diagnostic and therapeutic applications. In: *Laser Systems for Photobiology and Photomedicine,*Chester, A.N., Martellucci, S., and Scheggi, A.M. eds, Plenum Press, New York, pp. 13-27, 1991.

Witt, A.N. Multiple scattering in reflection nebulae I: A Monte Carlo approach. *The Astrophysical J. Suppl. Series* **35**: 1-6, 1977.

Wu, J., Partovi, F., Field, M.S., and Rava, R.P. Diffuse reflectance from turbid media: an analytical model of photon migration. *Appl. Opt.*, **32**: 1115-1121, 1993.

Wyman, D.R., Patterson, M.S. and Wilson, B.C. Similarity relations for anitrotropic scattering in Monte Carlo simulations of deeply penetrating neutral particles. *J. Comp. Phys.*, **81**: 137-150, 1989.

Yamanouchi, I., Yamauchi, Y., and Igarashi, I. Transcutaneous bilirubinometry: preliminary studies of noninvasive transcutaneous bilirubin meter in the Okayama National Hospital. *Pediatrics,* **65**: 195-202, 1980.

Yang,Y., Ye, Y., Li,F., Li, Y., and Ma, P. Characteristic autofluorescence for cancer diagnosis and its origin. *Laser in Surgery and Medicine* **7**:528-532, 1987.

Yoon, G., Welch, A.J., Motamedi, M., Van Gemert, M.C.J. Development and application of three-dimensional light distribution model for laser irradiated tissue. *IEEE J. Quantum Electronics,* **QE-23**: 1721-1733, 1987.

Yoon, G., Prahl, S.A., and Welch, A.J. Accuracies of the diffusion approximation and its similarity relations for laser irradiated biological media. *Appl. Opt.*, **28**: 2250-2254, 1989.

Zeng, H., MacAulay, C., Palcic, B., and McLean, D.I. A computerized autofluorescence and diffuse reflectance spectroanalyser system for *in vivo* skin studies. *Phys. Med. Biol.*, **38**: 231-240, 1993. Also presented at the *3rd Annual Western Canadian Society of Clinical and Investigative Dermatology, Jasper, Alberta,* Feb. 21-23, 1992.

Zeng, H., MacAulay, C., McLean, D.I., and Palcic, B. A novel microspectrophotometer and its biomedical application. *Opt. Eng.*, 1993b (in press).

Zeng, H., MacAulay, C., Palcic, B., and McLean, D.I. Autofluorescence distribution in skin tissue revealed by microspectrophotometer measurements. *SPIE Proc,* **1876B**, 1993c (in press).

Zeng, H., MacAulay, C., Palcic, B., and McLean, D.I. Laser induced changes in autofluorescence of *in vivo* skin. *SPIE Proc,* **1882**, 1993d (in press).

CHAPTER 7: APPENDIX

7.1 Monte Carlo simulation of light propagation in biological tissue[4]

7.1.1 Introduction

Monte Carlo simulation of photon propagation offer a flexible yet rigorous approach toward photon transport in turbid tissues. This method simulates the "random walk" of photons in a medium that contains absorption and scattering. The method is based on a set of rules that govern the movement of a photon in tissue. The key two decisions are (1) the mean free path for a scattering or absorption event, and (2) the scattering angle. Figure 46 illustrates a scattering event. In addition, at boundaries it must be decided if a photon is reflected or moves across the boundary. The rules for photon propagation are expressed as probability distributions for the incremental steps of photon movement between sites of photon-tissue interaction, for the angle of deflection in a photon's trajectory when a scattering event occurs, and for the probability of transmittance or reflectance at boundaries. Therefore, the method is rigorous yet very descriptive. However, the method is statistical in nature and relies on calculating the propagation of a large number of photons by a computer.

7.1.2 Sampling random variables

The Monte Carlo method, as its name implies ("throwing the dice"), relies on the random sampling of propagation variables from well defined probability distributions. Cashew and Everett (1955) provide a good reference for the principles of Monte Carlo modeling. Witt (1977) is also helpful with regard to calculating photon propagation.

Consider some random variable, x, which is needed by the Monte Carlo propagation equations. This variable may be a stepsize(s) which a photon will take between photon-tissue interaction sites, or an angle of deflection(θ) which the scattered photon may experience due to a scattering event.

---

[4] References used in preparing this section were Jacques, 1993 and Wang and Jacques, 1992.

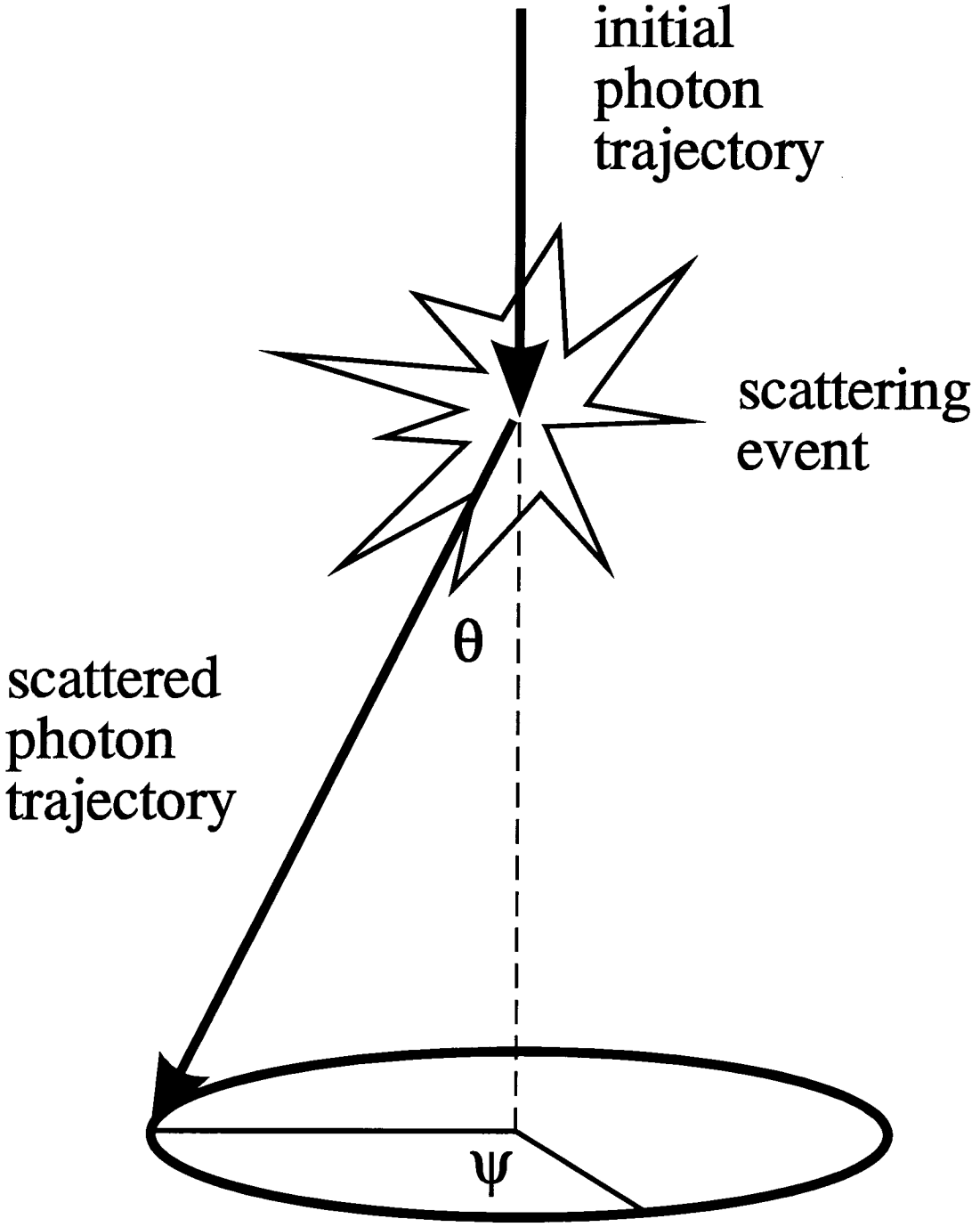

Figure 46. Deflection of a photon by a scattering event. The angle of deflection, θ, and the azimuthal angle, ψ, are indicated.

There is a probability density function, p(x), which defines the distribution of x over the interval $a \leq x \leq b$, such that:

$$\int_a^b p(x)dx = 1 \tag{35}$$

The probability that x will fall in the interval $[a,x_1]$, such that $a \leq x \leq x_1$, is given by the distribution function, $F_x(x)$, which is defined:

$$F_x(x_1) = \int_a^{x_1} p(x)dx \tag{36}$$

We wish to utilize the random number generator of the computer to generate a random variable, ζ, that will specify a unique choice of x that is consistent with the probability density function p(x). The probability density function for ζ is a constant, $p(\zeta) = 1$, within the interval [0,1]. The corresponding probability distribution, $F_\zeta(\zeta_1)$, is defined:

$$F_\zeta(\zeta_1) = \int_0^{\zeta_1} p(\zeta)d\zeta = \zeta_1 \tag{37}$$

These four functions, p(x), $F_x(x_1)$, $p(\zeta)$, and $F_\zeta(\zeta_1)$, are illustrated in Figure 47.

The key to the Monte Carlo selection of x using ζ is to equate the probability that ζ is in the interval $[0,\zeta_1]$ with the probability that x is in the interval $[a,x_1]$. In figure 47, we are equating the shaded area depicting the integral of p(x) over $[0,x_1]$ with the area depicting the integral $p(\zeta)$ over $[0,\zeta_1]$. Keep in mind that the total areas under the curves p(x) and $p(\zeta)$ each equal unity, as is appropriate for probability density functions. The results is a one-to-one mapping between the upper boundaries ζ_1 and x_1 based on the equality of the shaded areas in figure 47. In other words, we have equated $F_x(x_1)$ with $F_\zeta(\zeta_1)$. For generality, we replace the variables, ζ_1 and x_1, by continuous variables ζ and x:

$$F_\zeta(\zeta) = F_x(x) \tag{38}$$

or

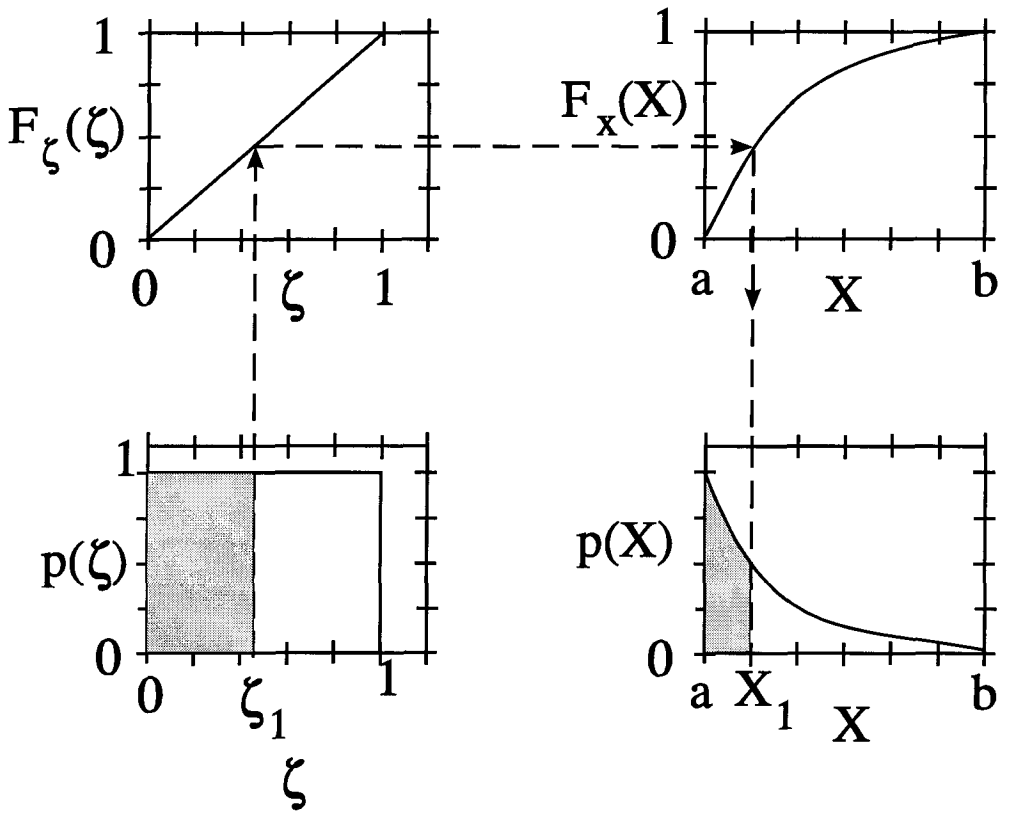

Figure 47. Sampling of random variables using a random number ζ. The probability density function, $p(\zeta)$, maps onto the probability density function, $p(x)$, via the distribution functions, $F_\zeta(\zeta)$ and $F_x(x)$. The shaded areas under the $p(\zeta)$ and $p(x)$ curves are equal.

$$\zeta = \int_a^x p(x)dx \tag{39}$$

where ζ is a random number between [0,1]. Eq.(39) is the basic equation for sampling a non-uniformly distributed p(x) based on a randomly generated variable ζ. To illustrate the use of Eq.(39), the following sections describe the selection of stepsize, s, the deflection angle, θ, and the azimuthal angle, ψ.

Selecting stepsizes, s

The stepsize of the photon is calculated based on the sampling of the probability for the photon's free path, $s \in [0, \infty]$. According to Beer's law of photon attenuation, the probability, P, of a photon interaction with the medium in the interval $[s_1, s_1 + ds_1]$ is:

$$-\frac{dP\{s \geq s_1\}}{ds_1} = (\mu_a + \mu_s)P\{s \geq s_1\} = \mu_t P\{s \geq s_1\} \tag{40}$$

where μ_a is the absorption coefficient, μ_s is the scattering coefficient, and μ_t is the total attenuation coefficient equal to $\mu_a + \mu_s$. All units are in cm^{-1}. Integration of Eq.(40) over the range $[0, s_1]$ leads to an exponential distribution:

$$P\{s \geq s_1\} = \exp(-\mu_t s_1) \tag{41}$$

Eq.(41) can be rearranged to yield the cumulative distribution function of the free path s:

$$P\{s < s_1\} = 1 - \exp(-\mu_t s_1) \tag{42}$$

The probability density function, $p(s_1)$, for the free path s is then expressed:

$$p(s_1) = \frac{dP\{s < s_1\}}{ds_1} = \mu_t \exp(-\mu_t s_1) \tag{43}$$

Now we apply Eq.(39):

$$\zeta = \int_0^s p(s)ds = \int_0^s \mu_t \exp(-\mu_t s)ds$$
$$= 1 - \exp(-\mu_t s) \tag{44}$$

The right-hand sides of both Eqs.(44) and (42) are the same and the reader may wonder why we have gone in a logical circle. Our motive was to first establish p(s) then apply Eq.(39), which is the general procedure we shall follow for routinely establishing how to randomly select variables. Rearranging Eq.(44):

$$\exp(-\mu_t s) = 1 - \zeta \tag{45}$$

Solving for s:

$$s = \frac{-\ln(1 - \zeta)}{\mu_t} \tag{46}$$

Since $-\ln(1-\zeta)$ is equivalent to $-\ln(\zeta)$ when ζ is a random variable in [0,1], Eq.(46) can be restated:

$$s = \frac{-\ln(\zeta)}{\mu_t} \tag{47}$$

Selecting deflection angle, θ

When a photon is scattered, the photon trajectory is deflected by an angle θ in the interval $[0,\pi]$. The probability density function that Henyey and Greenstein (1941) originally proposed for galactic light scattering approximates Mie scattering by particles comparable in size to the wavelengths of light, and is given:

$$p(\cos\theta) = \frac{1 - g^2}{2(1 + g^2 - 2g\cos\theta)^{3/2}} \tag{48}$$

The parameter g is called the anisotropy factor and characterizes the angular distribution of scattering. It is convenient to substitute the variable μ for the factor $\cos\theta$, such that μ is distributed in the interval [-1,1]. This

density function, $p(\mu)$, as proposed by Henyey and Greenstein, is interesting because the following identity holds:

$$g = \int p(\mu)\mu \, d\mu = \langle \mu \rangle \tag{49}$$

which equals the expectation value $\langle\mu\rangle$, or $\langle\cos\theta\rangle$, and defines g. Therefore, g characterizes the average amount of scattering in a medium (Eq.(49)), but also specifies the shape of the scattering function (Eq.(48)). The anisotropy, g, has a value between -1 and 1. A value of 0 indicates isotropic scattering and a value near 1 indicates very forward-directed scattering. Jacques *et al* (1987b) determined experimentally that the Henyey-Greenstein function adequately describes the probability density function of scattering in the tissue (dermis). Values for g range between 0.3 to 0.98 for tissues, but quite often g is ~0.9 in the visible spectrum.

Applying Eq.(39):

$$\zeta = \int_{-1}^{\mu} p(\mu)d\mu = \int_{-1}^{\mu} \frac{1 - g^2}{2(1 + g^2 - 2g\mu)^{3/2}} \cdot d\mu \tag{50}$$

Solving for μ (Prahl *et al*, 1989):

$$\mu = \frac{1}{2g}\left\{1 + g^2 - \left[\frac{1 - g^2}{1 - g + 2g\zeta}\right]^2\right\} \tag{51}$$

As g approaches zero, Eq. (51) becomes undefined. But in that limit, scattering becomes isotropic and the probability density function of Eq.(48) becomes $p(\mu) = 1/2$. Applying Eq.(39):

$$\zeta = \int_{-1}^{\mu} \frac{1}{2} \cdot d\mu = \frac{1}{2}(\mu + 1) \tag{52}$$

Solving for μ:

$$\mu = 2\zeta - 1 \tag{53}$$

Selecting azimuthal angle, ψ

When a photon is deflected by an angle θ, we assume that the photon deflects symmetrically about the initial axis of

propagation at an azimuthal ψ that is uniformly distributed within the interval $[0,2\pi]$. We here ignore asymmetric scattering. The probability density function, $p(\psi)$, is constant and equals $1/2\pi$. Applying Eq.(39):

$$\zeta = \int_0^{\psi} \frac{1}{2\pi} \cdot d\psi = \frac{\psi}{2\pi} \tag{54}$$

Solving for ψ:

$$\psi = 2\pi\zeta \tag{55}$$

7.1.3. Rules for photon propagation

This section presents the equations that describe photon propagation in the Monte Carlo model as applied to tissues. The treatment draws principally from Prahl *et al*, 1989. Figure 48 indicates the basic flowchart for one implementation of a Monte Carlo calculation.

Conventions used in following discussions

The details of the grid element organization for accumulating data will be delayed for later discussion in section 7.1.4. Throughout this section, the "equations" will often utilize an arrow ($\leftarrow$) to indicate the assignment of a new parameter value, a convention similar to the assignment of values in a computer programming statement.

Launching the photon

Each photon is initially assigned a weight, W, equal to unity. The photon is injected orthogonally into the tissue at the origin, which corresponds to a collimated ray of incident photons. Alternative photon sources are discussed in section 7.1.5.

When the photon is launched, if there is a mismatched boundary at the tissue surface, then some specular reflectance will occur. If the refractive indices of the outside medium and tissue are n_1 and n_2, respectively, then the specular reflectance, R_{sp}, is specified:

Figure 48. A simplified flow diagram for the Monte Carlo simulation of photon propagation. The photon is initialized with a weight of unity. The distance of the photon's step to the first interaction event is found, and the photon is moved. If the photon has left the tissue, the possibility of internal reflectance is checked. If the photon is internally reflected then the photon position is adjusted accordingly and the program continues, otherwise the photon escapes and the event is recorded as observable reflectance (or transmittance). With each step, the photon's weight is decremented. The fraction of lost weight is added to the local element of an array associated with the position of the photon that indicates photon energy absorbed by the tissue. The remaining photon weight is then scattered statistically to achieve a new direction, and a new step is calculated. If the photon weight falls below a threshold minimum value, then roulette is played to either extinguish the photon or continue propagation the photon. (Prahl *et al*, 1989).

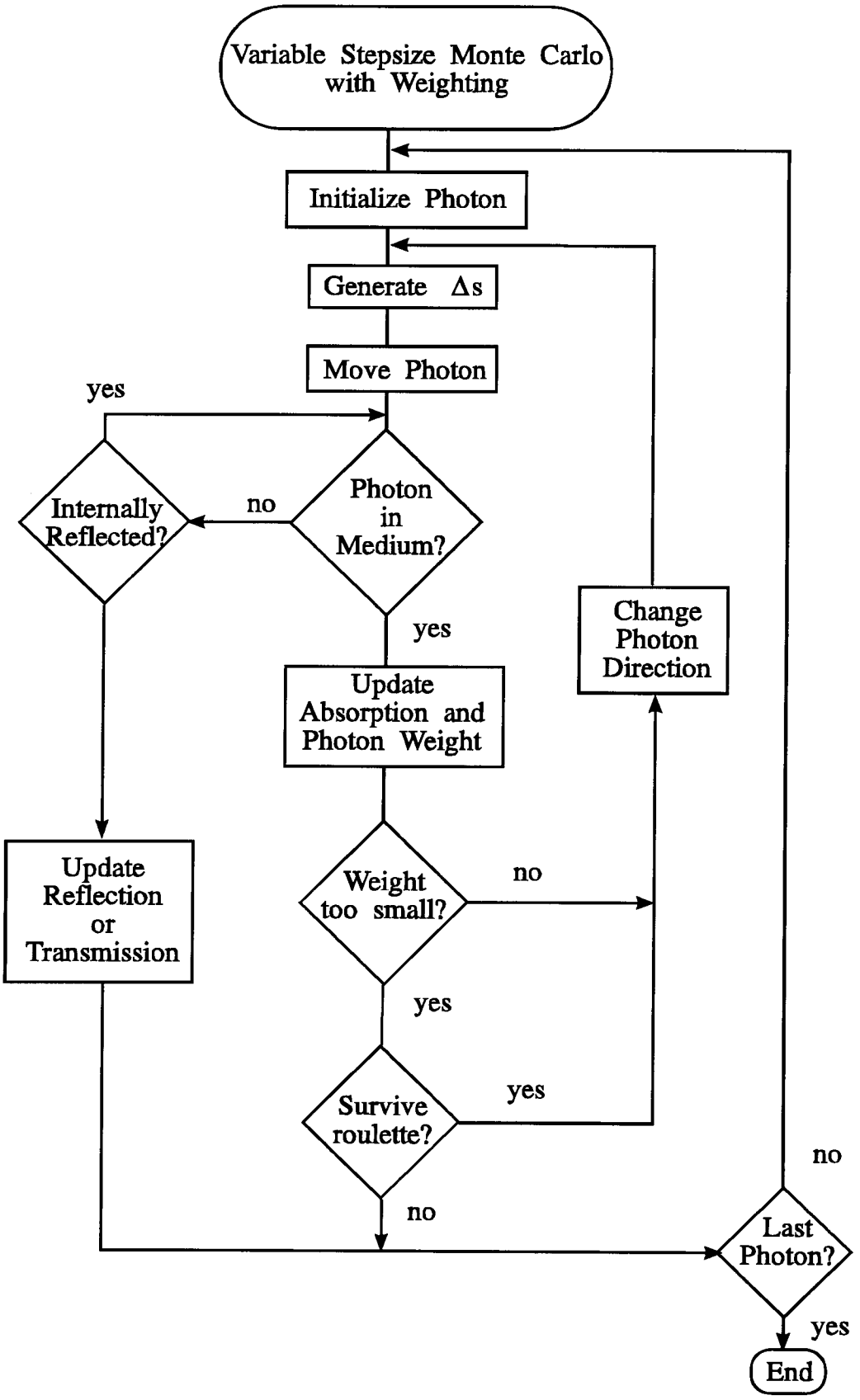
Variable Stepsize Monte Carlo with Weighting
Initialize Photon
Generate Δs
Move Photon
yes
Internally Reflected?
no
Photon in Medium?
yes
Change Photon Direction
Update Absorption and Photon Weight
Update Reflection or Transmission
Weight too small?
no
yes
Survive roulette?
yes
no
no
Last Photon?
yes
End

$$R_{sp} = \frac{(n_1 - n_2)^2}{(n_1 + n_2)^2} \tag{56}$$

The photon weight is decremented by R_{sp}:

$$W = 1 - R_{sp} \tag{57}$$

The specular reflectance is stored as the parameter R_{sp}, and is used when considering total reflectance in contrast to diffuse reflectance. Subsequent discussion of reflectance refers to the diffuse reflectance due to photons that entered the tissue and later escaped.

Photon's stepsize, s

The stepsize of the photon, s, is calculated based on a random sampling of the probability density function for s. The computer's random number generator yields a random variable, ζ, in the interval [0,1]. As before using Eq.(47), the sampling of s is given:

$$s = \frac{-\ln \zeta}{\mu_t} \tag{58}$$

where $\mu_t = \mu_a + \mu_s$. The mean free path between photon-tissue interaction sites is $1/\mu_t$. In turbid tissues at visible and near-infrared wavelengths, μ_s is typically about 100 times greater than μ_a and the scattering coefficient dominates the prediction of s.

Moving the photon

Once s is specified, the photon is ready to be moved in the tissue. The current position of the photon is specified by (x,y,z). The current trajectory of the photon is specified by a unit vector, $\mathbf{r}$, which is characterized by the direction cosines (μ_x, μ_y, μ_z), following Witt (1977):

$$\begin{aligned} \mu_x &= \boldsymbol{r} \bullet \boldsymbol{x} \\ \mu_y &= \boldsymbol{r} \bullet \boldsymbol{y} \\ \mu_z &= \boldsymbol{r} \bullet \boldsymbol{z} \end{aligned} \tag{59}$$

where **x**, **y**, and **z** are unit vectors along each axis. Initially at launching, the photon position is (0,0,0) and the trajectory is (0,0,1). The new position of the photon is specified by (x',y',z'), and is calculated:

$$\begin{aligned} x' &= x + \mu_x s \\ y' &= y + \mu_y s \\ z' &= z + \mu_z s \end{aligned} \tag{60}$$

The simplicity of Eq.(60) is a major reason for using Cartesian coordinates.

Internal reflectance or escape

During a step, the photon may cross a boundary. For example, the photon may attempt to escape the tissue at the air/tissue interface. If this is the case, then the photon may either escape as observed reflectance (or transmittance if a rear boundary is also included) or be internally reflected by the interface. The probability of a photon being internally reflected depends on the angle of incidence, θ_i, onto the boundary, where $\theta_i = 0$ implies orthogonal incidence. The value of θ_i is calculated:

$$\theta_i = \begin{cases} \cos^{-1}(\mu_z) & \text{if } \mu_z \geq 0 \\ \pi - \cos^{-1}(\mu_z) & \text{if } \mu_z < 0 \end{cases} \tag{61}$$

Snell's law indicates the relationship between the angle of incidence, θ_i, the angle of transmittance, θ_t, and the refractive indices of the media from which the photon is incident, n_i, and transmitted, n_t:

$$n_i \sin\theta_i = n_t \sin\theta_t \tag{62}$$

The internal reflectance, $R(\theta_i)$ is calculated by Fresnel's law:

$$R(\theta_i) = \frac{1}{2}\left[\frac{\sin^2(\theta_i - \theta_t)}{\sin^2(\theta_i + \theta_t)} + \frac{\tan^2(\theta_i - \theta_t)}{\tan^2(\theta_i + \theta_t)}\right] \tag{63}$$

A fraction, $1\text{-}R_i(\theta)$, of the current photon weight successfully escapes the tissue as observable reflectance, and increments the local reflectance array:

$$R(x', y') \leftarrow R(x', y') + (1 - R_i(\theta))W \tag{64}$$

The primed coordinates, x' and y', are used to emphasize that (x',y') refers to the position of escape, not the position of the photon. Only a fraction of the step s was taken by the photon before it successfully escaped. The actual position of escape must be calculated based on the value of this foreshortened stepsize, s', which is calculated as:

$$\begin{aligned} s' &= \frac{z}{\mu_z} && \text{if } z \le 0 \\ s' &= \frac{z - \tau}{\mu_z} && \text{if } z \ge \tau \end{aligned} \tag{65}$$

Eq.(60) is then used, substituting s' for s, to calculate the position of escape, (x',y').

A fraction $R_i(\theta)$ of the current photon weight is internally reflected. The new photon weight is calculated:

$$W \leftarrow R_i(\theta)W \tag{66}$$

The photon also has a new position and trajectory. The x and y coordinates of the position do not change; only the z coordinate has to be changed:

$$\begin{aligned} z &\leftarrow -z && \text{if } z \le 0 \quad \text{(outside slab at top surface)} \\ z &\leftarrow 2\tau - z && \text{if } z \ge \tau \quad \text{(outside slab at bottom surface)} \end{aligned} \tag{67}$$

where τ is the thickness of the tissue slab. The geometry of this calculation is illustrated in Figure 49. The new trajectory simply reverses the z-component of the trajectory:

$$\mu_z \leftarrow -\mu_z \tag{68}$$

Photon absorption

Once the photon has taken a step, some attenuation of the photon weight due to the absorption by the tissue must be calculated. A fraction of the photon's current weight, W, will be deposited in the local grid element (grid elements will be discussed later). The amount of deposited photon weight, ΔQ, is calculated:

$$\Delta Q = W \frac{\mu_a}{\mu_t} \tag{69}$$

The current value, Q(x,y,z), for the total accumulated photon weight previously deposited in the local grid element (x,y,z) is updated:

$$Q(x,y,z) \leftarrow Q(x,y,z) + \Delta Q \tag{70}$$

The new photon weight, W, is calculated:

$$W \leftarrow W \frac{\mu_s}{\mu_t} \tag{71}$$

Note that $(\mu_a/\mu_t + \mu_s/\mu_t)$ equals unity, so energy is conserved.

Terminating a photon

If the photon weight, W, has been sufficiently decremented such that it falls below a threshold value (e.g., $W_{threshold}$ = 0.001), then further propagation of the photon yields little information. However, proper termination must be executed to ensure conservation of energy without skewing the distribution of photon deposition. A technique called roulette is used to terminate the photon when $W \leq W_{threshold}$. The roulette technique gives the photon one chance in m (e.g. m = 10) of surviving with a weight of m·W. Otherwise, the photon weight is reduced to zero and the photon is terminated. A random number, ζ, in the interval [0,1] is generated by the computer. The photon weight is updated according to the following decision:

$$\begin{aligned} &\text{if } \zeta \leq 1/m \text{ then } W \leftarrow m \cdot W \\ &\text{if } \zeta > 1/m \text{ then } W = 0 \end{aligned} \tag{72}$$

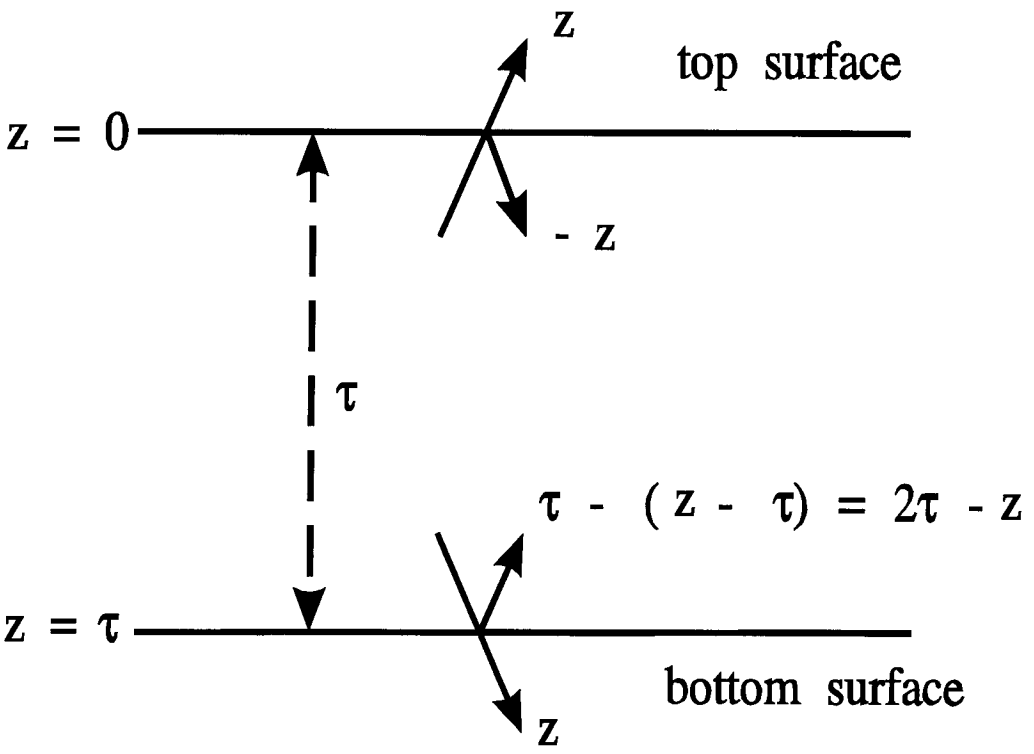

Figure 49. Total internal reflectance. When a photon is totally internally reflected, the z coordinate of the photon is changed from its would-be position outside the tissue to a position within the tissue.

This method conserves energy and eventually terminates photons in an unbiased manner.

Scattering the photon

Once the photon has been moved and its weight decremented, the photon is ready to be scattered. A random number ζ is generated. The selection of the deflection angle, θ, is accomplished in terms of the $\cos\theta$ or μ as previously discussed in Eqs.(51) and (53):

$$\mu = \begin{cases} \dfrac{1}{2g}\left\{1 + g^2 - \left[\dfrac{1 - g^2}{1 - g + 2g\zeta}\right]^2\right\} & \text{if } g > 0 \\ 2\zeta - 1 & \text{if } g = 0 \end{cases} \tag{73}$$

The photon deflection θ equals $\cos^{-1}(\mu)$.

The azimuthal angle, ψ, is calculated as previously discussed in Eq.(55). The selection of ψ is based on a random number, ζ:

$$\psi = 2\pi\zeta \tag{74}$$

Once the deflection and azimuthal angles are calculated, the new trajectory of the photon (μ'_x, μ'_y, μ'_z) is calculated from the old trajectory (μ_x, μ_y, μ_z) and the deflection angles θ and ψ (Prahl *et al*, 1989, Witt, 1977):

$$\begin{aligned} \mu'_x &= \frac{\sin\theta}{\sqrt{1 - \mu_z^2}}(\mu_x\mu_z\cos\psi - \mu_y\sin\psi) + \mu_x\cos\theta \\ \mu'_y &= \frac{\sin\theta}{\sqrt{1 - \mu_z^2}}(\mu_y\mu_z\cos\psi - \mu_x\sin\psi) + \mu_y\cos\theta \\ \mu'_z &= -\sin\theta\cos\psi\sqrt{1 - \mu_z^2}\cdot(\mu_y\mu_z\cos\psi - \mu_x\sin\psi) + \mu_z\cos\theta \end{aligned} \tag{75}$$

If the angle is too close to normal (i.e. $|\mu_z| > 0.99999$) then the following formulas should be used (Prahl *et al*, 1989):

$$\begin{aligned} \mu'_x &= \sin\theta\cos\psi \\ \mu'_y &= \sin\theta\sin\psi \\ \mu'_z &= \mu_z\cos\theta \,/\, |\mu_z| \end{aligned} \tag{76}$$

Multi-layered tissues

This is the appropriate point to mention multi-layered tissue models. Different tissue layers may have different optical properties and refractive indices. A brief discussion of how to treat such internal boundaries is presented here. Consider a photon which attempts to make a step of s within tissue 1 with μ_{a1}, μ_{s1}, n_1, but crosses a boundary into tissue 2 with μ_{a2}, μ_{s2}, n_2 after a foreshortened step s_1. The first question asked is whether or not the photon is reflected by the refractive index mismatch, which depends on the angle of incidence onto the boundary and the refractive indices, n_1 and n_2. The problem is handled in a manner similar to the above treatment of internal reflectance to yield a value for $R(\theta_i)$ using Eqs. (61)-(63). To determine whether or not the photon is reflected by the boundary or transmits into tissue 2, a random number, ζ, is generated:

$$\begin{aligned} &\text{if } \zeta \le R(\theta_i) \text{ then photon is reflected} \\ &\text{if } \zeta > R(\theta_i) \text{ then photon is transmitted} \end{aligned} \tag{77}$$

If the photon is reflected, then the position and trajectory are simply updated appropriately. But if the photon is transmitted into tissue 2, then the following procedure is followed. The photon has traveled a foreshortened step size s_1 within tissue 1, which corresponds to a distance of $s_1\mu_{t1}$ in dimensionless units of optical depth. The photon still intends to travel a further distance of $(s-s_1)\mu_{t1}$. But this additional distance will take place in tissue 2. Therefore, the remaining stepsize, s_2, in tissue 2 is specified:

$$s_2 = \frac{(s - s_1)\mu_{t1}}{\mu_{t2}} \tag{78}$$

Eq.(60) is used, substituting s_1 for s, to calculate the foreshortened step within tissue 1. Then Eq.(60) is again applied, substituting s_2 for s, to complete the step in tissue

2. This approach is relatively simple. Of course, we are not mentioning the hardest task, which is developing efficient code that manages the geometry of tissue structures and detects boundary crossings.

7.1.4 The data

The basic idea

The basic strategy of this implementation of the Monte Carlo method is to record the accumulated photon energy density, Q, in J/cm^3 that is deposited in a local tissue volume. The local light fluence, Φ, in J/cm^2 is calculated using the local absorption coefficient, μ_a, in cm^{-1}:

$$\Phi = \frac{Q}{\mu_a} \tag{79}$$

The grid elements

The propagation of photons according to the equations in section 7.1.3 is conducted using Cartesian coordinates. A choice must still be made regarding how to store photon deposition. One must choose an array to serve as the grid element system for data acquisition of the internal distribution of Q.

Since many of our problems are symmetric around the central z-axis, we have chosen a grid system in cylindrical coordinates to minimize the computer memory space required. A cylindrical coordinate system requires two variables (r,z), whereas a Cartesian coordinate system requires three variables (x,y,z). Also, we have chosen equally spaced grids because the resulting plots of isofluence contours are smooth at positions distant from the source at the origin. In contrast, logarithmically scaled grid sizes offer better resolution near the source but poorer resolution at distant points. But these choices are somewhat arbitrary.

Let us organize the grid in cylindrical coordinates as an array Q[i,j] which corresponds to the accumulated energy deposition, Q(r,z), in units of photon weight. Photon propagation is conducted in Cartesian coordinates of x, y, and

z, as discussed previously. Energy deposition is stored in cylindrical coordinates of r and z. The coordinate r is given:

$$r = \sqrt{x^2 + y^2} \tag{80}$$

Which always yields a positive value for r. All values of z are positive within the tissue slab. The grid element [i,j] corresponds to the position (r,z) such that:

$$\begin{aligned} idr \le r &< (i+1)dr \\ jdz \le z &< (j+1)dz \end{aligned} \tag{81}$$

If the computer language offers an INTEGER function that rounds off 2.49 to 2 and 2.51 to 3, then the following assignment statements can be used:

$$\begin{aligned} i &= INTEGER\left(\frac{r}{dr} - 0.5\right) \\ j &= INTEGER\left(\frac{z}{dz} - 0.5\right) \end{aligned} \tag{82}$$

and INTEGER of a negative number equals zero.

The volume, dV, of the volume element corresponding to [i,j] is calculated:

$$\begin{aligned} dV &= \int_{idr}^{(i+1)dr} 2\pi r dr dz \\ &= \pi(((i+1)dr)^2 - (idr)^2)dz \\ &= (2i+1)\pi dr^2 dz \end{aligned} \tag{83}$$

Note that in this cylindrical system, each volume element corresponds to an annular ring whose diameter is ~ r, thickness is dr, and depth is dz.

Converting the raw data to Q and Φ

After completing a Monte Carlo simulation involving N photons (e.g. N = 1,000,000), the accumulated deposited photon weight is stored in grid elements Q[i,j] in units of photon weight. This raw data is converted into energy density,

Q[i,j], in units of J/cm³ by assuming that the total energy of N photons represents some value of energy, for example 1J. In this sense, each "photon" is really a packet of photons. Then, the energy density is calculated by the following expression:

$$Q[i,j] \leftarrow \frac{Q[i,j] \cdot (1 \text{ Joule})}{NdV} \tag{84}$$

To calculate the light distribution, Φ[i,j], in J/cm², Eq.(79) is restated in terms of the arrays:

$$\Phi[i,j] = \frac{Q[i,j]}{\mu_a[i,j]} \tag{85}$$

where μ_a[i,j] denotes the absorption coefficient of the local grid element. In a uniform tissue, μ_a is constant, but in complex tissue models μ_a may vary.

Reflectance (transmittance) data

Recall that reflectance (or transmittance) of photons, R(x,y) or T(x,y), were calculated in terms of their position of escape at (x,y). Let us choose to store the reflectance in the array R[i] where i denotes the cylindrical coordinate r, as defined in Eqs.(80)-(82). The raw data is converted to a useful form by the expression:

$$R[i,j] \leftarrow \frac{R[i,j]}{N(2i+1)\pi dr^2} \tag{86}$$

The units of R[i] are cm^{-2}.

In general terms, R(r) is the local diffuse reflectance in cm^{-2}, which expresses the fraction of the incident energy that escapes per unit area of surface. The total reflectance, R_t, is given:

$$R_t = R_{sp} + \int_0^\infty R(r) 2\pi r dr \tag{87}$$

where R_{sp} is the specular reflectance that occurred at photon launching (see Eq.(56). Both R_t and R_{sp} are dimensionless.

7.1.5 Varieties of sources

The above treatment has considered a Monte Carlo simulation where all photons were launched at the origin perpendicular to the tissue surface. The result is essentially a narrow impulse of collimated radiation incident at the surface, which is a special case not usually encountered in the research laboratory or medical clinic. More typical types of sources are the uniform flat-field beam of a finite diameter, the Gaussian beam profile, the divergent beam from an optical fiber, and a point source of fluorescence within a tissue. The propagation and data analysis equations of section 7.1.2 and 7.1.3 can be applied to all these cases.

Consider cylindrical symmetry incident beam (e.g. flat-field beam and Gaussian beam). The response of a symmetric tissue to the finite diameter beam can be obtained by convolving the impulse response against the radiant exposure distributions of the light beam.

Flat-field beam

Assume a collimated flat-field beam has a radius w and a total energy of 1 unit (e.g. 1 J). The radiant exposure of the source, S(r), is given:

$$S(r) = \begin{cases} 1 / \pi w^2 & r \le w \\ 0 & r > w \end{cases} \qquad (88)$$

Let us assign the values of $\Phi(r,z)$ obtained by Eq.(85) to a new function G(r,z) to emphasize its role as an impulse response:

$$G(r,z) = \Phi(r,z) \qquad (89)$$

The function G will be repeatedly used during subsequent convolutions to generate various distributions for $\Phi(r,z)$ that depend on the radiant exposure, S(r).

Convolution of the impulse response G against the radiant exposure S in cylindrical coordinates is illustrated in figure 50, and is specified by the expression:

$$\Phi(r,z) = \int_0^w S(r')\left[\int_0^{2\pi} G(\sqrt{r^2 + r'^2 - 2rr'\cos\alpha'}, z)d\alpha'\right] \cdot r'\,dr' \qquad (90)$$

where w is the radius of the source, α' is the angle between the vector from the origin to a source point (r',α') and the vector from the origin to an observation point $(r,0)$. Although G depends on z, the convolution is evaluated completely for one desired depth, so z is a constant during each integral evaluation. The units of G are cm^{-2}, the units of S are J/cm^2, the double integration yields area in units of cm^2, therefore the resulting Φ is in units of J/cm^2.

There is a symmetry to this convolution which simplifies numerical evaluation. The cylindrical coordinate system may be transformed, as depicted in figure 50b, which allows Eq.(90) to be restated:

$$\Phi(r,z) = \int_{w-r}^{w+r} G(r'', z)\left[\int_0^{2\pi} S(\sqrt{r^2 + r''^2 - 2rr''\cos\alpha''}) \cdot d\alpha''\right] \cdot r''\,dr'' \qquad (91)$$

The advantage of the transformed coordinate system is that the integral within the brackets becomes independent of depth z because S is independent of z. Therefore, a single evaluation of the bracketed term can be repeatedly used for each of the many depth, z, which are considered. In contrast, the bracketed term in Eq.(90) requires reevaluation for each depth z that is considered because G depends on z.

The transformation is illustrated in figure 50. The first coordinate system has its origin at the center of the source, as in figure 50a and Eq.(90). The point of observation is at $(r,0)$. An incremental region of source is located at (r',α') and has a value $S(r')$. The distance between the source point and observation point is d' equal $\sqrt{r^2 + r'^2 - 2rr'\cos\alpha'}$. the limits of integration range from zero to w which is the radius of the source.

The second coordinate system has its origin at the center of the point of observation, as in figure 50b and Eq.(91). The source is centered at $(r,0)$. The incremental region of source is located at (r'',α'') and has a value S(d"), where d" equals

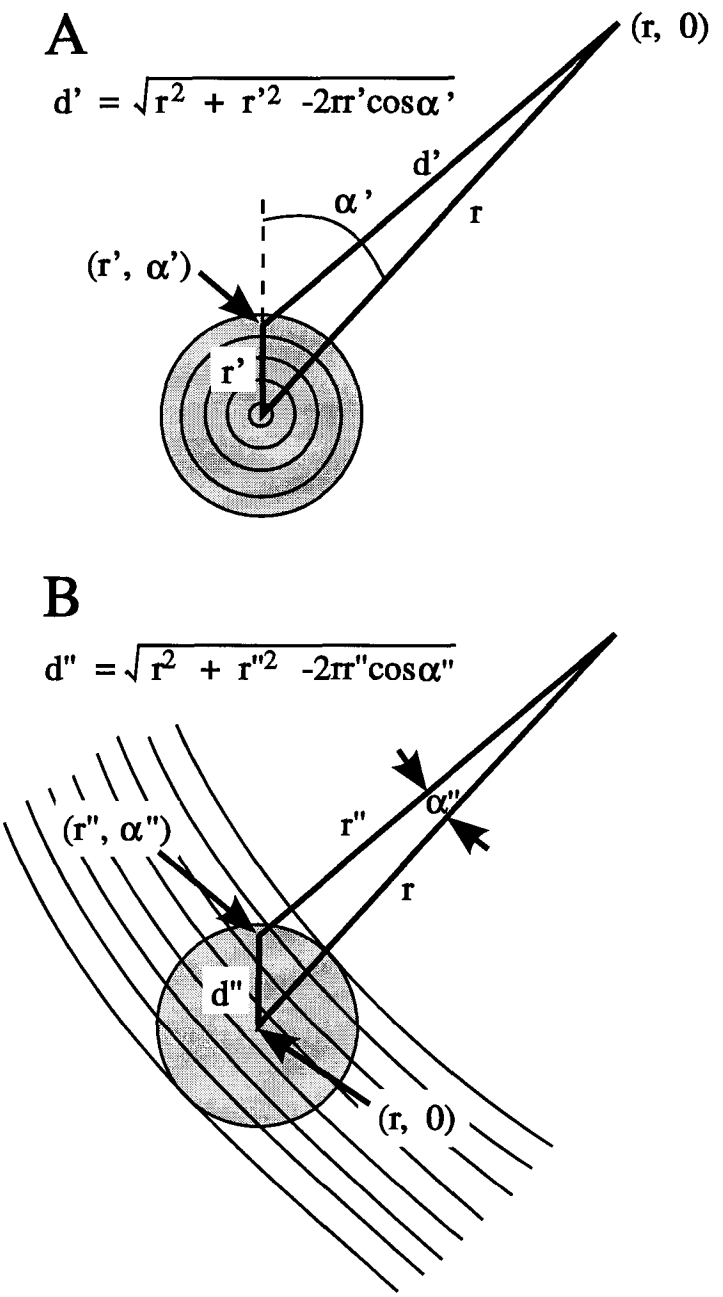

Figure 50. Coordinate system for convolution of impulse response, G, over the source function, S (stippled region). The thin lines indicate the rings of integration during convolution in cylindrical coordinates. The coordinate systems shown are equivalent. (A) The origin is at the center of the source. The observation point is at (r,0). The convolution involves S(r') and G(d'). (B) The origin is at the point of observation. The center of the source is at (r,0). The convolution involves S(d") and G(r").

$\sqrt{r^2 + r"^2 - 2rr" \cos \alpha"}$. The distance between the source point and observation point is r". The limits of integration range from w-r to w+r, which are the minimum and maximum distance between a source point and the observation point. Note however that much of the region of integration lies outside the source and therefore the value of S in the integrand is zero.

In the original coordinate system (Figure 50a), the uniform flat-field beam provides a source of radiant exposure, S(r'), that is specified:

$$S(r') = \begin{cases} P / \pi w^2 & r' \leq w \\ 0 & r' > w \end{cases} \tag{92}$$

where P is the total power of the laser beam. In the transformed coordinate system (figure 50b), the solution for $\Phi(r,z)$ is conveniently summarized by restatement of Eq.(91):

$$\Phi(r,z) = \int_{w-r}^{w+r} G(r",z)\Theta(r,r")2\pi r" \, dr" \tag{93}$$

where $\Theta(r,r")$ equals the integration within the bracket in Eq.(91) divided by 2π:

$$\Theta(r,r") = \frac{1}{2\pi}\int_0^{2\pi} S(\sqrt{r^2 + r"^2 - 2rr" \cos \alpha"})d\alpha"$$

$$= \begin{cases} \frac{P}{\pi w^2} & r + r" \leq w \\ \frac{\alpha_0"}{\pi} \cdot \frac{P}{\pi w^2} & |r - r"| < w \text{ or } w < r + r" \\ 0 & |r + r"| > w \end{cases} \tag{94}$$

where

$$\alpha_0" = \cos^{-1}\left[\frac{r^2 + r"^2 - w^2}{2rr"}\right] \tag{95}$$

The three situations specified in Eq.(94) are illustrated in figure 51.

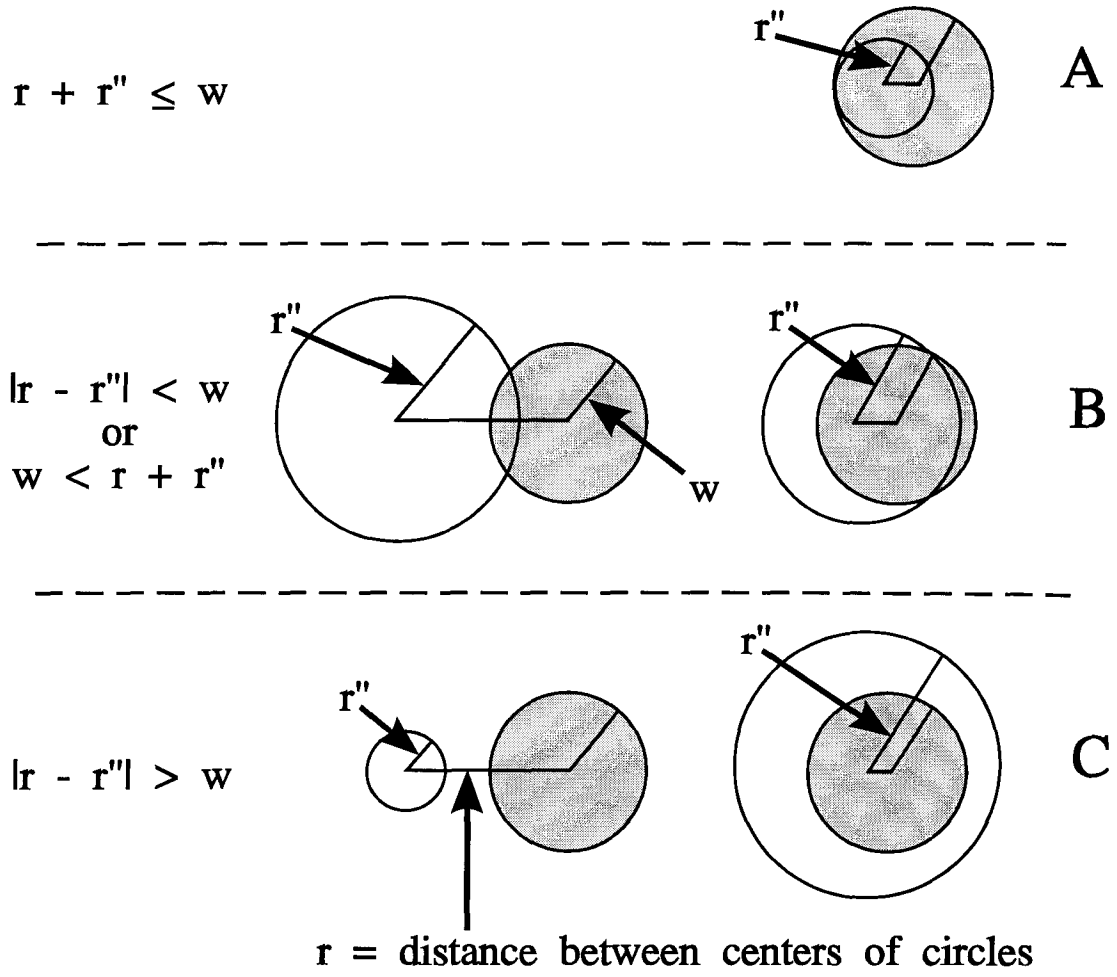

Figure 51. Convolution for a uniform laser beam. The source is a circular laser beam with radius w (stippled region). The observation point is at the center of the second circle (not stipled) with radius r". The convolution using the coordinate system of figure 50B involves integration over all possible values of r". Three situations arise. (A) The ring of integration with radius r" is completely within the source. (B) The ring of integration is partially within the source. (C) The ring of integration is never intersects the source. Eq.(94) lists the forms of the integrand for these three situations during the convolution.

Gaussian beam

A Gaussian beam with a $1/e^2$ radius of w and a total energy of 1 unit (e.g. 1 J) has the following radial distribution:

$$S(r) = \frac{2}{\pi w^2} \exp(-2r^2 / w^2) \tag{96}$$

which conserves energy:

$$\int_0^\infty S(r) 2\pi r dr = 1 \tag{97}$$

The convolution formula for a Gaussian beam profile was derived by Prahl *et al*, 1989:

$$\Phi(r,z) = \frac{2P}{\pi w^2} \exp\left[-2(r / w)^2\right] \int_0^\infty G(r'',z) \exp\left[-2(r''/w)^2\right] \cdot I_0\left(\frac{4rr''}{w^2}\right) 2\pi r'' dr'' \tag{98}$$

where I_0 is a zero-order modified Bessel function.

7.1.6 Modifying MCML for isotropic photon sources

The University of Texas M.D. Anderson Cancer Center provided us a program called MCML (standing for Monte Carlo Modeling of Light Transport in Multi-layered Tissue in Standard C, Wang and Jacques, 1992) which implemented numerically all the principles, rules, and equations discussed in proceeding sections. The MCML program can be readily used to calculate the responses of a multi-layered tissue to a normal incident light beam on the surface. However, the fluorescence emissions inside the tissue are buried isotropic photon sources. In order to model the fluorescence escape processes, the MCML program had to be modified.

The problem of buried isotropic photon sources inside the tissue of multiple planar layers is still cylindrically symmetric. Therefore, the data recording (grid) system and the propagation simulation functions need no changes. The major changes to the MCML program were at the photon launching. The fluorescence source is buried and isotropic. So the launched photons should be equally distributed over the 4π steradians.

This was realized by utilizing the function *Spin()* in the MCML program. This function accomplishes the photon scattering event governed by the Henyey-Greenstein phase function [Eq.(48)]. We first initialized the photon packet to be unidirectional (e.g. +z direction) temporarily, then pretended that the whole photon packet suffers an isotropic scattering on the same spot as initialized using the function *Spin()*. The anisotropy factor g in this function was set to zero. Other changes included defining one more variable to record the depth of the source inside the tissue and corresponding input structure changes of the MCML program.

The correctness of the modified program was verified by comparing the results obtained by this program with that published in the literature (e.g. Keijzer *et al*, 1989b).